Base Flow Modification by Plasma Actuation for Swept Wing Transition Control

Peng, K.

DOI
10.4233/uuid:6e1e3a01-d5bf-4101-ac23-2fc1720bb9ba

Publication date
2024

Document Version
Final published version

Citation (APA)
Peng, K. (2024). *Base Flow Modification by Plasma Actuation for Swept Wing Transition Control*. [Dissertation (TU Delft), Delft University of Technology]. https://doi.org/10.4233/uuid:6e1e3a01-d5bf-4101-ac23-2fc1720bb9ba

Base Flow Modification
by Plasma Actuation
for Swept Wing Transition Control

Base Flow Modification
by Plasma Actuation
for Swept Wing Transition Control

Dissertation

for the purpose of obtaining the degree of doctor
at Delft University of Technology,
by the authority of the Rector Magnificus prof. dr. ir. T.H.J.J. van der Hagen,
Chair of the Board for Doctorates,
to be defended publicly on
Monday 3 June 2024 10.00 hours

by

Kaisheng PENG

Master of Science in Electrical Engineering,
Southwest Jiaotong University, Chengdu, China,
born in Sichuan, China.

This dissertation has been approved by

promotor: Prof. Dr. M. Kotsonis
promotor: Prof. Dr. F. Avallone

Composition of the doctoral committee:

Prof. Dr. Ir. Rector Magnificus,	chairperson
Prof. Dr. M. Kotsonis,	Technische Universiteit Delft
Prof. Dr. F. Avallone,	Politecnico di Torino
Independent members:	
Prof. Dr. S. Leonov,	University of Notre Dame
Prof. Dr. A. Gangoli Rao,	Technische Universiteit Delft
Dr. N. Benard,	University of Poitiers
Dr. -Ing. J. Kriegseis,	Karlsruhe Institute of Technology
Dr. J. Serpieri ,	Politecnico di Torino
Reserve member:	
Prof. Dr. F. Scarano,	Technische Universiteit Delft

Keywords: Plasma, swept wing, boundary layer, crossflow instability, transition, flow control

Printed by: Rijnja, Den Haag

Front & Back: Airplane equipped with plasma, design by Kaisheng Peng.

ISBN 978-94-6366-866-8

An electronic version of this dissertation is available at
`http://repository.tudelft.nl/`.

Do it or do not do it
— you will regret both.

Søren Kierkegaard

Contents

ACKNOWLEDGEMENTS

The pursuit of a Ph.D. has perpetually seemed like an impossible dream for me, not to mention that embarking on the journey in a land thousand miles away. Yet, here I am, realizing that I have woven the threads of my doctoral thesis into the fabric of existence. The memories of my first arrival in the Netherlands still remain vivid. Despite commencing with worry and insecurity, this journey has unfolded into a tapestry of beauty and joy. Here I would like to grasp this opportunity to express my heartfelt gratitude to people who have contributed to this journey.

My profound appreciation goes to my promotor, Marios, for providing me with the opportunity to delve into the research project at TU Delft. His generous support, wide knowledge and boundless ideas have been invaluable not only to my research project, but also in shaping my professional and personal growth. Looking back on the entire PhD journey, the supportive discussions, thoughtful suggestions and enjoyable mealtime conversations serve as constant reminders of how fortunate I am to have him as my supervisor. His exemplary supervision of PhD students and dedication to research have established a model for what professors should embody.

I'm also grateful to my co-promotor, Francesco. His encouragement and easy accessibility have been sources of profound gratitude. Additionally, I appreciate his consistent provision of valuable and sincere feedback, contributing significantly to both my research endeavors and my development as a researcher.

Furthermore, I wish to extend my gratitude to Theo. His numerous favours related to the DaVis software, constructing the wing model $K-M3J$, and imparting Matlab plotting skills have played a crucial role in ensuring the smooth progress of my research. He has also been a great friend, providing support and companionship throughout this journey. The jokes and conversations we shared during our private drinks and meals have added vibrant colors to my PhD adventure.

I would also like to express my sincere appreciation to the members of my doctoral committee for their time and effort in reviewing this document. Their valuable questions and suggestions have enriched this research.

I extend special appreciation to Emiel and Stefan, the dedicated technicians in the low-speed lab. Their great support in constructing the wing model $K-M3J$ and endeavours in maintaining a functional and friendly lab environment are truly commendable. Their prompt response to any technical issues deserves recognition, as does the enjoyable lunchtime conversations we've had.

A heartfelt appreciation is reserved for Colette, whose dedication and active involvement have been pivotal for the seamless operation of our section. From the initial stages to the completion of this thesis, her guidance and assistance have been indispensable.

A sincere appreciation is extended to my colleagues in the low-speed lab. I want to express my gratitude to Giulia, Beto, Hongxin, Rodrigo, Alessandro, Sven, Jordi,

Marina, Giulio, Babak, Yifu and Parisa, for fostering such an enjoyable and welcoming office environment. The happy time we've shared together have made our collective experience truly special. A heartfelt appreciation goes to Giulia. Her friendship both inside and outside the office have been a lifeline, especially during the quarantine period. Her care and support pulled me through those challenging days, casting a warm light on the gray moments. I'm truly grateful for her thoughtful gestures, from organizing my birthday celebration to inviting me to gatherings and warmly welcoming me at her hometown. Thank you, Giulia, for being a constant source of comfort and joy in my life. A special appreciation also goes to Beto for being my first friend in the Netherlands. His support and friendship became my anchor when facing the uncertainties of starting a PhD project in a foreign land. Appreciation also goes to Sven for translating my summary to Dutch and kindly letting me using his screen for the whole PhD period.

Furthermore, I'd like to also thank my colleagues in high-speed lab, Ata, Tyler, Alessandro, Edoardo, Gabriel, Luis, Constantin, Jane, Christoph, Kushal, Adrian, Thomas, Ilda, Kherlen, Luuk, Babak, Haris, Renzhi, Wencan, Adrian and Mengie for enriching my academic journey and social life. The social activities we engaged in served as a refreshing break from academic routines, and I am grateful for the collaborative spirit that fuelled our shared moments.

Throughout my PhD project, I had the privilege of working with Joerie on his MSc thesis. Despite the challenges encountered in experiments, the collaboration proved to be highly rewarding. I genuinely appreciate the opportunity he afforded me to evolve both as a researcher and a supervisor.

A genuine thanks extends to my Chinese community – Weibo, Xiaodong, Ming, Yu, Yi, Jingna, Xiang, Dong, Yanan, Guanqun, Wenchan and Yifu. Our shared experiences of Chinese cuisine and European travels created golden memories that defined this journey. Amidst the quarantine, their daily support and companionship were pillars of strength, turning challenging times into moments of shared resilience and connection. Grateful for the warmth, camaraderie, and the beautiful tapestry of moments we wove together outside the confines of the office.

From a thousand miles away, my heartfelt appreciation extends to my parents and relatives for their unwavering support and care. I'm also grateful to my friends in China, whose support means a lot to me, even from afar.

The last gratitude goes to the old Kaisheng, for his complete courage in starting this journey and never giving up.

SUMMARY

In the upcoming decades, a substantial growth in the commercial aviation market is anticipated, accompanied by an increasing societal awareness of global warming. This circumstance necessitates a technological development for emission reduction in future transport aircraft. A method for aerodynamic efficiency improvement is the so-called Laminar Flow Control (LFC), which can potentially achieve a considerable boost in aircraft efficiency. The research described in this thesis focuses on the specialised strategy of Base Flow Modification (BFM) based on plasma actuators (PAs), a promising member in the LFC family.

The results of this booklet is divided into three main parts. The first part explores the effects of unsteady PA-induced perturbations on a swept wing boundary layer dominated by stationary crossflow (CF) vortices, representative of typical cruise flight regimes. Key parameters such as forcing frequency and streamwise location of PAs are scrutinized, which have pronounced effects on the development of crossflow instabilities (CFIs). To focus on the PA-induced unsteady disturbances, PAs are operated at very low power to minimize the net BFM effect.

The second part primarily aims to experimentally validate the reduction of CF component achieved by the plasma-based BFM. It also delves into the effects of the PA forcing on the base flow and developing CFIs in a swept wing boundary layer. Employing the BFM strategy, a simplified predictive model is constructed with linear stability theory analysis to infer CFI modes' characteristics. The achieved CF reduction and the base flow direction are traced under various momentum coefficients, which are controlled by the applied high voltage amplitude. Moreover, the streamwise growth of stationary and travelling CFIs is investigated under the condition of PA actuation.

The last part focuses on controlling CFIs and laminar-turbulent transition in an experimental swept wing model using the plasma-based BFM technique. A simplified model coupled with linear stability theory analysis predicts the net BFM effect on CFI modes. Experiments are conducted in a low-turbulence wind tunnel where PA is operated at constant input voltage and frequency to achieve the BFM control. Various parameters of the PA-based BFM technique are investigated, namely the Reynolds number, angle of attack and wavelength of dominated stationary CFI modes. The results generally confirm the stabilising ability of BFM on the swept wing boundary layer. More importantly, the PA-based BFM essentially renders the boundary layer more susceptible to travelling CFIs. In the presence of net BFM effect and intrinsic PA unsteadiness, the PA-based BFM technique achieves transition delay with specific combinations of Reynolds number, angle of attack and wavelength of dominated stationary CFI modes.

SAMENVATTING

In de komende decennia wordt een aanzienlijke groei van de commerciële luchtvaartmarkt verwacht, vergezeld door een toenemend maatschappelijk bewustzijn van de opwarming van de aarde. Deze omstandigheid vereist technologische ontwikkelingen voor het verminderen van emissies in toekomstige transportvliegtuigen. Een methode die voor verbetering van aerodynamische efficiëntie kan zorgen is de zogenaamde Laminar Flow Control (LFC), die mogelijk aanzienlijke verbeteringen in de efficiëntie van vliegtuigen kan opleveren. Het onderzoek dat in deze scriptie wordt beschreven, richt zich op de gespecialiseerde strategie van Base Flow Modification (BFM) op basis van plasmabesturingsactuatoren (PAs), een veelbelovend onderdeel van de LFC-familie.

Dit boek is verdeeld in drie hoofdonderdelen. Het eerste deel onderzoekt de effecten van onstabiele door PA veroorzaakte verstoringen op een grenslaag gedomineerd door stationaire dwarsstroomwervels (CFI), representatief voor typische cruisevluchtregimes. Belangrijke parameters zoals de frequentie van de verstoring en de locatie van Pas op de vleugel worden onderzocht, die een aanzienlijke invloed hebben op de ontwikkeling van dwarsstroomwervels. Om zich te concentreren op de door PA veroorzaakte verstoringen, worden de PAs bediend met zeer lage kracht om het netto BFM-effect te minimaliseren.

Het tweede deel heeft voornamelijk tot doel de vermindering van de dwarsstroomwervelcomponent die is bereikt door de op plasma gebaseerde BFM experimenteel te valideren. Het gaat ook in op de effecten van de PA-verstoring op de basisstroom en de ontwikkeling van CFIs in een geveegde vleugelgrenslaag. Met behulp van de BFM-strategie wordt een vereenvoudigd voorspellend model opgesteld met lineaire stabiliteitstheorieanalyse om de kenmerken van CFI-modi af te leiden. De bereikte CF-vermindering en de richting van de basisstroom worden gevolgd onder verschillende impulscoëfficiënten, die worden gecontroleerd door de toegepaste hoogspanningsamplitude. Bovendien wordt de stroomafwaartse groei van stationaire en reizende CFIs onderzocht onder de voorwaarde van PA-aansturing.

Het laatste deel richt zich op het beheersen van CFIs en laminair-turbulente overgang in een experimenteel model van een geveegde vleugel met behulp van de op plasma gebaseerde BFM-techniek. Een vereenvoudigd model met lineaire stabiliteitsanalyse voorspelt het netto BFM-effect op CFI-modi. Experimenten worden uitgevoerd in een windtunnel met weinig turbulentie waar PA wordt bediend bij constante invoerspanning en frequentie om de BFM-besturing te bereiken. Diverse parameters van de op PA gebaseerde BFM-techniek worden onderzocht, namelijk het Reynolds-getal, de aanvals-hoek en de golflengte van gedomineerde stationaire CFI-modi. De resultaten bevestigen over het algemeen de stabiliserende capaciteit van BFM op de geveegde vleugelgrenslaag. Belangrijker nog, de op PA gebaseerde BFM maakt de grenslaag wezenlijk gevoeliger voor bewegende CFIs. In aanwezigheid van

het netto BFM-effect en intrinsieke PA-onstabiliteit bereikt de op PA gebaseerde BFM-techniek vertraging van de overgang met specifieke combinaties van Reynolds-getal, aanvals-hoek en golflengte van gedomineerde stationaire CFI-modi.

1

PROLOGUE

In this chapter, crossflow instabilities and laminar-turbulent transition are introduced in the context of swept wing boundary layers. Laminar flow control strategies based on plasma actuators are elaborated upon mitigating the crossflow component of base flow and/or crossflow instabilities, with particular focus on the base flow modification strategy. Furthermore, insight is provided into the motivation of this research, along with the organization of this thesis.

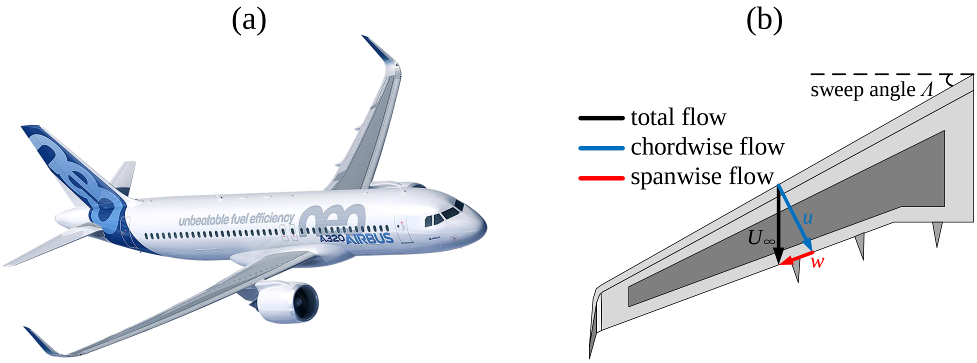

FIGURE 1.1: (a) A320neo aircraft of Airbus[1]; (b) Schematic of the flow over swept wing.

1.1. INTRODUCTION

The swept wing concept emerged as a significant aviation innovation in the early 20th century, catering to the demands of high-speed flight cruising. After proving its effectiveness in World War II, the swept wing design gained widespread adoption in commercial aviation due to its practicality. Since then, swept wings made a substantial impact on the air travel by enhancing aircraft speed and efficiency, improving payload capacity and extending travelling distance.

A prime example of the swept wing design's contemporary relevance is illustrated by the Airbus A320neo aircraft, as depicted in figure 1.1 (a). This member of the Airbus A320 family stands out for cutting-edge features and exceptional fuel efficiency. Figure 1.1 (b) depicts a sketch of the flow over swept wing, which is positioned at a sweep angle Λ relative to the fuselage. By sweeping the wing backward, the inviscid flow U_∞ (black arrow) is decomposed into two components. One is called chordwise flow u, parallel to the chord line (blue arrow) and the other is spanwise flow w, perpendicular to the chord (red arrow). Compared to the straight wing where the total airflow accelerates, the swept wing configuration only causes the acceleration of chordwise flow, a part of the total flow. As a result, the swept wing reduces the amount of flow acceleration, resulting in the delayed or even suppressed formation of shockwaves during high-speed flight. This in turn, increases the critical Mach number of aircraft and further minimizes wave drag, increasing the lift-to-drag ratio. In the contemporary aviation landscape, virtually all modern high-speed aircraft, whether used for commercial or military purposes, incorporate the swept wing design in some form. Its widespread adoption underscores its effectiveness in meeting the demands of efficiency, speed, and stability, solidifying its status as an indispensable feature in the evolution of aviation.

---

[1] Source: `https://www.nicepng.com/ourpic/u2e6t4r5i1w7e6y3_7-min-a320-neo-png/`

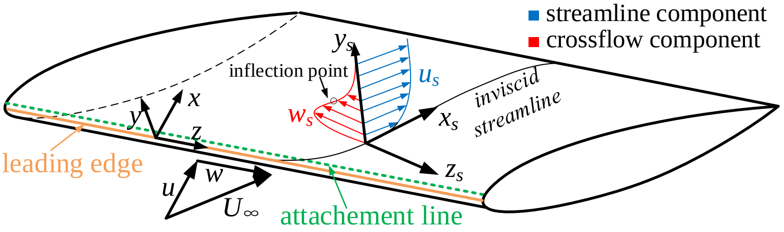

FIGURE 1.2: Sketch of flow components developing on the infinite swept wing, re-adjusted from [28].

1.2. SWEPT WING BOUNDARY LAYER

The boundary layer theory (initially introduced by Prandtl [71]), describes the viscous effect of fluids in the proximity of the aerodynamic body. This elucidates the disparities between inviscid flow theoretical solutions and empirical observations. According to the boundary layer theory, the flow retains its inviscid nature outside the boundary layer. Whereas, the flow velocity diminishes to zero at the aerodynamic body surface, due to the non-negligible viscous effect. This effect becomes more pronounced at lower external flow velocity, as the inertial forces in the boundary layer become comparable to the viscous forces. This confined thin layer, however, exhibits significant impact on the integral aerodynamic performances of airfoils and wings since the inviscid flow assumption doesn't hold there.

1.2.1. CROSSFLOW AND CROSSFLOW INSTABILITY

The swept wing boundary layer exhibits distinctive three-dimensional flow characteristics, inside which the so-called crossflow (CF) velocity component arises. Particularly, the region near the leading edge is characterized by a favourable pressure gradient (though its intensity and spatial extension are subject to the wing geometry). These conditions are representative of free-flight environment and contribute to the emergence of the crossflow instabilities (CFIs). The following discussion, accompanied by a simplified schematic in figure 1.2, sheds light on the formation of CF component. Let's consider a simple case, the infinite swept wing (i.e. invariant in the spanwise direction) as an illustrative example. In order to facilitate the description, the swept wing aligned system xyz and the local inviscid streamline-aligned coordinate system $x_s y_s z_s$ are introduced, as shown in figure 1.2. The x and z axes are perpendicular and parallel to the leading edge respectively, while the y axis is aligned normal to the local wing surface. The x_s is tangential to the local inviscid streamline while the z_s is normal to the inviscid streamline. The y_s axis coincides with the y axis. Additionally, the velocity components corresponding to xyz and $x_s y_s z_s$ are denoted as $[u\,v\,w]$ and $[u_s\,v_s\,w_s]$.

At the leading edge, the inviscid flow U_∞ can be decomposed into two orthogonal components, namely chordwise flow u and spanwise flow w, aligned with the x and z axes. As the flow passes over the wing body, u is accelerated by the favourable pressure gradient, while w remains unaltered due to the spanwise invariant conditions (recalling the infinite wing in the z direction). In the inviscid flow outside of the

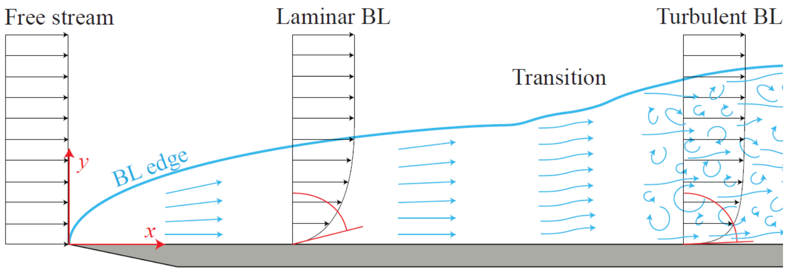

FIGURE 1.3: Schematic of boundary layer (BL) over a flat plate, developing from laminar to turbulent. The tangent angles of velocity profiles are shown in red, corresponding to $\frac{\partial u}{\partial y}|_{wall}$, re-adjusted from [84].

boundary layer, the pressure gradient is balanced by centripetal acceleration. However, this force balance doesn't hold inside the boundary layer due to the wall-normal decrease of streamline-aligned velocity u_s (which decreases to zero at the wall due to the viscous effects). The decrease of u_s results in a lack of associated momentum to compensate the pressure gradient and ultimately leads to the formation of CF component w_s, which directs perpendicularly to the streamline.

The w_s profile shown in figure 1.2 corresponds to the CF component and vanishes at the wall (due to the non-slip condition) and the boundary layer edge (due to the force balance), leading to a maximum in the wall-normal direction. This renders an inflection point of the w_s profile (the circular marker in figure 1.2), serving as a source of CFIs which follow the inviscid instability mechanism. Numerous studies demonstrate that CFIs are largely insensitive to sound but rather depending on environmental disturbances such as freestream turbulence intensity and surface roughness. Generally, in conditions of sufficient CF component (e.g. relatively high Re and angle of attack α, [85]), CFIs are significantly enhanced, dominating the boundary layer and transition process. However, it should be noted that the dominance of CFIs is limited in the region of favourable pressure gradient, since the swept wing boundary layer could be susceptive to other instabilities at certain conditions. For instance, attachment line instability could be amplified at large leading-edge radius, with Görtler vortices at concave surface and Tollmien-Schlichting waves at adverse pressure gradient, as summarized by Rius Vidales [76]. Comprehensive literature reviews on the nature of CFIs can be found in the work of Bippes [7], Saric *et al.* [80] and Wassermann & Kloker [94, 95].

1.2.2. LAMINAR-TURBULENT TRANSITION

As long ago as the 18th century, Reynolds' experiments revealed that the boundary layer's behaviour, namely the laminar or turbulent state, depends on the Reynolds number Re, which represents the ratio of inertial and viscous forces [75]. Particularly, laminar flow is characterized by the orderly movement of fluid particles in parallel layers without chaos and occurs at relatively low Re. On the other hand, turbulent flow is marked by irregular and chaotic fluid motions with increased momentum exchange and emerges at relatively high Re. Figure 1.3 depicts the transition process

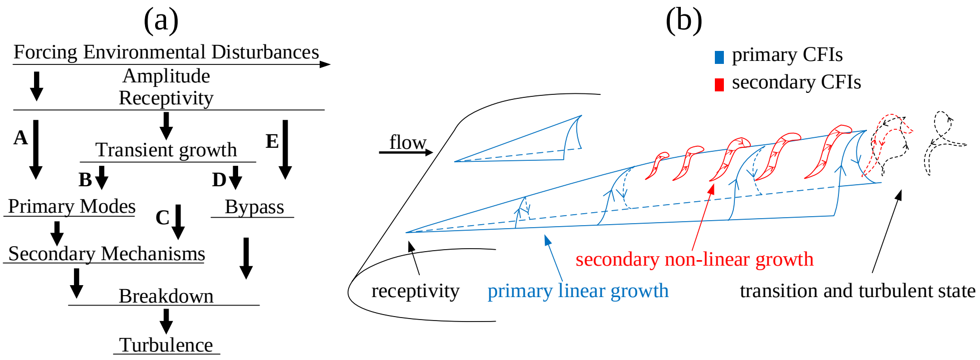

FIGURE 1.4: (a) Boundary layer transition paths, re-adjusted from [65]; (b) Sketch of the laminar-turbulent transition driven by CFIs, following the path A.

where a boundary layer develops from laminar to turbulent. Additionally, compared to the laminar flow, the velocity profile of turbulent flow is distinctively fuller near the wall, as the larger angle (i.e. $\frac{\partial u}{\partial y}|_{wall}$) shown in figure 1.3. Since the wall skin friction τ holds a function of fluid viscosity μ and velocity gradient at the wall ($\tau = \mu \frac{\partial u}{\partial y}|_{wall}$), this disparity in turn leads to a significant discrepancy in τ between laminar and turbulent boundary layers. In general, turbulent boundary layer experiences larger skin friction than its laminar counterpart. Considering that skin friction contributes nearly half of the total drag [76], airfoils and wings surrounded by laminar boundary layers are recognized as more *economic* since less propulsive thrust is required to compensate for aerodynamic drag. As a result, numerous studies have been inspired by this insight, focusing on maintaining laminar boundary layers on aerodynamic bodies, particularly at high *Re*.

As the flow develops downstream, the boundary layer undergoes an alteration from laminar to turbulent regime through the transition process. This process could be subject to various transition paths illustrated in figure 1.4(a) as summarized by Morkovin [65]. Nonetheless, in the context of current work, the development of swept wing boundary layer is subject to CFIs and assumed to follow the path A. Figure 1.4(b) depicts the transitional path A driven by CFIs. Primary CFIs are initiated and characterized by external disturbances through the receptivity process. If these CFIs are initiated with sufficiently weak amplitudes, a modal framework can be applied to such disturbance field (i.e. a linear superposition of orthogonal modes, [58]). Undergoing the amplitude growth, these primary modes strongly modulate the boundary layer, followed by an explosive growth of secondary modes. The secondary modes feature dissimilar flow structures than primary ones and ultimately lead to the laminar-turbulent transition. Nonetheless, considering the distinct features of primary CFIs (i.e. stationary and travelling CFI modes), the boundary layer development and transition scenarios can vary significantly. Hence, the following two sections are dedicated to influences of these two primary modes, following the path A. Specifically, section 1.2.3 illustrates transition scenarios dominated by stationary CFIs while section 1.2.4 focuses on scenarios characterized by travelling CFIs.

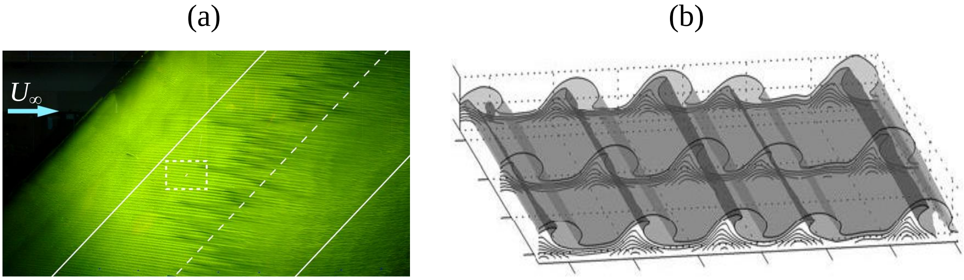

FIGURE 1.5: (a) Fluorescent oil flow visualization of the swept wing model $M3J$ at the presence of DREs, re-adjusted from [85]; (b) Time-average velocity magnitude along the stationary CF vortex axis measured with tomo-PIV, re-adjusted from [86].

1.2.3. Transition Induced by Stationary Crossflow Instabilities

In general, primary stationary CFIs are characterized by stationary vortices that remain spatially *fixed* along the wing span and align closely with freestream inviscid streamlines. Figure 1.5(a) presents an oil visualization [85] and (b) shows a tomo-PIV measurement of these stationary vortices [86]. A sequence of span-wise periodic streaks are confirmed by both techniques, outlining the three dimensional structures of stationary vortices. Extensive researches have demonstrated the dominant role of these CFIs in the development and transition of swept wing boundary layers, at conditions of low freestream turbulence intensity T_u [7, 80]. Such condition (i.e. low T_u) can be found in free flight environment, representing the clean cases (i.e. not controlled by plasma actuator) of this work. At the condition of low T_u, the growth of stationary CFI modes has been found highly sensitive to surface roughness, which emerges as a key factor influencing the receptivity process of stationary CFI modes. Numerous studies have been dedicated to the understanding of receptivity to various types of surface roughness, such as distributed surface roughness patch (DRP), isolated discrete roughness element (IDRE) and discrete roughness element (DRE) arrays [34, 72, 101]. These surface roughness configurations are representative for various practical scenarios, including wing surface finish (DRP), insect strikes/protruding rivets (IDRE) and periodic rivets (DRE), respectively. In this study, DRE is chosen as the primary method for initiating stationary CFI modes (though a small-amplitude DRP is also included in Chapter 6). The selection of DRE offers several advantages, including the efficacy in initiating stationary CFI modes and a focus on single stationary mode characterized by DRE. This simplifies the investigation process and ensures more consistent and comparable results. Several studies have been dedicated towards exploring the receptivity of DRE arrays in three dimensional boundary layers. The results have revealed that several parameters such as element height, shape, location and spanwise spacing play a vital role in the receptivity process [7, 80, 94, 105]. Insights of the near-element flow fields are first given by numerical studies of Kurz & Kloker [54, 55] and then followed by the experimental observation of Zoppini *et al.* [103]. The results indicate that behind the element, two counter rotating

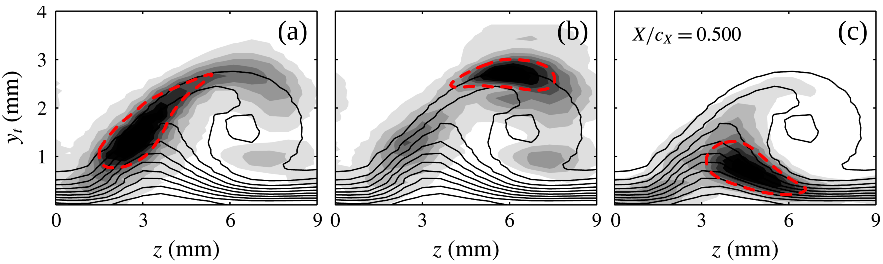

FIGURE 1.6: Contours of bandpass filtered velocity fluctuations and time-average fields (10 levels from 0 to U_∞, solid lines) from hot-wire measurements on the swept wing model $M3J$, re-adjusted from [86]. The frequency bands correspond to (a) type I mode ($5\,\text{kHz} \leqslant f \leqslant 6\,\text{kHz}$); (b) type II mode ($7\,\text{kHz} \leqslant f \leqslant 8\,\text{kHz}$); (c) type III mode ($350\,\text{Hz} \leqslant f \leqslant 550\,\text{Hz}$).

vortices are formed. While one vortex gradually decays downstream, the other one is favoured by the CF component and continues growing, eventually triggering primary stationary CFI modes.

Subsequently these initiated primary stationary CFI modes undergo a quasi-linear stage, which is characterized by small vertical and spanwise fluctuation components of v' and w' respectively (i.e. in y and z directions, recalling figure 1.2). In the quasi-linear growth stage, the downstream development of stationary CFI modes is characterized by distinct trajectory directions and growth rates depending on their wavenumber vectors. As stationary CFI modes propagate downstream, their small components of v' and w' convect low-momentum flow away from the wall and replace with high-momentum flow, and vice versa. Though this momentum exchange process starts with small v' and w', it occurs in regions characterized by large vertical gradients of streamwise velocity u (i.e. region close to the wall). This leads to a rapid amplification of the streamwise component u' and non-linear interactions start to play a role in the development of stationary CFI modes [80]. When stationary CFI modes further reach non-linear saturation amplitudes, this state can persist for quite a streamwise distance. Concurrently, the aforementioned momentum modulation generates strong velocity shears in the spanwise and wall-normal directions. These strong-shear layers are highly unstable to secondary CFIs and lead to a rapid emergence of the latter. The secondary CFIs are generally categorized as two types, namely type I and type II modes, which are characterized by their distinct frequency ranges and spatial locations (within primary CFI structures). Figure 1.6(a) and (b) depicts the type I and type II modes within the stationary CF vortex, while (c) illustrates the type III mode and will be discussed in section 1.2.5. In particular, type I modes are closely connected to the local minimum spanwise gradient of the mean flow and emerge in the outer side of stationary vortices' upwelling region. On the other hand, type II modes are located on the top of stationary vortices where wall-normal gradients of streamwise velocity are pronounced. Compared to type I modes, type II modes tend to have lower energy and higher frequencies. Consequently, these secondary modes undergo rapid amplifications, along with the perturbation spectrum filled up progressively, ultimately leading to the fast transition. Due to the fact that the transition develops locally, the transition front induced by stationary CFI

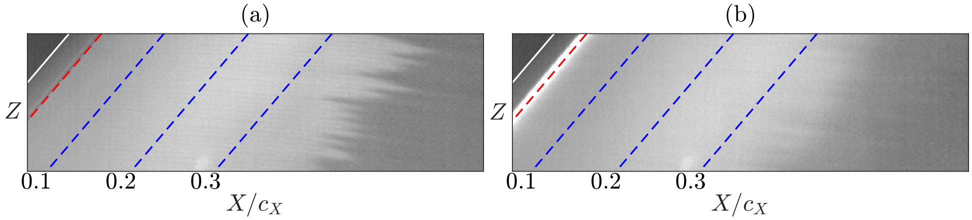

FIGURE 1.7: Infrared thermography images of transition patterns induced by (a) stationary CFIs and (b) travelling CFIs on the swept wing model $M3J$ at the condition of $Re = 2.5 \times 10^6$ and $\alpha = 2.5°$. The white line indicates the leading edge and the flow comes from left to right. The red dashed line indicates the PA location.

modes is non-uniform in wing span and characterized by pronounced jagged-patterns of turbulent wedges. An example can be found in figure 1.7 (a) where the transition pattern of stationary CFIs is illustrated by the infrared thermography measurement. The measurement is conducted on the swept wing model $M3J$ installed in the low turbulence wind tunnel (LTT) of TU Delft. The DRE array is installed near the leading edge to amplify stationary CF vortices.

1.2.4. TRANSITION INDUCED BY TRAVELLING CROSSFLOW INSTABILITIES

The other type of primary CFIs, travelling CFI modes, are oblique waves propagating along the wing span at non-zero frequency. The transition mechanism of travelling CFIs essentially shares similarities with the one of stationary CFIs, following the path A in figure 1.4(a). Nonetheless, notable distinctions are found for travelling CFIs throughout each stage leading up to transition. With respect to the receptivity, travelling CFIs are usually characterized by a high susceptivity to the freestream turbulence intensity T_u, in contrast to stationary CFIs. Notwithstanding, it should be noted that travelling CFIs are also susceptive to surface nonuniformities, such as phased surface roughness at conditions of high T_u [12]. Experimental investigations on the receptivity of travelling CFIs are mainly carried out in (but not limited to) the Institute of Theoretical and Applied Mechanics (ITAM) in Novosibirsk by Kachanov and co-workers, by which several types of receptivity can been identified for travelling CFIs, depending on various scenarios [13, 15, 16]. Within the context of this thesis, travelling CFIs are initiated mainly through three types of receptivity process. One such type is the 'roughness-vortex' receptivity, which occurs in scenarios where freestream vortices interact with surface non-uniformities (e.g. wing surface roughness and waviness). It should be noted that, this receptivity process is usually weak but can be effective in the presence of phased roughness. This receptivity is assumed to occur in both clean cases and plasma-controlled cases in this work, due to the presence of DRE arrays as well as possible residues of plasma actuator surface finishing (i.e. electrode and dielectric material). The other two types of receptivity are distinguished as the surface vibrations interacting with or without the freestream vortices. These two receptivity processes are both found to be rather effective in initiating travelling

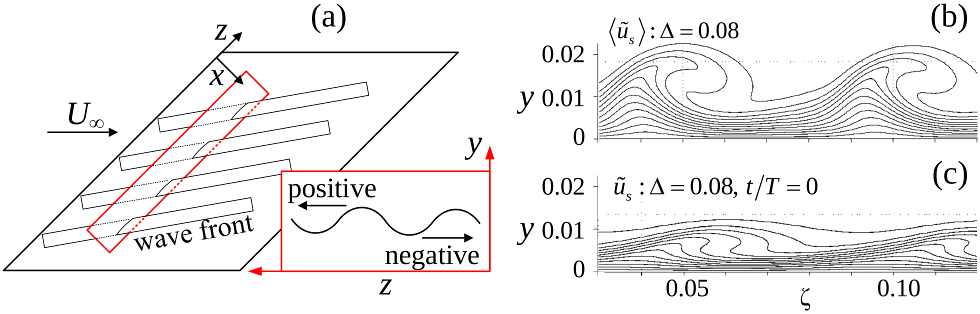

FIGURE 1.8: (a) Schematic of positive and negative travelling CFIs. Inset depicts the travelling mode's direction in the yz plane (looking from upstream); (b) Contours of stationary CF vortices in the fixed streamwise system at $\xi = 3.2$; (c) Instantaneous contours of travelling CF vortices in the fixed streamwise system at $\xi = 2.0$, re-adjusted from [95].

CFIs and the resulting disturbance amplitudes and phases significantly depend on the disturbance spanwise wavenumber and frequency [14, 38]. In this work, the surface vibration is found to be caused by the unsteady plasma forcing (section 1.3.4) and the two aforementioned surface vibration receptivity processes can be expected in only plasma-controlled cases.

These initiated travelling CFI modes essentially consist of two distinct wave families that are characterized by opposite propagating directions. Specifically, the positive travelling CFI modes propagate in the opposite direction to CF component, while the negative travelling CFI modes propagate in the CF direction. Figure 1.8(a) depicts the directions of positive and negative travelling CFI modes in the yz plane (looking from upstream). Nonetheless, these travelling CFI modes display trajectories that are inclined at various angles to the freestream line, in contrast to stationary CFI modes. The wave trajectory shows a high dependency on the disturbance frequency. That is, the higher frequency, the more inclined trajectories of travelling CFI modes (i.e. more deviated from the inviscid streamline). More importantly, the positive travelling CFI modes appear as more unstable than negative travelling CFI modes and stationary CFI modes, as they feature significantly larger growth rates downstream, as found in a majority of studies [8, 40]. During the downstream development of travelling CFI modes, the momentum modulation of slow and fast flow occurs, similar to the one observed in stationary vortices. However, in travelling CFI modes, this modulation takes place in an instantaneous manner, leading to an unsteady deformation of the mean flow. In general, the instantaneous vortex structures of travelling CFI modes share some similarity with stationary vortices. Nonetheless, compared to stationary CF vortices, the instantaneous vortex structure of travelling CFI modes is more stretched and flat in the spanwise direction, as illustrated in figure 1.8(b) and (c). Consequently, the instantaneous travelling vortices exhibit larger streamwise vorticity and stronger wall-shear layers. Undergoing a similar secondary mechanism, the travelling CFI modes ultimately lead to transition. Nonetheless, the transition induced by travelling CFI modes features minimal distinct turbulent wedges and appears as quasi-uniform in the spanwise direction, in contrast to the one induced by stationary CFI modes. An illustrative example is shown in figure 1.7(b), where strong travelling CFIs are induced by a plasma actuator located at the red dashed line.

1.2.5. Interaction between Primary Stationary and Travelling Crossflow Instabilities

In realistic application environments (such as free flight), both stationary and travelling CFI modes can be present within the boundary layer, through the aforementioned receptivity processes (e.g. phased roughness receptivity). The mutual interactions between these modes are important in determining the boundary layer development, ultimately influencing the transition process. For instance, stationary CFI modes of diverse wavenumbers, originating from surface roughness, could interact with travelling CFI modes of a broadly amplified band of frequencies. Through a summing interaction, travelling CFI modes of a very broad band of wavenumbers could be produced, resulting in the rapid spectral broadening. Additionally, the interaction of stationary and travelling CFI modes usually leads to the formation of a low-frequency mode, the so-called type *III* mode. This mode is typically located in the inner upwelling region of the stationary vortex structure, where the spanwise velocity gradient shows a local maximum (figure 1.6(c)). In contrast to aforementioned secondary modes of type *I* and type *II*, the type *III* modes are characterized by low-frequencies and more upstream initiation. Compared to secondary modes, the type *III* modes appear as not very effective in the transition break down, though they usually feature significant amplitudes and are more active upstream. Still, it should be noted that transition can be initiated by the super-harmonics evolved from type *III* modes, which are essentially type *I* modes [9].

Several studies have been dedicated to the interaction between stationary and travelling CFI modes, which are driven by various models and flow conditions. Nonetheless, a common finding among these studies is the universal influence of the initial amplitudes of both modes on their subsequent interactions. Malik et al. [60] conducted a numerical investigation into the interaction of stationary and travelling CFI modes by manipulating their initial amplitudes. Their findings revealed that when travelling CFI modes featured smaller initial amplitudes (10 times weaker) than stationary CFI modes, the interaction appeared relatively weak, causing stationary CFI modes to saturate at slightly lower Re. However, a significant change was observed when travelling CFI modes had comparable or even higher amplitudes. In such scenario, these travelling CFI modes tended to suppress the growth of stationary CFI modes, resulting in an earlier saturation of both primary modes. The effect of high-amplitude travelling CFI modes on the growth and saturation of stationary CFI modes was experimentally observed by Deyhle & Bippes [25] and Downs *et al.* [33]. The experimental investigation of Deyhle & Bippes [25] revealed a practical transition delay when the freestream turbulence intensity T_u increased from 0.08% to 0.15% (i.e. stronger travelling CFIs). Nonetheless, outside of this range, the transition was actually promoted. It should be noted that in these transition delay cases, the surface roughness was essentially non-negligible and the resulted stationary CFI modes indeed saturated at lower amplitudes. As a result, this delay was attributed to the previously mentioned suppression effect of travelling CFI modes on stationary CFI modes.

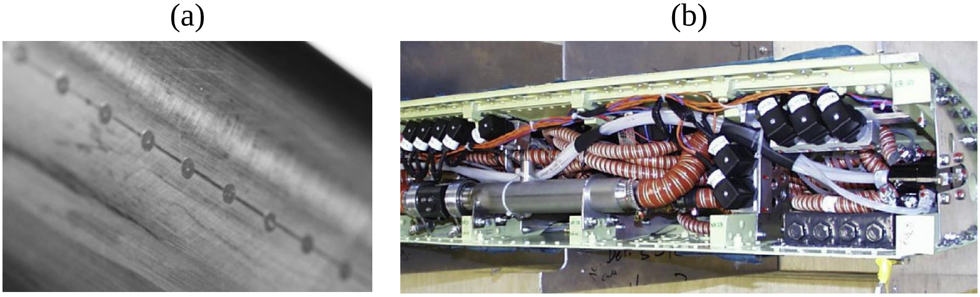

FIGURE 1.9: (a) Photograph of the DREs mounted on the wing leading edge, re-adjusted from [84]; (b) Leading edge of the Do 228 test aircraft equipped for LFC flight test [53].

In the context of the current work, two distinct scenarios can be categorized based on the strength of stationary and travelling CFI modes. The first scenario is characterized by dominant stationary CFI modes with weak travelling CFI modes, corresponding to clean cases (i.e. without plasma control). On the other hand, the second scenario still involves strong stationary CFI modes, though accompanied by strong travelling CFI modes due to the intrinsic unsteadiness of plasma actuator (section 1.3.4).

1.3. CONTROL OF CROSSFLOW INSTABILITIES

The important deterministic role of CFIs in swept wing boundary layers makes it a straightforward task to mitigate these instabilities to delay transition and consequently the drag reduction of swept wings. Therefore, any device or method that effectively suppresses CFIs holds significant potential in achieving this goal.

1.3.1. LAMINAR FLOW CONTROL (LFC)

One promising technique to achieve this goal is the Laminar Flow Control (LFC). This term widely refers to techniques that could effectively maintain laminar flow over aerodynamic bodies at higher *Re* at which the laminar flow will be lost without LFC, ultimately achieving the transition delay. Originally, this involved suction devices for transition delay in aircraft design [47]. In the context of this work, the term of LFC is broadly used to encompass all passive and active flow control methods aimed at transition delay. A review of early experiments and flight-tests regarding LFC is given by Joslin [47], along with a more recent review by Krishnan *et al.* [53].

In recent decades, significant achievements of LFC have been made in the field of swept wings. The main contributions are briefly summarized here, but not limited to. One notable achievement is the introduction of DREs as a passive control method, as shown in figure 1.9(a). Saric *et al.* [79] first installed these DREs near the stagnation point to stimulate sub-critical stationary CFI modes, which feature smaller wavelengths and are less unstable than critical stationary modes. As a result, the growth of dominant critical stationary CFI mode was attenuated by the control mode (i.e. sub-critical stationary CFI mode), resulting in substantial transition delay.

The efficacy of DREs was later verified by several numerical studies [46, 61, 94]. To encompass a broader range of all capable passive/active devices, the more generalised term Upstream Flow Deformation (UFD) was introduced by Wassermann & Kloker [94], essentially following the same control mechanism of DRE. One such device, discrete suction holes, has been demonstrated to stimulate sub-critical CFI modes and effectively delay transition [56, 63]. The effectiveness of such suction method significantly depends on the suction rate. A larger suction rate generally enhances the boundary layer stability, however, a threshold is recommended as oversuction was found to trigger premature transition [63].

Furthermore, the growth of secondary CFIs exhibits a remarkable sensitivity to the small wall-normal and CF velocity components of primary stationary vortices [9, 37]. This finding unveils the potential for efficient transition control by locally manipulating the already non-linearly developed CF vortices (thus controlling secondary CFIs). One such technique is pinpoint suction, which locally modifies the shear layer and exert control over secondary CFIs. The work of Friederich & Kloker [37] achieved transition delay through the pinpoint suction holes, which are located below the updraft side of CF vortices. The results indicate that the pinpoint suction doesn't directly weaken the CF vortex rotation. Instead, it leads to the formation of a pair of counter-rotating vortices, with one hindering the target stationary CF vortex rotation while the other one naturally decaying. It should be noted that the impact of such suction differs from the cancellation observed in two-dimensional flows, which is achieved through the anti-phase/counter-rotating vortex.

Alternatively, the mitigation of CFIs can be achieved by directly targeting the underlying CF component itself, as it serves as the source of CFIs. One effective technique for this purpose is homogeneous suction (e.g. suction slit). Messing & Kloker [63] investigated this method through Direct Numerical Simulations (DNS). The results indicate that, when suction is actively employed, the CF component experiences a reduction scaled to suction rate. Additionally, the streamwise velocity profile becomes fuller at the wall, which is a distinctive outcome of homogeneous suction. As a result, such suction stabilizes the boundary layer by dampening both stationary and travelling CFI modes. Specifically, when considering stationary CFI modes, the damping effect is heavily influenced by the spanwise wavenumber, whereas it exhibits a relatively negligible dependence on the frequency of travelling CFI modes.

Although the effectiveness of the mechanisms behind these methods has been established, it should be noted that the control devices utilized (to implement these mechanisms) do show disadvantages in certain scenarios. For instance, as a passive technique, DRE-based LFC is expected to work only in specific flight conditions and can be less effective or even detrimental in off-design conditions. On the other hand, the suction-based LFC turns out as a highly interdisciplinary task in spite of its flexibility and adaptability to various environment conditions. The corresponding suction system is typically complicated (e.g. piping, compressor and valves, as shown in figure 1.9(b)) and brings additional demands of geometry and manufacture (e.g. hole quality, system weight and volume), challenging the design and practicality of suction-based LFC.

In summary, the aforementioned methods reveal the potential of LFC for swept

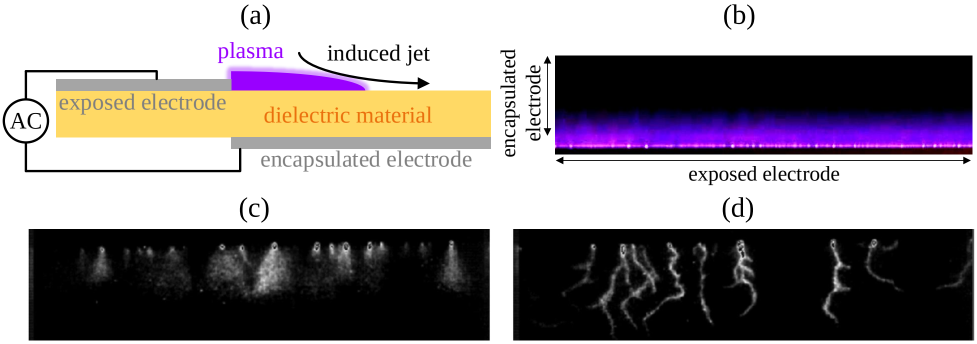

FIGURE 1.10: (a) Schematic of typical DBD PA (side view); (b) Photograph of the plasma discharge, re-adjusted from [21]; (c) High-speed photograph of DBD discharge in the negative AC circle; (d) High-speed photograph of DBD discharge but in the positive AC circle. (c) and (d) are re-adjusted from [35].

wing transition control. Nonetheless, the performance and practicality of LFC can be significantly improved by deploying alternative active control devices, which ought to be simpler and more robust.

1.3.2. DIELECTRIC BARRIER DISCHARGE PLASMA ACTUATORS

The Dielectric Barrier Discharge (DBD) plasma actuator (PA) has wide applications across various fields, such as ozone generation, surface treatment and so on [48]. In recent years, DBD PA has garnered significant attention in LFC concepts. Specifically, the AC-DBD configuration (powered by alternating current (AC) power) is commonly employed in aerodynamic applications due to the plasma-generated body force. This active flow control device offers numerous advantages, such as flush-mountable, fast response and full electric operation without mechanically driven parts [6, 20, 49]. These inherent advantages make DBD PA a promising candidate of active flow control device for implementing the aforementioned LFC methods.

A typical 2D configuration of DBD PA consists of two flush-mounted electrodes separated by a dielectric material, as depicted in figure 1.10(a). One electrode is exposed to the surrounding air and connected to high voltage, while the other electrode is encapsulated and connected to ground. Upon applying sufficiently high voltage, electrical breakdown occurs and generate charged particles. The presence of dielectric layers plays a vital role as it allows for the charge accumulation on dielectric material surface, mitigating the local electric field and suppressing the discharge process. This inherent self-limiting characteristic of DBD PA prevents the formation of electric arcs by prohibiting the cascade of charges. On the other hand, it necessitates the use of AC voltage to sustain plasma. During the negative AC cycle, electrons migrate from the exposed electrode towards the dielectric material surface, whereas the opposite occurs during the positive cycle. It is important to note that electrons exhibit greater mobility when departing from the exposed electrode compared with the dielectric surface [20]. As a consequence, during the negative AC cycle, the glow-like discharge takes place while the streamer discharge is ignited during the positive AC cycle [6, 20],

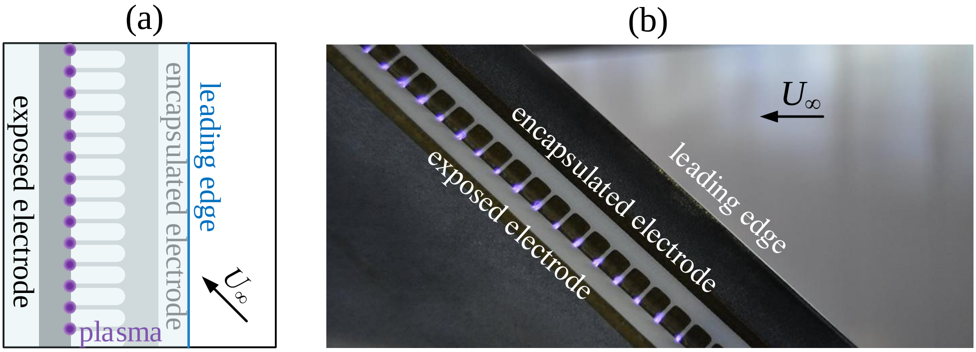

FIGURE 1.11: (a) Schematic of PA designed for UFD strategy; (b) Photograph of the UFD-based PA installed on the swept wing model $M3J$, re-adjusted from [84].

as shown in figure 1.10(c) and (d).

During the plasma ignition, the collision between charged and neutral particles within the discharge volume results in the transfer of momentum, giving rise to a Coulombian electro-fluid-dynamic (EFD) body force [97]. This body force holds significant importance in the practical implementation of DBD PA for flow control purpose. Specifically, the generated body force exhibits asymmetric characteristics in positive and negative AC cycles due to the aforementioned distinct discharge modes. Enloe *et al.* [36] reported a push-push scenario whereas Neumann *et al.* [66] found a push-pull scenario. The variations observed in these studies emphasize the significance of considering factors such as local pressure gradients and viscous forces when estimating the body force using velocity data [49]. Nevertheless, considering that the gas discharge processes occur at much smaller spatial and temporal scales (4-8 orders of magnitude) compared to resulting airflow scenarios, the plasma body force approximately imparts quasi-steady momentum to the surrounding airflow [89]. This ultimately gives rise to a weak jet of maximum velocity in the order of several meters per second, largely parallel to the dielectric wall [92]. This distinctive behavior forms the essence of all flow control methods, aiming to manipulate the flow field properties through the utilization of dielectric barrier discharges [52].

1.3.3. PLASMA-BASED LFC FOR CROSSFLOW INSTABILITIES

To date, most of plasma-related studies and applications are executed in 2D boundary layer conditions, such as the active cancellation of Tollmien–Schlichting waves [39, 51], or boundary layer separation control [43]. The attempts and studies of plasma-based control on CF-dominated boundary layers have started more recently. Until now, several strategies of plasma-based LFC have been proposed to target CFIs and are summarised below.

Upstream Flow Deformation Strategy

This method directly follows the mechanism of the aforementioned passive DRE-based LFC and UFD-suction LFC techniques. By exciting sub-critical CFI modes,

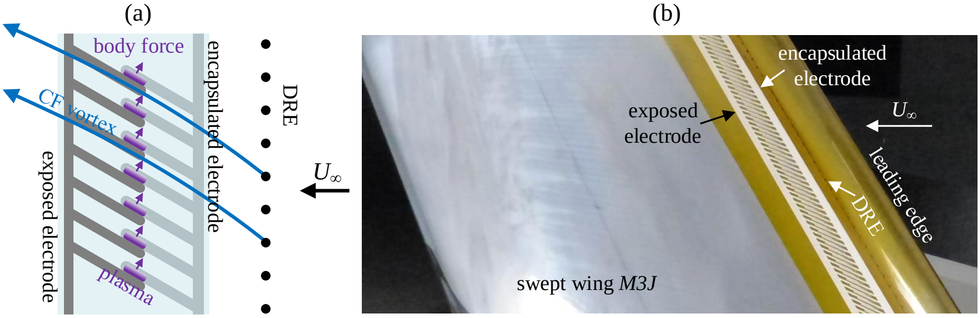

FIGURE 1.12: (a) Schematic of PA designed for direct attenuation strategy; (b) Photograph of PA installed on the swept wing model *M3J*, in the context of direct attenuation strategy.

the growth of critical CFI modes is suppressed, thereby achieving transition delay. Figure 1.11(a) illustrates the schematic of a typical PA configuration for UFD strategy and (b) shows the UFD-based PA installed on the swept wing model *M3J*. The first experimental investigation came from Schuele *et al.* [82] where stationary CFI modes were successfully excited by micrometric-sized PAs on a right-circular cone operating at the Mach of 3.5. A similar approach was followed by Serpieri *et al.* [87] where various stationary CFI modes were plasma-conditioned on a swept wing model. Nonetheless, the efficacy of plasma-based UFD strategy is mainly demonstrated by numerical researches. Dörr & Kloker [32] suppressed critical stationary CFI modes and decreased skin friction in a DNS model, where the distributed PAs successfully excited sub-critical stationary CFI mode as the control mode. The results showed that the PA forcing in both anti-CF and co-CF direction can delay transition though the anti-CF forcing further reduced the mean CF component. Expanding on their previous work, Dörr *et al.* [31] applied discrete PAs on the boundary layer dominated by travelling CFIs. It was found that the PA forcing in both directions could significantly damp the growth of travelling CFIs. The outcome demonstrated the stabilising effect of deformed mean flow which appeared after the plasma-induced sub-critical modes. Following the same approach, Shahriari *et al.* [88] demonstrated the successful transition delay by the sub-critical modes induced by ring-type PAs in numerical simulations. Additionally, sub-critical travelling CFI modes were also found beneficial for delaying transition. In the numerical work of Guo & Kloker [40], the anti-CF PAs excited a positive sub-critical travelling CFI mode as the control mode. The results demonstrated the ability of sub-critical travelling CFI mode to suppress both critical stationary and travelling CFI modes, thus achieving the skin friction reduction.

Direct Attenuation Strategy

This strategy is targeted towards directly attenuating the rotational strength of primary stationary CF vortices. In other words, the PA works in the direct opposition mode, analogous to the Tollmien-Schlichting wave cancellation techniques applied in 2D boundary layers [39, 51]. A schematic of the typical PA configuration for the direct attenuation strategy is illustrated in figure 1.12(a). Dörr & Kloker [30] achieved the reduction of stationary CF vortices by configuring the PA forcing in both

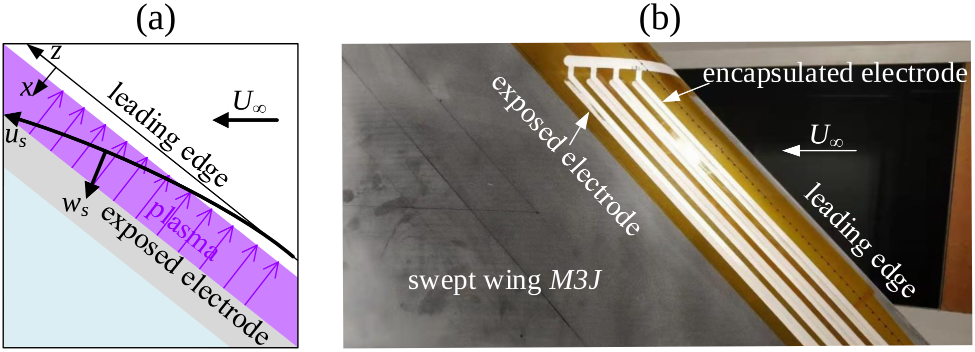

FIGURE 1.13: (a) Schematic of PA designed for BFM strategy; (b) Photograph of the BFM-based PA installed on the swept wing model $M3J$.

co-CF and anti-CF directions (the anti-CF case is shown in figure 1.12(b)). The PA position (w.r.t the local CF vortex axis) was found to be a key parameter in reducing the CF vortex circulation. The optimal spanwise position of PA was investigated by Wang *et al.* [93] where the Non-Linear Parabolized Stability Equations (NPSE) combined with sensitivity analyses were solved. While the previous studies have been largely numerical, Yadala *et al.* [98, 100] experimentally achieved transition delay with a comb-type PA which forced a sub-critical mode. However, no clear sub-critical modulation was observed though the transition was delayed about 3.5% of the chord length. Guo & Kloker [41] argued that the success of Yadala *et al.* was more related to the direct attenuation strategy, due to the strong dependence of the transition delay on spanwise phase of PAs.

Base Flow Modification Strategy

In the Base Flow Modification (BFM) method, the PA is installed near the leading edge and configured to directly oppose the base flow CF component. This method is analogous to the aforementioned homogeneous suction approach where the CF component is reduced. By reducing the CF component, the BFM strategy directly stabilizes the boundary layer. Figure 1.13(a) illustrates a typical PA configuration for BFM and (b) shows the BFM-based PA installed on the swept wing model $M3J$. As shown in figure 1.13(a), close to the attachment line of swept wing leading edge, inviscid streamlines are directed almost parallel to the leading edge (i.e. z axis). As such, the PA forcing perpendicularly to the leading edge (i.e. -x direction) can be utilised to directly counter the CF component. However, it should be noted that, the discrete, spanwise-modulated PA configurations adopted in the aforementioned UFD and direct attenuation strategies have been found to perform a local BFM action as well [41]. By doing this, the discrete PA needs to be carefully placed in relation to the incoming CFIs, to avoid triggering undesired stationary CF vortices [29]. The CF reduction is supposed to impose a global stabilisation on the boundary layer, thus suppressing the growth of both stationary and travelling CFIs. In an early numerical work of Dörr & Kloker [29], the CF component was reduced by sub-critically spaced PAs, modelled as steady volume distributed body forces. The boundary layer stabilisation was found to invoke a combination of base flow deformation and 3D flow modulation (i.e. the conditioning of sub-critical modes). Yadala *et al.* [99] were the first to experimentally demonstrate transition delay on a swept wing model using 2D straight PA in the BFM configuration. A simplified numerical model (first proposed by Serpieri *et al.* [87]) combined with the experimentally-characterized body force distribution additionally confirmed the general stabilisation of plasma-based BFM on CFIs. Serpieri *et al.* [87] operated a 2D straight PA at high forcing frequency (f_{AC}) while the low-frequency velocity fluctuations were found amplified downstream. By means of linear stability theory (LST) and a simplified body force model, the authors attributed the low-frequency fluctuations to plasma actuator inherent unsteadiness. Baranov *et al.* [4] placed the so-called multi-discharge actuator (MDA) at sub-critical spacing at a downstream position where the spatial amplification of critical modes reached the maximum. As a result, the mean CF component was reduced and critical stationary CF vortices were suppressed without triggering significant sub-critical modes. However, the uncontrolled and seemingly random unsteady disturbances produced by the MDA resulted in an earlier development of secondary CFIs thus triggering earlier transition. By estimating the transition movement and the net power gain from drag reduction, Yadala *et al.* [100] found the BFM strategy to be more robust but less effective than the UFD strategy, due to the higher input power.

In spite of the effectiveness and advantages of plasma-based LFC for swept wing transition control, the above mentioned strategies have their own limitations, in need for further improvement. The UFD strategy imposes strict requirements for the manufacturing and dimensioning quality of the actuator (e.g. the ’cross-talk’ phenomenon, where parasitic reverse plasma will be created if electrodes are too narrowly spaced, [5]). Recent improvements in designing PAs for controlling the CF component and CFIs can be found in the work of Baranov *et al.* [4] and Guo & Kloker [41]. Similarly, the direct attenuation strategy requires to localise the PA at desired positions with respect to the natural CF vortices, which can become unrealistic in operational flight conditions where the phase or wavelength of incoming CFIs is unknown. In contrast, in view of actuator manufacturing and design considerations, the BFM strategy appears to be the most applicable and robust method, albeit requiring higher energy input to manipulate the base flow, compared to direct instability control methods.

1.3.4. Non-deterministic Unsteady Perturbations due to Plasma Actuation

The application of plasma-based LFC in realistic flight environments brings forth further complications. One of the largely unknown factors which influences the efficacy of all plasma-based LFC is the introduction of non-deterministic unsteady flow disturbances. Specifically for the AC-DBD PAs, the PA forcing comprises two parts, namely the steady and unsteady components. One of the sources of unsteady components can result from the AC power frequency f_{AC}, which is controllable. The work of Dörr & Kloker [30] demonstrated that the unsteady component caused by f_{AC} had negligible effects on the boundary layer when a sufficiently high f_{AC} was selected (e.g. exceeding frequencies of the most amplified primary travelling CFIs and secondary CFIs). Nonetheless, the experimental study of Serpieri *et al.* [87]

still observed the enhancement of travelling CFIs due to the PA operation, even though the PA was operated at very high f_{AC}. This revealed that the unsteady component of PA forcing can result from other PA unsteadiness (instead of f_{AC}), which is not controllable. Based on a simplified body force model and corresponding LST analysis, Serpieri [84] attributed the unsteady disturbances to the inherent unsteadiness of the PA forcing, possibly related to the stochastic dynamics of the electrical discharge. This assumption was later confirmed by Moralev *et al.* [64]. Using the cross-spectra analysis, they traced the origin of the random unsteady disturbances to the quasi-stochastic nature of PA micro-discharges. Considering that the micro-discharge formation is an inherent feature of typical DBD PAs, the effects of these unavoidable disturbances on the boundary layer require further investigation. This becomes particularly pertinent when the frequency of these stochastic disturbances overlaps with those of the most amplified travelling CFIs. Moreover, these unsteady disturbances could quadratically/non-linearly interact with stationary CFIs, resulting in the rapid spectral broadening of the perturbation system and eventual transition to turbulence, as found by Corke *et al.* [19] and Arndt *et al.* [2]. This complexifies the transition control goal and needs to be further investigated.

1.4. MOTIVATION AND LAYOUT

1.4.1. MOTIVATION AND OBJECTIVES

As summarized in section 1.3.3, compared to other plasma-based LFC techniques, the BFM strategy exhibits promising applicability and robustness in terms of actuator design and fabrication. This makes it a highly promising candidate for LFC in modern transport aircraft. Nonetheless, comprehensive and systematic studies of plasma-based BFM are limited, even though prior research has shown its potential in controlling flow over swept wings. This doctoral dissertation presents experimental investigations and analyses of the BFM manipulation on swept wing boundary layers at subsonic conditions. Particular attention is given to the development and alteration of CFIs and laminar-turbulent transition. The successful operation of the PA and characterization of the altered flow field provide valuable insights into the interaction between the PA forcing and swept wing boundary layer. The outcomes provide a foundation for practical application and improvement of such technique, which aims to delay the laminar-turbulent transition and eventually to reduce fuel consumption. The present work was mainly guided by four primary research objectives respectively presented in three chapters:

- **Objective A/ Clarify the nature of unsteady perturbations induced by PA.** This objective is dedicatedly investigated in Chapter 4. Given the inevitable nature of intrinsic PA unsteadiness (section 1.3.4), the practical implementation of plasma-based BFM becomes notably intricate. Consequently, the elucidation of the development of plasma-induced disturbances is chosen as the first step, aiming to establish a comprehension of the dependency of their physical characteristics and impacts on key parameters (e.g. the applied voltage frequency f_{AC} and the forcing location). To resemble the realistic flight conditions, such investigations should be implemented within swept wing boundary layers dominated by stationary CF vortices.

The PA is required to operate at significantly low power to minimize the net BFM effect, thus isolating the purely detrimental unsteady forcing effects.

- **Objective B/ Experimentally confirm the direct effect of plasma-based BFM on the boundary layer.** This work is mainly described in Chapter 5. Though the BFM strategy was experimentally demonstrated to delay transition [99], the direct effects of an operating PA on the CF component of swept wing boundary layers have yet to be characterized experimentally. Furthermore, a comprehensive understanding of the working principle of plasma-based BFM needs to be achieved by establishing the relationship between PA operating parameters and eventual base flow modifications, such as streamline-aligned velocity component, CF component and base flow direction.
- **Objective C/ Clarify the effects of PA forcing on crossflow instabilities.** This objective is mainly investigated in Chapter 5 and Chapter 6. PA effects have crucial roles in the stabilization and development of swept wing boundary layers. A comprehensive understanding of the PA effects on CFIs need to be achieved by establishing the dependency of stationary and travelling CFIs' alterations on PA operating parameters as well as the local flow characteristics.
- **Objective D/ Clarify the effects of BFM PA forcing on laminar-turbulent transition.** This objective is mainly investigated in Chapter 6. Several key parameters (e.g. Reynolds number, stationary CFI modes' wavelengths and wing angle of attack) need to be identified for the ultimate understanding of PA effects on transition. Corresponding influences of these parameters need to be meticulously examined to uncover their significance for transition characteristics such as the topology and location.

1.4.2. Thesis organization

The structure of this dissertation is outlined as follows: Chapter 2 delves into the methodology employed throughout the execution of the experiments and the subsequent data processing. Chapter 3 details the design and performance of the scaled model $K-M3J$. Chapters 4 to 6 encompass an in-depth depiction and analysis of the conducted experiments, addressing each of the primary research objectives presented in this dissertation. Chapter 7 provides a comprehensive overview of the principal discoveries and offers insight into the potential directions for future research endeavours.

2

METHODOLOGY

The majority of this study relies on experimental work. In this Chapter, employed facilities and experimental techniques are introduced, along with an introduction of key post-processing techniques of measured data. Additionally, the simplified body force model and linear stability theory are briefly introduced, which augment the experiment design and data analysis.

2.1. EXPERIMENTAL SETUP

The research undertaken within this thesis primarily stems from comprehensive experimental investigations, complemented by the inclusion of theoretical computations. This synergy enables a comprehensive understanding of the subject matter. The upcoming section presents a thorough overview of the experimental setup. This encompasses details of the wind tunnel facility, swept wing models, manufacture processes of surface roughness arrays and PAs, measurement techniques, followed by the numerical solution. Comprehensive reviews on these equipment and techniques can be found in the work of Serpieri [84], Yadala [97], Rius Vidales [76] and Zoppini [101]. Additionally, to facilitate subsequent discussions, a general notation guideline is established here. The terms PA-*off* and PA-*on* are used to refer to scenarios where PA is not activated and activated, respectively. The quantities at conditions of PA-*off* and PA-*on* are distinguished by the subscript *off* and *on* respectively.

2.1.1. WIND TUNNEL FACILITY

Two distinct wind tunnel facilities have been employed. To elaborate, experiments detailed in Chapter 4 and Chapter 6 were conducted in the low-speed Low Turbulence wind Tunnel (LTT). Conversely, the experiments detailed in Chapter 3 and Chapter 5 were conducted within the Anechoic Vertical Tunnel (A-tunnel). Both LTT and A-tunnel are located at the Low Speed Laboratory (LSL) of Delft University of Technology. Particularly, the LTT facility is an atmospheric, closed-loop and subsonic tunnel, comprising a test section featuring the dimension of 2.60 m × 1.80 m × 1.25 m in xyz. The incorporation of seven dedicated anti-turbulence screens ensures that the flow within the test section maintains a low freestream turbulence intensity T_u ($< 0.03\%$) under free-stream conditions of current experiments (i.e. $25\,\mathrm{m/s} \leqslant U_\infty \leqslant 55\,\mathrm{m/s}$), as reported by Serpieri [84]. Such low T_u is necessary to create flows dominated by stationary CFIs due to the distinct receptivity process of primary stationary and travelling CFIs. More comprehensive reviews of LTT's characteristics can be found in the work of Dobbinga [27] and Rius Vidales [76].

On the other hand, the A-tunnel is an open-jet, closed-circuit, vertical wind-tunnel, which is mainly meant for aeroacoustic measurements, fundamental studies in laminar-turbulent transition and flow control. The circular wind tunnel outlet features a diameter of 0.60 m and allows for interchangeable nozzles of various dimensions that can be flush-mounted to the contraction exit. For the present experiments, the nozzle with the dimension of 400 mm × 700 mm has been employed. Under the freestream conditions of $18\,\mathrm{m/s} \leqslant U_\infty \leqslant 22\,\mathrm{m/s}$, the corresponding turbulence intensity remains lower than 0.10% owing to the four anti-turbulence screens arranged at an interval distance of 200 mm [62]. For a deeper exploration of the A-tunnel's capabilities, a comprehensive review can be found by Merino-Martínez *et al.* [62].

2.1.2. SWEPT WING MODEL $M3J$

The employed swept wing model in Chapter 4 and Chapter 6 is an in-house designed 45° swept wing model, known as the 66018$M3J$. Alternatively, the swept wing model used in Chapter 5 is the K–$M3J$, a scaled model of $M3J$, which is specifically designed for the A-Tunnel and experiments focusing on PAs. The design and characteristics of

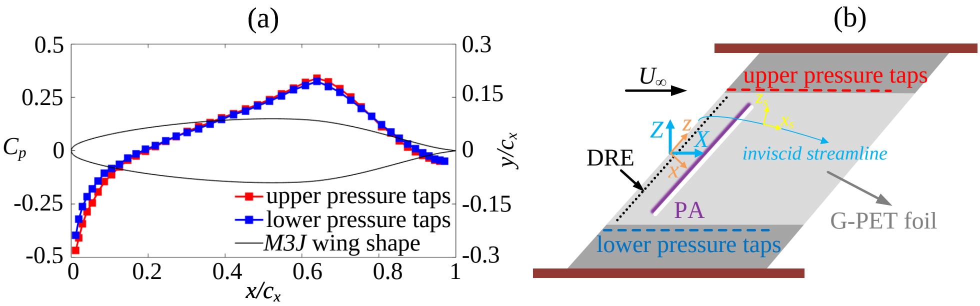

FIGURE 2.1: (a) $M3J$ cross-section (in the x direction) with pressure coefficients measured by the lower and upper pressure taps at $\alpha = 3.3°$, $Re = 2.17 \times 10^6$; (b) Diagram of $M3J$ with PA installed in the test section of LTT. Red and blue dashed lines illustrate locations of upper and lower pressure taps.

the $K{-}M3J$ will be described in Chapter 3. The $M3J$ model essentially derives from a modification of *NACA* 66018 and has been extensively used in related experiments by the author's research group, serving as a robust tool for delving into the physics of CFIs and LFC techniques. The $M3J$ model is only briefly described here and a comprehensive review of parameters and characteristics of $M3J$ is given by Serpieri & Kotsonis [85].

This model is fabricated from glass-fiber reinforced epoxy resin and coated by black polyester gel. Due to the high sensitivity of CFIs to surface roughness, the model surface is carefully polished to a final low roughness level, where a root-mean-square (rms) roughness of $Rq \approx 0.2\,\mu$m is confirmed by surface profilometer measurements [76]. Figure 2.1(a) illustrates the cross-section of the $M3J$ with experimental pressure coefficients, while figure 2.1(b) depicts the diagram of the $M3J$ installed in the LTT test section. Notably, the leading edge of the $M3J$ incorporates a small curvature radius, primarily designed to mitigate the potential attachment line contamination. The fully convex surface near the leading edge effectively suppresses Görtler type instabilities. Compared to the original *NACA* 66018, the position of the maximum thickness point has been moved downstream. This alteration aims to ensure a favourable pressure gradient along a substantial portion of the wing chord at the preferred angles of attack. By doing this, the growth of TS waves is mitigated while CFIs are favoured in the swept wing boundary layer. The pressure distributions are captured by two rows of distributed pressure taps positioned along the lower and upper sides of the wing span (indicated by red and blue lines in figure 2.1(b)). When placed at mild angles of attack, the $M3J$ model exhibits a uniform spanwise pressure distribution even without wall liners. One example of such pressure distributions is shown by the pressure coefficient C_p in figure 2.1(a). The virtually invariant pressure coefficients guarantee the infinite swept wing condition at the measured condition ($\alpha = 3.3°$ and $Re = 2.17 \times 10^6$). The acquired pressure distributions can be further used to calculate the boundary layer edge velocities, the input required by the simplified numerical model (section 2.5.1).

Due to intricate nature of swept wing models and diverse measurement methods, three reference coordinate systems are employed in this study, as depicted in figure 2.1(b). The first coordinate system (blue) is essentially aligned with the wind tunnel test section and denoted as XYZ. The airfoil chord in the X direction is denoted as c_X, while the corresponding velocity vectors are represented by $[U\,V\,W]$. The second system (orange) is body-fitted to the swept wing model and denoted as xyz, where y is aligned normal to the local surface of the wing. The airfoil chord in the x direction is denoted as c_x, while the corresponding velocity vectors are represented as $[u\,v\,w]$. The last coordinate system (yellow) is aligned with the local inviscid streamline and denoted as $x_s y_s z_s$, with y_s aligned normal to the local wing surface. The corresponding velocity components are denoted as $[u_s\,v_s\,w_s]$. Additionally, it should be noted, under the assumption of a semi-infinite swept wing flow, the two interpretations of the chordwise position essentially hold an identical relationship, i.e. $X/c_X = x/c_x$.

2.2. SURFACE ROUGHNESS CONFIGURATION

For the current work, Polyethylene terephthalate glycol (PETG) foils are employed as the dielectric materials of PAs, covering the wing models. These PETG foils' surfaces are exceptionally smooth, featuring a root-mean-square roughness of 0.02 μm [78]. As a result, stationary CFIs on those swept wing models (essentially on the PETG foil surfaces) are expected to be extremely weak or even undetectable in natural flow conditions (i.e. PA-*off*) due to the receptivity process summarized in section 1.2.3. Therefore, additional stimulus needs to be applied in this study to enhance stationary CFIs. Mainly two types of surface roughness configurations are utilized in this study, namely DRP and DRE. The fabrication and characterization of these roughness patterns essentially follow the procedures reported by Zoppini [101] and are only briefly introduced here.

2.2.1. DISTRIBUTED ROUGHNESS PATCHES

The DRP is only used in Chapter 6 in order to stimulate weaker stationary CF vortices on the *M3J* (compared to those enhanced by DREs). The DRP is simply composited with a layer of spray adhesive (3M Spraymount Spray), which enhances the wing surface roughness through the random deposition of adhesive particles. The corresponding mould employed for spraying takes the form of a rectangular PVC mask, which determines the geometry and position of the DRP. Ultimately, a spray adhesive stripe is generated parallel to the leading edge, spanning from $x/c_x = 0.015$ to 0.025.

In order to characterize the geometric features of the DRP, multiple instances of applied DRP are subjected to scanning by a scanCONTROL 30xx profilometer. This profilometer is equipped with a semiconductor laser featuring a wavelength of 405 nm and a reference resolution of 1.5 μm[1]. During the characterization process, a Zaber traversing system[2] is employed to facilitate the movement of laser scanner, with a step resolution of 15 μm (figure 2.2(a)). The scanning process captures the

---

[1] `https://www.micro-epsilon.com/download/manuals/man--scanCONTROL-30xx--en.pdf`).

[2] `https://www.zaber.com/products/linear-stages/LRQ-E/specs?travel=75-150`

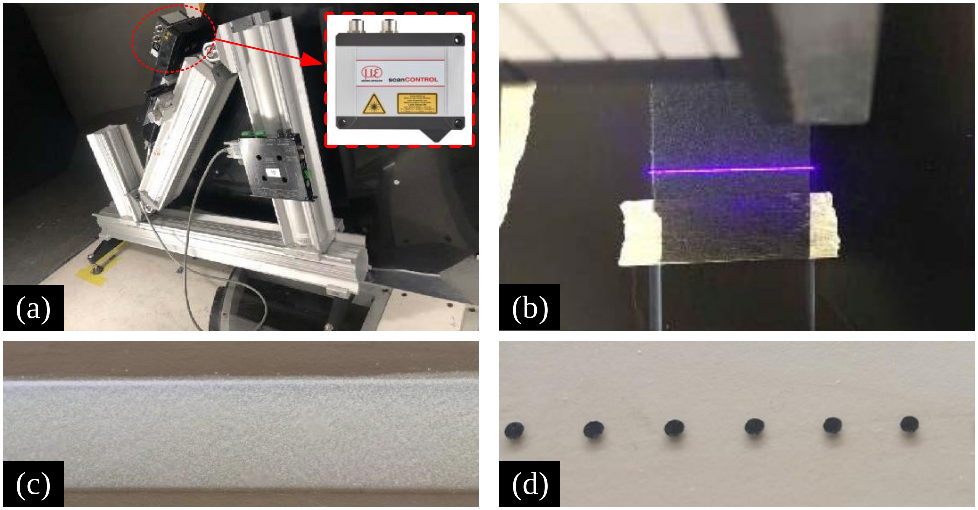

FIGURE 2.2: (a) Photograph of scanCONTROL 30xx profilometer equipped on the traversing system, re-adjusted from [101]; (b) ScanCONTROL laser beam measuring the surface roughness, re-adjusted from [101]; (c) Photograph of the manufactured DRP; (d) Photograph of the manufactured DRE.

local height of the DRP with a step interval of 30 μm. The characterization of the DRP is conducted when it still remains on the PETG foil, which covers the $M3J$ wing model.

The 3D geometry of the DRP is subsequently reconstructed through the measured height signals, which illustrates the shape and spectral features of the DRP. The height of the DRP is estimated by averaging the local DRP height in both spanwise and streamwise directions. Furthermore, Zoppini *et al.* [102] investigated the spanwise spectra of the DRP by Fast Fourier Transform. Their outcomes showed that comparable spectral energies were concentrated within the λ from 0 to 16 mm, exhibiting a spanwise-uniform characteristic. Additionally, owing to the repeatable geometrical features of DRPs, the resulted flow field is likely to be independent of the local patch geometry, as concluded by Zoppini [101].

2.2.2. DISCRETE ROUGHNESS ELEMENT ARRAYS

DRE arrays are thoroughly used in this work to amplify stationary CFIs. The selectivity and efficacy of DRE have been widely demonstrated in previous work [34, 79, 86, 104]. The in-house manufacture procedure of DREs is detailed in the work of Zoppini [101]. In brief, the characteristics of DRE arrays are first designed by a CAD tool (e.g. *Solidworks* in this work). This involves determining key factors like the inter-spacing, numbers and shapes of DREs. The designed configuration is then imported into specialized software developed by Toolbotics, known as Art2gcode[3]. This tool converts the CAD design into a coordinate file compatible with the GLRS

---

[3] Art2gcode: `http://www.art2gcode.com/Art2GcodeV1/v1.html`

system, which directs the operation of the CNC laser cutting machine Tooli[4]. For the cutting material, a self-adhesive black PVC foil[5] with a thickness of 100 μm is employed. To achieve higher elements, multiple layers of PVC foil are straightforwardly affixed together prior to initiating the cutting process. Eventually, the laser-cut strip, comprising both the DREs and the mask, is applied to the wing surface. After removing the mask, only the DREs are left affixed to the wing surface.

The statistical characterization of DREs used in this work follows the study conducted by Zoppini [101], where DREs were produced through the same method. The measurement set-up employed is the scanCONTROL 30xx precision profilometer along with the traverse system, as explained in section 2.2.1. The acquired amplitude signals are processed to extract key parameters including the diameter and height. Additionally, the height is estimated by the distance between the linear fittings of the DRE top surface and wing surface. By fitting the DRE top surface with circular shapes, the diameter is derived when the difference (between the fitting circular shape and the DRE top surface) reaches the minimum.

2.3. PLASMA ACTUATORS

It is evident that the implementation of DBD PAs must maintain a non-intrusive operation within the framework of the plasma-based BFM technique. This places high requirements on the fabrication process, including the need for extremely thin electrodes. Additionally, the effectiveness of PA forcing is notably influenced by the accuracy of the PA electrodes' alignment and dimensions, thus necessitating meticulous attentions in the PA design. In this section, the design and fabrication of PAs are detailed, along with the methods of characterizing the resulting PA body force, which subsequently serve as the input of the simplified body force model (section 2.5.1).

2.3.1. DESIGN AND FABRICATION

For this study, the most typical configuration of DBD PAs is chosen to achieve the BFM technique, as the one illustrated in figure 1.10(a). Nonetheless, due to the distinct geometrical features of $M3J$ and $K{-}M3J$, corresponding PAs are specifically designed and undergo distinct manufacture processes.

Plasma Actuators for Operation on the $M3J$ Wing

The fabrication of PAs for operation on the $M3J$ wing essentially follows the procedure outlined in the work of Yadala [97], with a brief overview provided here. The fabrication procedure comprises three key steps. The first step involves the geometrical design of PA, namely the dimensioning of exposed and encapsulated electrodes. This is achieved by creating vector files through the CAD design software *Solidworks*. These vector files are then converted by *Art2gcode* into GLRS coordinate files for subsequent use in operating the CNC laser cutting machine.

The second step entails the mask generation on a black, self-adhesive PVC foil

---

[4] Tooli machine: `http://www.art2gcode.com/help.toolbotics.com/Home.html`

[5] d-c-fix deco foil. Technical sheet at `https://www.plakfolie.nl/a-53045956/decofolie/velours-folie-zwart-45cm-x-p-m/$#$description`

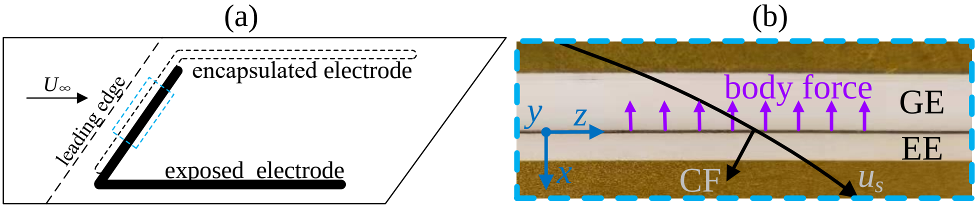

Figure 2.3: (a) Sketch of the whole PA sheet for $M3J$; (b) Zoom-in view (photograph) of PA (the blue dashed box in (a)), along with the body force arrangement in xz plane. EE: exposed electrode; GE: encapsulated electrode; u_s: streamline-aligned velocity.

similar to the type used in the DRE fabrication (section 2.2.2). This black foil is affixed to a 500 μm thick and transparent GPET foil[6], which is used as the dielectric material of PA. The laser tool head operated by the GLRS files, precisely cuts out the geometric shapes of electrodes from the self-adhesive sheet. The laser power and number of passes were carefully chosen to cut only the self-adhesive sheet without affecting the dielectric surface. Thanks to the dielectric material's transparency and thickness properties, the laser can directly pass through it without causing any damage. Therefore, the mask of the encapsulated electrode (adhered to the back side of the dielectric material) can be directly cut by laser, without physically moving the dielectric foil. This improvement yields an exceptionally precise alignment of exposed and encapsulated electrodes, effectively mitigating any potential disruptions in the electric field and ensuring a uniform body force distribution. Once the laser cutting is completed, the cut part of self-adhesive sheets (i.e. electrodes) are removed from the dielectric foil, creating a mask used in the next step.

The final step involves the computer-controlled spraying of the conductive electrodes. A spraying nozzle is attached to the CNC-XY plotter, replacing the laser head. The nozzle is connected to a pressurised air supply and the nozzle pressure is adjusted to 1.2 Pa. The nozzle is fed by a conductive silver coating[7], which is diluted with an industrial solvent (2-Butanone). The silver ink is sprayed onto the mask and the silver particles deposit on the dielectric foil, forming the electrodes once the mask is removed. As demonstrated by the work of Yadala [97], their similar PA fabrication method yields a 6 μm thick electrode for one spray path and 30 μm for five spray paths. In this study, two spray paths are employed to enhance the solidity of electrodes. Given the similarities to the fabrication process of Yadala [97], the PA electrodes for $M3J$ of this study are expected to fall within the range from 6 μm to 30 μm in thickness.

Plasma Actuators for Operation on the $K\!-\!M3J$ wing

In contrast to the labour-intensive process of fabricating PAs for the $M3J$ model, the production of PAs for the $K\!-\!M3J$ model benefits from a specialized printer EcoTank

---

[6] `https://www.vinkkunststoffen.nl/media/import/Datasheet_PetGAG_Caltek.pdf`

[7] `https://hollandshielding.com/Conductive-Silver-Coating`

FIGURE 2.4: Printer EcoTank ET-M1170 and a PVC sheet with PA printed on.

ET-M1170[8] (figure 2.4). Though very powerful and efficient in manufacturing PAs, the practicality of the printer is constrained by its working dimension limits (e.g. A4 format). As a consequence, the printer cannot contribute to the fabrication of PAs for $M3J$.

The corresponding process is extensively outlined by Arkesteijn [1] and briefly introduced here. Similar to the first step detailed in section 2.3.1, the geometry of PA is carefully designed to match the dimension and shape of $K-M3J$. This is done again by *Solidworks* and the drawings are saved as PDF files, which are subsequently employed by the printer. The ink employed by the printer is specially the silver nano particle ink [9]. Specifically, the printer utilizes the NB-TP-3GU100 transparent PET sheets [10] for printing the electrodes. These sheets are characterized by a microporous coating, which facilitates the rapid drying of the conductive silver ink. The printing sheets with electrodes are later affixed together with a dielectric layer PETG, using the adhesive spray glue. PETG is chosen for its excellent dielectric properties and transparent nature through which the alignment of exposed and encapsulated electrodes is ensured. The electrodes produced by this printer exhibit a remarkably smooth finish, featuring a thickness less than 15 nm.

2.3.2. BODY FORCE DISTRIBUTION

In this work, two distinct methods are employed to calculate the body force distribution of PA, depending on the types of Particle Image Velocimetry (PIV) used in the PA characterization. Specifically, in Chapter 5, high-speed time-resolved PIV is employed and the reduced method proposed by Kotsonis *et al.* [50] is used to estimate the body force. Whereas, the low-speed PIV is used in Chapter 6 and the empirical model

---

[8] `https://www.epson.nl/nl_NL/producten/printers/inkjet/business/ecotank-et-m1170/p/26979`

[9] `https://www.mpm.co.jp/electronic/eng/silver-nano/line-up.html`

[10] `https://www.mpm.co.jp/electronic/eng/silver-nano/line-up.html`

optimized by Maden *et al.* [59] is employed to reconstruct the body force. According to the distinct velocity fields used for the body force reconstruction, these two methods are referred to as the time-resolved method and the time-average method in this thesis.

Time-resolved Method

In Chapter 5, a high-speed PIV system captures the instantaneous velocity information required to characterize the induced flow fields. Analyzing the velocity fields with the full Navier-Stokes (NS) equation enables the determination of the body force. The 2D incompressible NS equation with the body force term can be expressed as below:

$$\frac{\partial \boldsymbol{U}}{\partial t} + \boldsymbol{U} \cdot \nabla \boldsymbol{U} - \nu \nabla^2 \boldsymbol{U} = -\frac{\nabla p}{\rho} + \frac{\boldsymbol{F}}{\rho} \tag{2.1}$$

where $\boldsymbol{U}$ is the 2D velocity vector, p is the static pressure, ν is the kinematic viscosity of the fluid and ρ is the fluid density.

To derive the body force, the equation 2.1 should be applied at the initial moments of the PA actuation. At this stage, the flow is anticipated to primarily accelerate in the vicinity of PA body force, while the remainder of the field remains semi-quiescent. Assuming an initial condition of zero velocity, the convective, viscous, and pressure gradient terms could be considered as comparatively negligible, resulting the simplified equation 2.2 from equation 2.1, as depicted below:

$$\frac{\partial \boldsymbol{U}}{\partial t} = \frac{\boldsymbol{F}}{\rho} \tag{2.2}$$

which is basically the Newton's second law.

Time-average Method

In Chapter 6, a low-speed PIV system operating at a sampling frequency $f_s = 15\,\mathrm{Hz}$ is employed to capture the induced flow velocity. In other words, in Chapter 6, the PIV records the steady stage of the PA-induced jet, due to the low f_s of PIV. In contrast to the initial stage of PA actuation, the acceleration term in the Navier-Stokes equation loses its importance once a quasi-steady wall-parallel jet is established, as shown in figure 2.5(a). Consequently, to calculate the body force of such steady-stage flow, the acceleration term could be neglected from the NS equation. Assuming that the influence of the unknown pressure gradient is negligible, the NS equation can be reduced as below [52]:

$$f_x = \rho(u\frac{\partial u}{\partial x} + v\frac{\partial u}{\partial y}) - \nu(\frac{\partial^2 u}{\partial x^2} + \frac{\partial^2 u}{\partial y^2}) \tag{2.3a}$$

$$f_y = \rho(u\frac{\partial v}{\partial x} + v\frac{\partial v}{\partial y}) - \nu(\frac{\partial^2 v}{\partial x^2} + \frac{\partial^2 v}{\partial y^2}) \tag{2.3b}$$

where u and v are the flow velocity components in the x and y axes respectively. Hereafter, the equations are referred to as the velocity-information based model. Due to the fact that f_y is significantly smaller than f_x, the contribution of f_y is widely

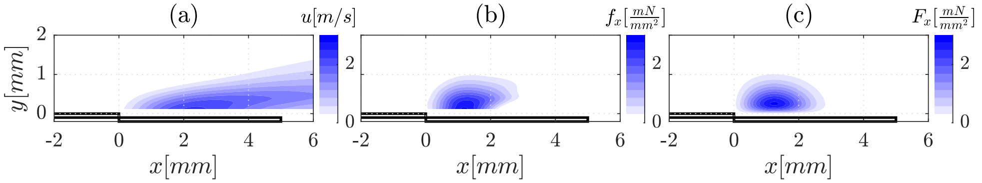

FIGURE 2.5: (a) Wall-parallel jet produced by the PA forcing; (b) Body force distribution f_x derived from the velocity-information based model at $V_{p-p} = 7\,\mathrm{kV}$ and $f_{AC} = 25\,\mathrm{kHz}$ (powered by GBS Electronik Minipuls 4 high-voltage amplifier); (c) Body force distribution F_x optimized by the empirical model based on (b).

considered negligible and therefore has not been taken into account in this study [52]. Figure 2.5(b) illustrates an example of body force derived from the velocity-information based model. Based on the calculated spatial force distribution f_x, Maden *et al.* [59] developed the corresponding empirical model. As depicted in figure 2.5(b), the force distribution initially exhibits a sharp increase as the x (or y) rises, followed by a subsequent decrease after reaching a local maximum. This behavior can be accurately represented mathematically as the product of a polynomial rise and an exponential decay in the x (or y) direction. The equations governing the magnitude and distribution of the force components can be written as follows:

$$X(x) = [a_1x + a_2x^2]\exp(-a_0x^{\alpha}) \tag{2.4a}$$

$$Y(y) = [b_1y + b_2y^2]\exp(-b_0y^{\beta}) \tag{2.4b}$$

where $a_{1,2},\ b_{1,2} \in \mathbb{R}$; $a_0, b_0 > 0$; $\alpha, \beta > 0$; $x, y \geq 0$. As a result, performing a scalar multiplication of these independent one-dimensional functions yields the empirical model of the body force distribution, as below:

$$F_x = cX(x)Y(y), \quad c \in \mathbb{R} \tag{2.5}$$

Equation 2.5 establishes an empirical relationship between the force distribution and spatial domain by determining dependent coefficients (i.e. $a_{0,1,2},\ b_{0,1,2},\ c, \alpha, \beta$) for equations 2.4 and 2.5. These coefficients are later fine-adjusted through a least-square fitting to minimize the disparity between f_x (from the velocity-information based model) and F_x (from the empirical model), automatically matching the resulted force magnitude. The detailed description of the empirical model and corresponding validations can be found in Maden *et al.* [59]. An example of the optimized force F_x from the empirical model is shown in figure 2.5(c).

2.4. MEASUREMENT TECHNIQUES

Multiple measurement techniques are employed during this research and are briefly introduced here. More detailed and complete reviews can be found in Tropea *et al.* [91] and Discetti & Ianiro [26].

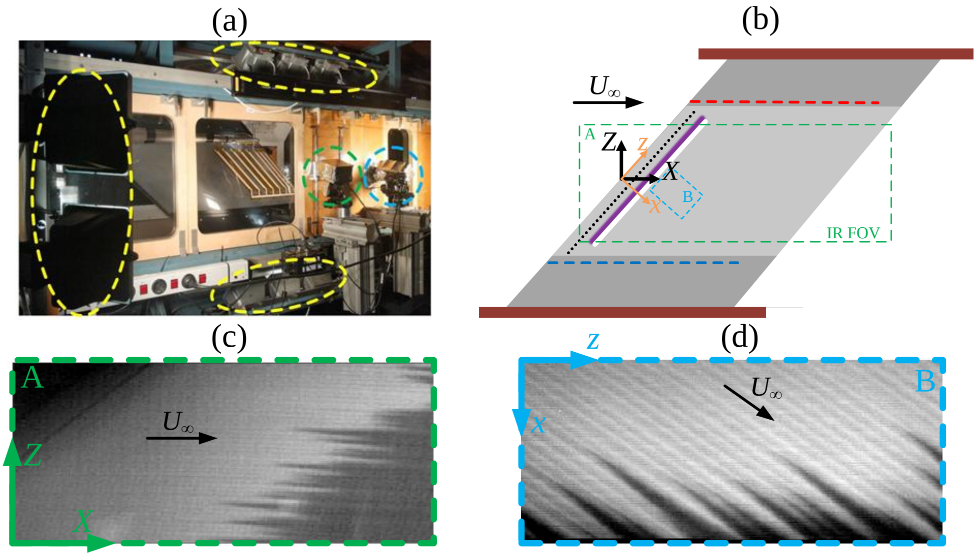

FIGURE 2.6: (a) Experimental set-up used in Chapter 4. The green and blue dashed circles indicate the cameras IR-full and IR-zoom respectively. Yellow dashed circles indicate the halogen lamps; (b) Schematic of IR acquisition set-up for the $M3J$ model. Boxes A and B represent the fields of view (FOV) of cameras IR-full and IR-zoom respectively; (c) Illustrative IR images obtained by cameras IR-full and (d) IR-zoom with the colour scale given by temperature values.

2.4.1. INFRARED THERMOGRAPHY

Infrared (IR) thermography, often referred to as IR thermography or thermal imaging, is a technique that captures and visualizes the infrared radiation emitted by objects and surfaces. It is primarily used for temperature measurement and analysis across diverse applications, one of which is the flow visualization. Specifically, this technique is used to detect stationary CF vortices and transition fronts in this study. Following Reynolds' analogy, high shear flows can be expected to enhance convective heat transfer with respect to low shear flows. When an aerodynamic surface is externally heated, the difference in heat convection rate through the surface skin can be translated into the surface temperature difference. More specifically, due to the higher kinetic energy and wall-shear stress, the turbulent flows enhance the surface heat transfer. This lowers the surface temperature when compared to laminar flow at similar conditions, and vice versa. Therefore, IR thermography can be used to retrieve the stationary CF vortex footprint and the laminar-turbulent transition front, owing to their large impacts on the local shear at the wall. Corresponding theories and applications of this technique in fluid mechanics can be found in Astarita & Carlomagno [3].

IR Thermography Configuration

In this research, the IR technique is mainly used in Chapter 4 and Chapter 6 for the non-intrusive and rapid flow visualization of the $M3J$ model. Two Optris PI640 IR cameras[11] are installed outside of the test section, focused on the wing's pressure

---

[11] `https://www.optris.com/en/product/infrared-cameras/pi-series/pi-640i/`

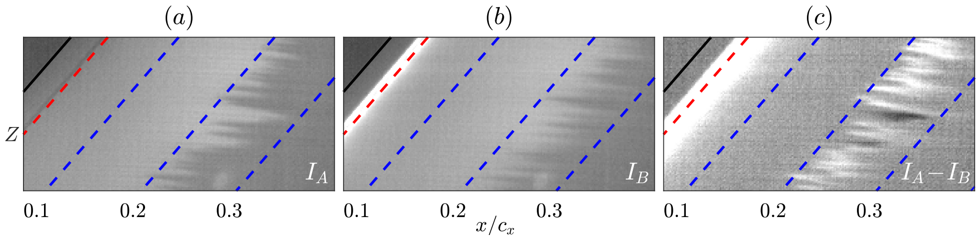

FIGURE 2.7: Time-average IR images of transition front visualization ($\alpha = 2.5°$ and $Re = 3.3 \times 10^6$) for (a) PA *off*; (b) PA *on*; (c) Subtracted IR image of (a) and (b). Flow comes from left and leading edge is shown by the black line. The leading edge and PA location are indicated by black and red dashed lines respectively.

side through small wall openings, as illustrated in figure 2.6(a). These cameras are characterized with a noise equivalent temperature difference (NETD) of 75 mK. Additionally, they feature an uncooled focal plane array (FPA) sensor with a resolution of 640 px × 480 px. Furthermore, these cameras can be equipped with lenses of various focal lengths (41.5 mm, 18.7 mm or 10.5 mm). This flexibility allows for various fields of view (FOV). Specifically, the camera with a wide FOV to observe the transition topology is referred to as camera IR-full ($f_{\#} = 10.5$ mm), while the one with a close-up FOV is referred to as camera IR-zoom ($f_{\#} = 41.5$ mm). A sketch of the FOV of these cameras are illustrated in figure 2.6(b). Several halogen lamps outside of the text section are irradiating the model surface to enhance the thermal contrast between the laminar and turbulent regions, as shown by the yellow dashed boxes in figure 2.6(a). Due to the higher shear stress of turbulent flow, the turbulent region presents lower temperature (darker tone) while the laminar region shows higher temperature (brighter tone), as shown in figure 2.6(c) and (d).

During the experimental measurements, the cameras are recording at a rate of 4 Hz for stationary thermography. These acquired IR images are then averaged and undergo a geometrical transformation to align with the wing curvature. To accomplish this, a calibration sheet was designed and installed on the $M3J$ model. A polynomial distortion correction based on the calibration sheet is applied to the measurement images to correct distortions caused by airfoil curvature and camera position. The outcome of these procedures yields a distortion-corrected time-average thermal map within the analysis region. A comprehensive routine of correcting the IR image distortion can be found in Rius Vidales [76].

Transition Location Identification

In Chapter 4, the transition location is quantified through an in-house developed routine, which is described by Rius Vidales [76]. In general, two sets of IR images are collected at different flow conditions, namely the tested $Re = 2.17 \times 10^6$ and the higher $Re = 2.7 \times 10^6$ respectively. Following the approach of Differential Infrared Thermography (DIT) proposed by Raffel *et al.* [73], the time-average images are mutually subtracted to define the differential image. This technique effectively reduces background noise and minimizes the chances of erroneous transition front identification. By detecting the maximum gradients of the binarized subtraction

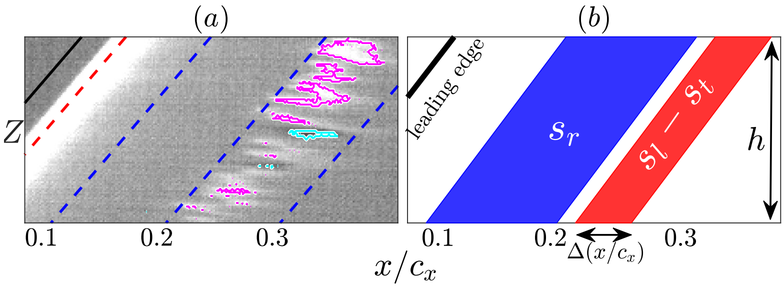

FIGURE 2.8: (a) Gained laminar flow (magenta) and lost laminar flow (Cyan), based on figure 2.7(c); (b) Simple sketch for clarifying the transformation between the net laminar gain and transition location shift (not to-scale).

image, a linear fitting with a confidence band of 95% is subsequently applied and determines the spanwise transition locations. Based on the identified transition location, the plasma-caused transition shift is defined by equation 2.6 and used as a measure of PA impacts on transition.

$$\Delta(x_t/c_x) = (x_t/c_x)_{on} - (x_t/c_x)_{off} \tag{2.6}$$

Net Laminar Gain

In Chapter 6, an alternative approach quantifying the transition shift relies on assessing the net laminar gain. Compared to the previously outlined method, this approach minimizes the experimental workload by eliminating the need for higher *Re* cases and simplifies post-processing procedures. Typical time-average IR images of the transition front are shown in figure 2.7(a) and (b) for PA-*off* and PA-*on* respectively. The bright strip in PA-*on* cases near the leading edge indicates the PA location as well as the model surface temperature increase due to the weak thermal energy deposition of the plasma discharge [49]. Figure 2.7(c) illustrates the IR intensity subtraction ΔI between images (a) and (b). The white area (near the transition front) corresponds to the gained laminar flow due to the transition delay achieved by the plasma-based BFM. Conversely, the black area corresponds to the lost laminar flow (i.e. gained turbulent flow). For this work, the gained laminar area s_l can be roughly identified as regions of $\Delta I > \Delta I_r$ while the lost laminar area s_t is identified as regions of $\Delta I < -\Delta I_r$, where ΔI_r is a threshold value. Variations of the threshold value are tested in order to identify the sensitivity of gained and lost laminar flow areas. Reasonable areas of gained and lost laminar flows can be identified with a threshold between 0.3 and 0.6. As a result, ΔI_r=0.4 is chosen as the threshold for the subsequent processing. Though the threshold of 0.4 is chosen heuristically, it remains constant for the entire parameter range to produce comparable outcomes. Typical results of s_l and s_t are given in figure 2.8(a), outlined by the magenta and cyan lines respectively (at the threshold of 0.4). Consequently, the net laminar gain is calculated as $s_l - s_t$. The net laminar gain is further transformed to the transition location shift $\Delta(x_t/c_x)$ mentioned before. Figure 2.8(b) depicts a simple sketch which aids in clarifying the transformation. Due to the area rule of parallelogram, the transition

(a) Re=2.5 × 10^6

(b) Re=2.5 × 10^6

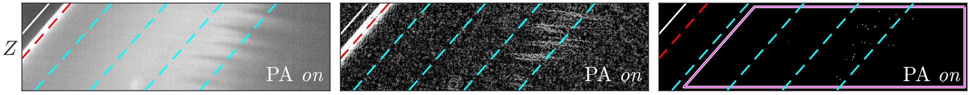

(c) Re=3.3 × 10^6

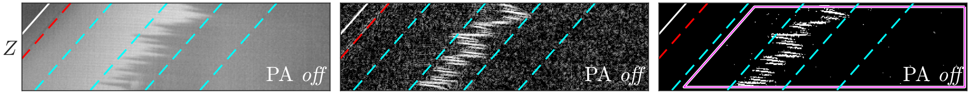

(d) Re=3.3 × 10^6

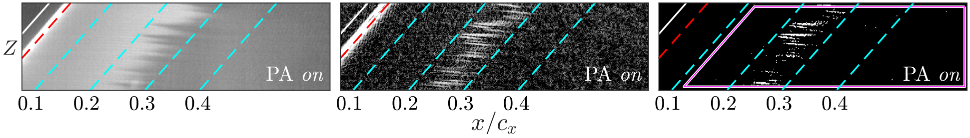

FIGURE 2.9: (a)Transition front identification of Re=2.5 × 10^6 and Re=3.3 × 10^6. Left column: time-average IR images; middle column: IR intensity gradient $|\nabla I|$; right column: filtered IR intensity gradient ($|\nabla I|$>0.25) .

location shift holds a function of the net laminar gain as below:

$$\frac{(s_l - s_t)}{\Delta(x_t/c_x)} = \frac{s_r}{(0.2-0.1)} = h \tag{2.7}$$

where s_r refers to the constant area between x/c_x=0.1 and 0.2 (blue area) and h is the parallelogram height. Consequently, the transition location shift can be calculated by $\Delta(x_t/c_x)$=0.1 × $(s_l - s_t)/s_r$, once $s_l - s_t$ is known.

Transition Front Blurriness

Beyond identification of laminar gain or loss, the use of IR thermography also enables access to the nature of laminar breakdown. More specifically, the loss of spatial coherency in the transition front (i.e. 'blurriness') can be expected to underline a change between a stationary CFI and travelling CFI scenario [10, 34]. As such it is desirable to formalise and quantify this effect. In the field of image processing, a blurred object is characterized by a gradual variation in intensity scale (e.g. IR intensity I in this work) along its outline when compared to a sharp object. In the context of this work, the object is the wedged transition front where a blurred wedge edge is expected to exhibit a relatively smaller gradient compared to a sharp edge. Consequently, the detection of transition front blurriness in this work can be facilitated by simply quantifying the IR intensity gradient at edges of transitional wedges. For all tested cases, the general trend of the transition front follows an angle of 45° with the X axis, highlighting the importance of both x-gradient and y-gradient of I. As a result, the intensity gradient $|\nabla I| = \sqrt{|\frac{\partial I}{\partial x}|^2 + |\frac{\partial I}{\partial y}|^2}$ is calculated for all cases and representative results are displayed in figure 2.9 (the middle column). In general, PA-*off* cases result in intensified $|\nabla I|$ values outlining the typical wedged-transition front, while PA-*on* cases result in minimal $|\nabla I|$ due to the blurred transition front. Similar results of $|\nabla I|$ are found for the majority of tested cases (not shown here for brevity), demonstrating the efficacy of $|\nabla I|$ as an indication of the transition front blurriness. The intensity gradient $|\nabla I|$ is only considered in a mask region (outlined by magenta lines as shown in figure 2.9) to exclude the strong gradient caused by the PA. Within this mask region, the $|\nabla I|$ is focused on sufficiently strong values ($|\nabla I| > 0.25$) to effectively eliminate background noise. The filtered $|\nabla I|$ is illustrated in the right column of figure 2.9. In the context of this work, the $|\nabla I|$ is employed solely as a means to reflect the plasma-caused alteration of transition front blurriness. Thus, any threshold value between 0.2 and 0.28 is deemed appropriate for this goal. In this thesis, the threshold is arbitrarily chosen as 0.25 and maintained consistently throughout the entire processing, ensuring comparable results. Consequently, the average density of $|\nabla I|$ is identified as $|\nabla I|_d = \Sigma|\nabla I|/s_I$, where s_I is the mask area outlined by the magenta lines and $\Sigma|\nabla I|$ refers to the sum of $|\nabla I|$ in the mask region.

2.4.2. Hotwire Anemometry

Hotwire anemometry (HWA) is a well-established flow measurement technique, fundamental in the development of experimental fluid mechanics. This technique relies on a heated wire sensor to determine the fluid velocity by means of convective heat transfer. In detail, the flow probe functions as one of the four resistances of a Wheatstone bridge circuit. The voltage across the bridge is meticulously balanced through a feedback mechanism. With the current passing through, the probe temperature tends to change when the heated probe is exposed to the flow, due to heat convection fluxes. Consequently, this temperature variation leads to alterations in wire resistance, subsequently affecting the voltage across the bridge. The feedback system of the bridge responds to any voltage imbalance by providing an adjusted voltage to the circuit which indirectly reflects the flow velocity. The adjusted voltage can then be converted to the flow velocity through a calibration which correlates bridge voltages with known flow velocities. Although the stability of the tunnel flow conditions is generally guaranteed, the flow temperature and pressure are continuously monitored by specially modified sensors in this study. This monitoring allows for the detection and correction of minor variations that may occur during the calibration or data acquisition process, ensuring an accurate adjustment of the acquired HWA signal. Comprehensive introduction and review of this technique can be found in [57] and [17].

In Chapter 4, HWA measurements are primarily employed to characterize the stationary flow structures as well as unsteady flow perturbations. These measurements are performed by operating a single-wire Dantec Dynamics *55P15* boundary layer probe[12], which is connected to a constant temperature anemometer *TSI IFA-300* equipped with automatic overheat ratio adjustment. The hotwire scan locations are automatically set using an automated traverse system (installed in the wind tunnel diffuser) with a step resolution of 2.5 μm in all three axes of translation. Throughout

---

[12] `https://www.dantecdynamics.com/product/miniature-wire-probe-boundary-layer/`

all measurements conducted, the orientation of the hotwire probe remains aligned with the Z direction. Consequently, at each measurement point, the velocity signal captured by the sensor represents a projection of the instantaneous wing-attached velocity components. These components can subsequently be reconstructed as below [101]:

$$U = \sqrt{(u \times \cos(45°))^2 + (w \times \sin(45°))^2 + (v)^2}. \tag{2.8}$$

Furthermore, it's crucial to implement precautions against potential electromagnetic interference (EMI) from the plasma discharges as well as the wind tunnel noise (e.g. traversing system's stepper motors and the wind tunnel's engine noise). In order to minimize the EMI, the cable connecting the HWA probe is coiled around several toroid magnets, creating a 'coil-like' arrangement. Additionally, it is advisable to place the probe as far away from the PA discharge region as possible and ground all the HWA electrical systems to minimize interference risks.

2.4.3. Particle Image Velocimetry (PIV)

PIV is a non-intrusive optical technique employed to indirectly determine the fluid velocities. This is accomplished by monitoring the displacement of tracer particles that are introduced into and transported by the investigated fluid over a short time interval. In contrast to single-point measurements (e.g. HWA), PIV is capable to provide velocity data that are spatially and temporally correlated in two or three spatial dimensions, depending on the specific PIV type.

Planar PIV

As the word *planar* implies, the planar PIV is used to capture and analyse velocity fields within a two-dimensional plane or a specific cross-section of fluids. The interested flow region is illuminated through a laser light sheet. Camera devices are accordingly positioned perpendicular to the laser sheet, capturing images of the illuminated particles in successive frames. Typically the cameras used to record images in either a double frame or single frame mode. In the double frame mode, an image pair is recorded with a time interval of dt and an independent acquisition frequency. On the other hand, in the single frame mode, the camera continuously records images with a time interval of dt and an acquisition frequency of $1/dt$. In both modes, dt should be chosen to be smaller than the relevant flow time scales. To spatially calibrate the captured domain, a template with predefined markers is mapped onto a Cartesian grid. This calibration process provides spatial corrections of these tracing particles based on their corresponding physical positions. These corrected images are subject to post-processing, including the reduction of background noise and wall reflections. Afterwards, the images are divided into sub-domains, namely the interrogation windows. A sliding cross-correlation algorithm processes the light intensity signals of each interrogation window, yielding correlation peaks that indicate average particle displacement of that domain. Due to the known time interval between the two frames (i.e. the chosen dt), velocity vector corresponding to the obtained average displacement can be estimated. This process is repeated for all interrogation windows, resulting in a complete 2D velocity vector field within the laser-illuminated plane.

Stereo PIV Configuration

In contrast to planar PIV, stereo PIV resolves the third component (i.e. out-of-plane component) by employing an extra camera. In the context of swept wing boundary layers (i.e. three-dimensional), stereo PIV excels in measuring the velocity vectors in all streamwise, spanwise and wall-normal directions simultaneously. While the underlying principle of stereo PIV resembles that of planar PIV, there are notable distinctions in the experimental setup and image processing. In stereo PIV, the cameras are positioned at an angle relative to the laser sheet, resulting in non-uniform distances from the field of view to the camera across the image. Due to the resulting distance variations, the captured particles are out of focus in specific regions. To ensure the sharp focus throughout the entire image, a Scheimpflug mount is employed, which tilts the image plane to be aligned with the lens and object plane [44].

The stereo PIV arrangement in the current study consists of two cameras positioned on opposite sides of the laser sheet plane. Therefore, a double-sided calibration target is required, which features a precise grid of markers. Nonetheless, small camera vibrations or laser sheet shifts are likely to result in misalignment of laser sheet with the target axis [74], requiring a disparity correction or self-calibration. This self-calibration relies on the cross-correlation of the actual particle images, characterizing the displacement field representing the disparity between both camera views. The disparity field is subsequently employed to refine the initial mapping coefficients (originally computed from the calibration target), ensuring a more accurate and representative calibration [1].

2.4.4. MEASUREMENT UNCERTAINTY QUANTIFICATION

The uncertainty of experimental measurement data derives from two main sources, namely systematic errors and random errors. Specifically, systematic errors are usually constant and addressed through calibration procedures, while random errors remain unknown and unpredictable. Regarding HWA cases, random errors can be attributed to various factors, including probe disturbances, velocity calibration, signal interpretation in high-turbulence intensity regions and reversed flow ambiguity [17]. On the other hand, error sources of PIV could be attributed to misalignment and synchronization of the system, particle tracing capability, imaging of the particles, laser-light illumination, flow topology and image evaluation techniques [74].

To estimate the uncertainty statistics of measured velocity series, the methods of Sciacchitano & Wieneke [83] are employed. The uncertainty of mean value $\mathrm{U}_{\bar{u}}$ and standard deviation U_{σ_u} can be estimated as below:

$$\mathrm{U}_{\overline{u}} = \frac{\sigma_u}{\sqrt{N_s}}, \tag{2.9}$$

$$\mathrm{U}_{\sigma_u} = \frac{\sigma_u}{\sqrt{2(N_s - 1)}} \tag{2.10}$$

It should be noted that the determination of effective number N_s intricately depends on the sampling frequency of measurements. In cases of time-uncorrelated measurements, the effective number N_s can be directly set equal to the total number of samples N_t. This applies to the low-speed PIV measurements (in Chapter 5 & 6), which feature an acquiring frequency $f_s = 13\,\text{Hz}$. In contrast, for time-correlated samples, the determination of N_s relies on the integral time scale T_I as detailed in Smith *et al.* [90]. Specifically, the integral time scale T_I is derived from the autocorrelation of the measurement series and can be computed as $N_s = N_T/(2T_I/\Delta t)$, where Δt denotes the sampling interval. This applies to the HWA measurements in Chapter 4, which feature a high sampling frequency of 51.2 kHz. The corresponding uncertainties for HWA measurements are estimated as $\text{U}_{\overline{U}_{HW}} = 0.16\% U_\infty$ and $\text{U}_{\overline{\sigma}_{HW}} = 0.1\% U_\infty$.

2.5. BOUNDARY LAYER NUMERICAL SOLUTIONS

In this study, the velocity distributions within swept wing boundary layers are obtained at experimental flow conditions, through the simplified body force model. These velocity distributions are subsequently used for the LST calculations, serving as a guide for designing experiments, as well as a complementary for experimental measurements.

2.5.1. SIMPLIFIED BODY FORCE MODEL

During this study, the employed wing models consistently exhibit infinite swept wing conditions (i.e. spanwise-invariant flow) throughout experiment measurements. An illustrative example is given in figure 2.1(a), which displays the uniformity of spanwise pressure distributions. Consequently, the stability of swept wing boundary layers could be estimated by the steady and incompressible 2.5D boundary solutions (incorporating experimental pressure distributions). This laminar solution has been widely performed in prior research through an in-house numerical code, as illustrated by the work of Serpieri & Kotsonis [86] and Serpieri [84].

To account for PA effects in swept wing boundary layers, the body force generated by PA is added as a source term in the 2.5D laminar boundary layer equations, resulting in the so-called simplified body force model [87]. Several assumptions have to be made for this augmentation, as summarized by Yadala [97]: (1) The external flow has minimal influence on the executed body force distribution. This assumption holds true regarding tested *Re* in the current study, as demonstrated by the work of Pereira *et al.* [70]. This simplifies the characterization of body force, as it can be measured under quiescent conditions and subsequently incorporated into the simplified model; (2) The PA body force remains time-invariant or steady within the boundary layer. To ensure this assumption, PA is operated at particularly high frequencies, under which the applied forcing could be regarded as steady [30, 87]; (3) The wall-normal component of body force is assumed to be negligible. This assumption automatically holds true as the wall-normal component of the generated body force is significantly lower than the wall-parallel component (almost two orders smaller, [24]). Based on all these assumptions, the 2.5D boundary layer equations coupled with PA body force can be written as below:

$$\frac{\partial u}{\partial x} + \frac{\partial v}{\partial y} = 0, \tag{2.11a}$$

$$u\frac{\partial u}{\partial x} + v\frac{\partial u}{\partial y} = -\frac{1}{\rho}\frac{\partial p}{\partial x} + \nu\frac{\partial^2 u}{\partial y^2} + \frac{F_x}{\rho}, \tag{2.11b}$$

$$u\frac{\partial w}{\partial x} + v\frac{\partial w}{\partial y} = \nu\frac{\partial^2 w}{\partial y^2} \tag{2.11c}$$

where F_x is the x-component of the PA body force. Clearly, for conditions of PA-*off* and PA-*on*, the term F_x is set to zero and non-zero respectively. Due to the invariance of flow along the z direction, the z-momentum equation is decoupled from the others. These equations are solved using a Cartesian grid (by the boundary layer solver or the finite element multiphysics tool *Comsol*), which is stretched in a manner such that the x coordinate aligns with the wing's curvilinear abscissa.

2.5.2. LINEAR STABILITY THEORY (LST)

In realistic flight conditions (i.e. low turbulence intensity), the critical stationary CFI modes are eventually responsible for the laminar-turbulent transition, through the development of unsteady secondary instabilities [7]. Nevertheless, an operated PA will inherently introduce additional unsteady perturbations into the boundary layer, as introduced before. These can potentially trigger travelling CFIs, which can amplify significantly due to their relatively higher growth rate [7]. These considerations indicate that travelling CFIs potentially play a relevant role in the final breakdown when PA is operated. Therefore, predictions of both stationary and travelling CFIs are required as a first step in designing experiments.

LST has been traditionally used in studies of CFIs [42, 61, 84] as a tool to predict the onset of the primary CFI modes. It has been widely demonstrated that LST can correctly predict the spanwise wavelength λ, frequency f and propagation angle Ψ of CFI modes [22, 23, 42, 45]. However, it should be emphasized here, that LST fails to accurately estimate the later CFI evolutions due to its intrinsic limitations (e.g. does not account for non-parallel and non-linear effects as well as the disturbance receptivity, Serpieri (2018)). However, the outcomes of LST still give valuable qualitative information as a complimentary of experimental measurement.

For the stability problem, the parallel flow assumption is applied, assuming the base flow is independent on the y coordinates (i.e. V=0). The small perturbation ψ is assumed to be a wave-like solution [76], as shown in equation 2.12.

$$\psi(x,y,z,t) \;=\; \phi(y)\; e^{i(\alpha x+\beta z-\omega t)} \tag{2.12}$$

Specifically, the shape of the vertical perturbation is given by $\phi(y)$, the streamwise and spanwise wavenumber are given by α and β, and the angular frequency by ω. The velocity distributi ons obtained from the simplified model are then used to solve Orr-Sommerfeld equation, with various combinations of ω, α and β. In this study, three primary CFI modes are considered, namely the stationary CFI modes, positive travelling CFI modes and negative travelling CFI modes, which correspond to conditions of $\omega = 0$, $\omega > 0$ and $\omega < 0$ respectively. In the spatial formulation, the angular frequency ω is real. Whereas, the streamwise wavenumber α and spanwise wavenumbers β are complex, i.e $\alpha = \alpha_i + \alpha_r$ and $\beta = \beta_i + \beta_r$. Particularly, the imaginary parts of α_i and β_i determine the spatial growth. Nonetheless, the spanwise-invariant flow leads to $\beta_i = 0$. Finally, the integral amplification N factor is calculated by integrating the spatial growth rate $-\alpha_i$ along the streamwise x axis.

$$N(x, \lambda, \omega) = \int_{x_0}^{x_l} -\alpha_i(x, \lambda, \omega)dx \tag{2.13}$$

where x_0 is the neutral point of the target CFI mode and x_l is the end point of considered domain. A full routine and detailed term definitions can be found in the work of Mack [58].

3

Swept Wing Model $K-M3J$

This chapter illustrates the design procedure of the new swept wing model $K-M3J$, which reproduces the near-leading-edge pressure distributions of the reference model $M3J$. The process involves the two-dimensional wing shape design and CFD validation, as well as the three-dimensional CAD model design and fabrication. The performance of the $K-M3J$ model is validated by preliminary wind tunnel experiments, encompassing surface pressure measurement, IR thermography visualization and planar PIV boundary layer measurement. Furthermore, the 2.5D boundary layer solution based on experimental pressure distributions, coupled with the LST analysis, is applied to numerically evaluate the characteristics of CFI modes, complementing the experimental observations.

Peng, K. and Kotsonis, M., 2021. *Cross-flow instabilities under plasma actuation: Design, commissioning and preliminary results of a new experimental facility.* In AIAA Scitech 2021 Forum (p. 1194).

3.1. INTRODUCTION

While several research studies based on PAs have been successfully conducted on the $M3J$ model, it's worth noting that the model wasn't originally designed for PA applications. As an example, when operating the PA for extended periods, there's a risk of damaging PA electrodes due to the gradual degradation from overtime measurements. This degradation can potentially lead to the occurrence of arc discharges, characterized by large power and high temperature. This in turn, can easily damage the smooth surface of the model, which is a pivotal factor in conducting CFI studies. Furthermore, the large size of the $M3J$ model have introduced challenges in terms of manufacturing and installing of PAs on the model, as explained in section 2.3.1. Additionally, the closed and limited optical access of the LLT test section adds extra complexity to the measurement setup arrangement. Therefore, a new swept wing model named $K-M3J$ for plasma-based experiments is specifically designed and deployed in the A-tunnel at Delft University of Technology.

This Chapter presents a description of the design and fabrication of the $K-M3J$, followed by preliminary experimental results. First, the 2D wing geometry is derived from the modification of the reference wing model $M3J$. The aerodynamic performance of the new wing shape is validated by the CFD simulations. The results illustrate a good pressure matching of the $K-M3J$ with the target C_p from $M3J$. Additionally, no separation is observed at the pressure side of $K-M3J$. Subsequently, the 3D $K-M3J$ model is designed by CAD tool *Solidworks* and manufactured by CNC machining, specifically for plasma-based experiments. Finally, a preliminary characterization experiment was conducted in the A-tunnel, aiming at understanding the aerodynamic features of $K-M3J$ along with the PA performance. The pressure distributions are compared at several angles of attack α to match with the target C_p. The resulting pressure coefficients are then used as the input for boundary layer solutions and LST analysis to calculate the N factors of stationary and travelling CFI modes. Finally, IR thermography and PIV are used to visualize the CF vortices and to investigate the PA effects on CFIs. The ultimate experimental results validate the ability of the new wing model $K-M3J$ in terms of studying PA effects on the receptivity and initial growth of CFIs.

3.2. MODEL DESIGN

3.2.1. 2D WING SHAPE

The design of the new wing model, denoted as the $K-M3J$ model, is based on the reference swept wing model $M3J$, which has been discussed in detail in section 2.1.2. Considering that the development of CF component is mainly controlled by the favourable pressure gradient along the chord, the growth of CFIs could be reproduced if the new model's C_p resembles the one of the $M3J$. In addition, the effects of PA on the receptivity and near-leading-edge growth of CFIs on the $M3J$ model are of interest. Starting from this consideration, the pressure coefficient C_p of the $K-M3J$ is required to match the near-leading-edge one of the $M3J$ at $U_\infty = 25\,\mathrm{m/s}$, from the stagnation point until $x/c_x = 0.2$ (pressure side of $M3J$). To achieve this goal, a 2D wing shape is initially designed using the pressure inverse calculation of the

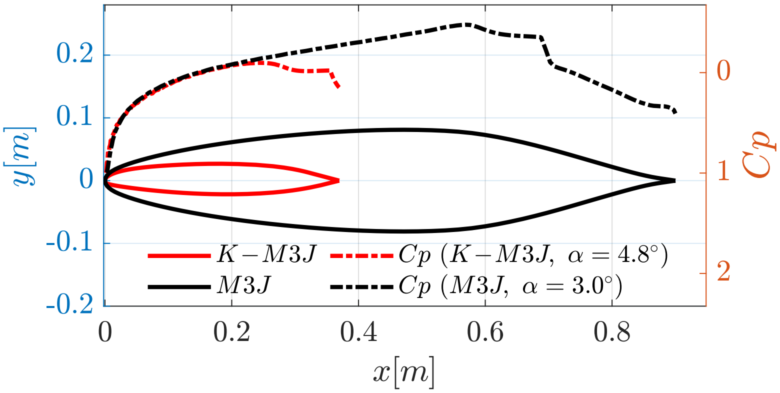

FIGURE 3.1: 2D geometry and pressure coefficient C_p (from the calculation of *Xfoil*) of $K-M3J$ and $M3J$.

XFLR5 tool[1]. In this design process, the near-leading-edge pressure distributions of the $M3J$ model serve as the prototype or reference. The resulting wing shape is further optimized by finely adjusting the pressure distributions in the viscous analysis of *Xfoil*[2]. The ultimate dimensional geometries of $K-M3J$ and $M3J$ are illustrated in figure 3.1.

Compared with the $M3J$, $K-M3J$ is much flatter and thinner in the shape, featuring an even smaller curvature radius at the leading edge. All these features support the formation of favourable pressure gradients as well as a delayed occurrence of the adverse pressure gradient [78]. On the other hand, in the current design, the 2D wing shape aligns with the xy plane and only the flow component u is considered in the calculation. Ultimately, at these conditions, a close matching of C_p between $K-M3J$ ($\alpha{=}4.8°$) and $M3J$ ($\alpha{=}3°$) is observed, as demonstrated in figure 3.1. It should be noted that these C_p are calculated by *Xfoil*, thus not considering the test section wall effect.

3.2.2. CFD SIMULATION AND CAD MODEL

In this section, the aerodynamic performance of $K-M3J$ is validated by CFD simulation. The widely used two-equation RANS $k-\epsilon$ turbulence model is solved by the commercial software *Comsol*. In the calculation of *Xfoil*, the windtunnel wall effect is not taken into consideration thus eliminating the blockage influence. However, in realistic test sections of wind tunnels, the blockage created by walls will accelerate the surrounding flow thus decreasing the pressure. To account for this effect, walls of the test section are added to the calculation domain, featuring a similar dimension with the A-tunnel test section (i.e. 700 mm × 400 mm, in Z and Y axes respectively), as shown in figure 3.5(a). In this CFD model, the calculation is only applied in the x direction (as shown in figure 3.4(b)) since the wing model is assumed to be infinite in the spanwise direction (i.e. z). As a result, the freestream velocity is given as

---

[1] `http://www.xflr5.tech/xflr5.htm`
[2] `https://web.mit.edu/drela/Public/web/xfoil/`

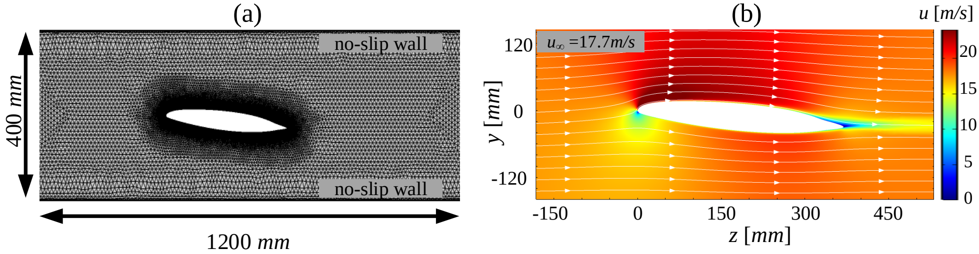

FIGURE 3.2: (a) Mesh and calculation domain of CFD model; (b) Average velocity field u of CFD model with selected streamlines (white arrows).

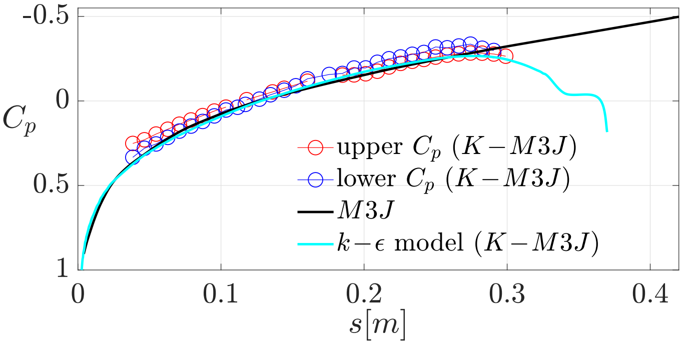

FIGURE 3.3: (Comparison of pressure coefficients between simulation and experiment. The black line refers to the target experimental C_p of $M3J$ and the light blue line indicates the numerical C_p from the $k\!-\!\epsilon$ model ($K\!-\!M3J$, $\alpha\!=\!4.75°$). Red and blue lines with circle markers indicate the experimental C_p from upper and lower pressure taps of $K\!-\!M3J$.

$u_\infty\!=\!17.7\,\text{m/s}$ and the wall condition is set as no-slip.

Figure 3.3 illustrates the C_p from the RANS $k\!-\!\epsilon$ model and the target one of $M3J$, where s indicates the surface distance starting from the leading edge (in the x direction). As presented in figure 3.3, a good agreement of C_p between $K\!-\!M3J$ ($\alpha\!=\!4.75°$) and the target $M3J$ ($\alpha\!=\!3°$) is achieved when considering the test section wall effect. It should be noted that the target C_p of the $M3J$ here results from the experiment measurements, at the condition of $U_\infty\!=\!25\,\text{m/s}$ and $\alpha = 3°$. The simulation outcome verifies that the deigned $K\!-\!M3J$ is still capable to reproduce the near-leading-edge pressure distributions of $M3J$ when considering the windtunnel wall effect, though with a slightly adjusted α. In addition, the minimal flow separation at the trailing edge indicates the sufficient laminar extension of the boundary layer as well as the boundary layer stabilization. The average-velocity field of u is shown in figure 3.2(b), where the white arrows illustrate the streamlines. As expected, at the condition of $u_\infty = 17.7\,\text{m/s}$ and $\alpha = 4.75°$, no separation is observed at the pressure side and only a small separation is detected on the suction side near the trailing edge, which guarantees an extensive laminar flow region on the pressure side. Based on the inspiring outcomes of the CFD simulation, the designed 2D shape of $K\!-\!M3J$ is taken as the prototype to design and manufacture the 3D swept wing CAD model.

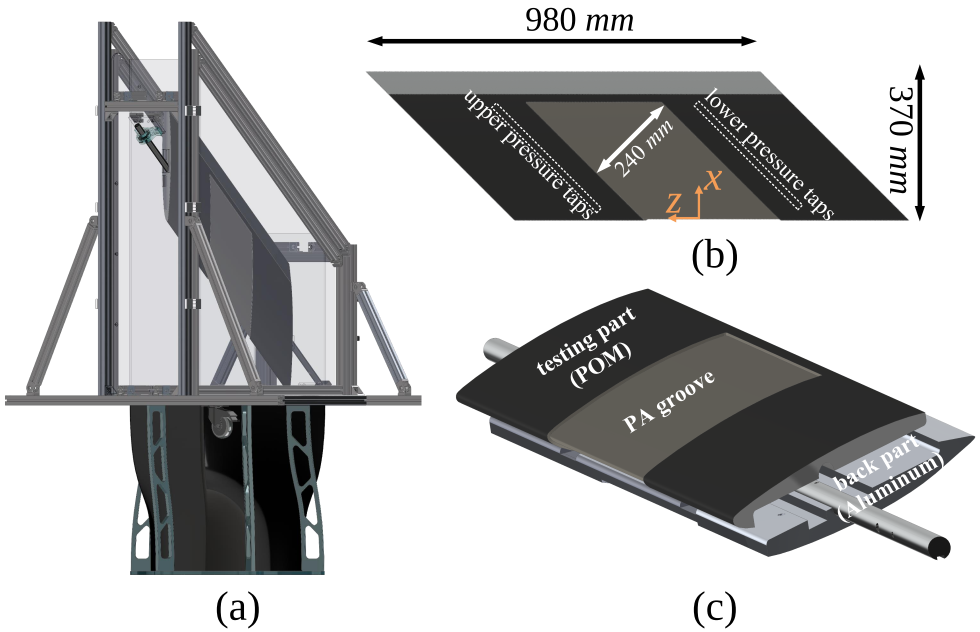

FIGURE 3.4: (a) CAD model of $K-M3J$ installed in the test section; (b) Top view of $K-M3J$ (pressure side); (c) Individual parts of the assembly CAD model.

The ultimate CAD model coupled with test section and contraction is shown in figure 3.4(a). The designed wing model features a sweep angle of 45° and a dimension of 980 mm × 370 mm in the xz plane, as illustrated in figure 3.4(b). Considering that this model is specifically designed for plasma-based experiments, it's essential to tackle several significant challenges: (1) PAs are fully electrical devices, which means that the material of the wing model should be non-metallic and insulated to prevent any potential electrical interference; (2) The wing model needs to be divided into 2 distinct parts due to the installation of pressure taps and the supporting shaft; (3) The possible bending deformation of plastic materials during the CNC fabrication. To address these issues, the $K-M3J$ model is designed as a composite of two individual pieces. The measuring part is made of Polyoxymethylene (POM) while the other part is constructed from aluminum. The two parts are securely joined together using screws, ensuring the model's shape and integrity. In addition, a broad groove with a depth of 3.1 mm is designed for the installation of PAs. The groove features a width of approximately 1/3 of the model's total spanwise length and extends to $x/c_x \approx 0.8$. In addition, two white dashed boxes in figure 3.4(b) illustrate positions of upper and lower pressure tap arrays. Specifically, the lower pressure tap array is the one located closer to the contraction inlet. Due to the manufacturing difficulties caused by the significantly small radius of the leading edge, the pressure tap array is not included in the vicinity of the leading edge. In other words, the pressure tap arrays extend from $x/c_x \approx 0.1$ to 0.8. In addition, the test section is closed by four walls made of transparent plastic materials (figure 3.4(a)). The outlet of the test section is tailored

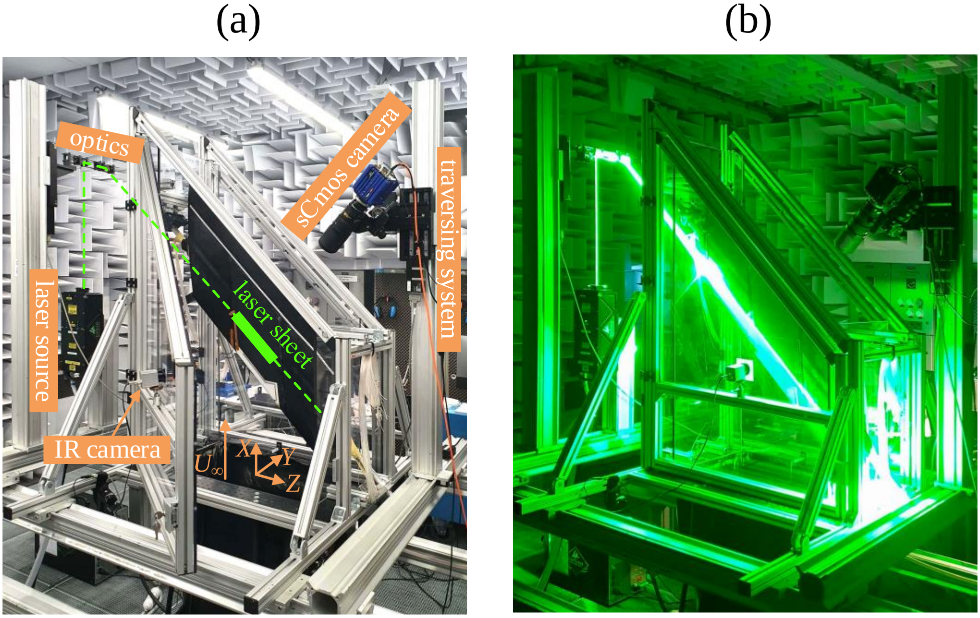

FIGURE 3.5: (a) Experimental setup for the preliminary experiments; (b) Experimental PIV setup with an operated laser .

Case	λ_{DRE}	x/c_x	D (mm)	h_{DRE} (mm)
DRE-L	8	0.02	1.772 ± 0.017	0.1147 ± 0.0023
DRE-H	6, 8, 10	0.02	1.772 ± 0.017	0.2179 ± 0.0031

TABLE 3.1: Geometric parameters and chord locations of DRE arrays

to follow the wing trailing edge for the convenience of installing subsequent measuring systems (e.g. the HWA measuring system).

3.3. PRELIMINARY EXPERIMENTAL INVESTIGATION

3.3.1. EXPERIMENTAL SETUP

The preliminary wind tunnel experiments are conducted in the A-tunnel to assess the validity of the designed $K-M3J$ model, encompassing surface pressure measurements, IR thermography visualization and planar PIV measurements. In order to avoid flow separation at the adverse pressure gradient region, zig-zag turbulators are used to trigger the turbulent boundary layers ($x/c_x \approx 0.8$ of pressure side and $x/c_x \approx 0.2$ of suction side). The groove designed for PAs is filled with a composite layer of PETG foils, on which the PA is placed. The typical spanwise-invariant PA is employed based on the BFM strategy and positioned at $x/c_x = 0.073$, parallel to the leading edge. Both encapsulated and exposed electrodes are fabricated with conductive silver paint with a dimension of 355 mm × 5 mm. The dielectric layer comprises PETG

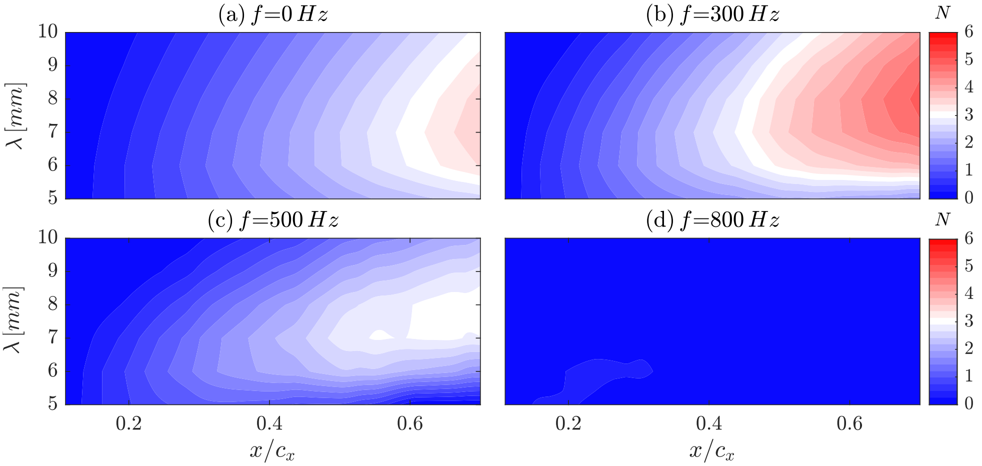

FIGURE 3.6: N factor from LST as a function of the wavelength λ and the streamwise chord location x/c_x for CFI modes of (a) 0 Hz; (b) 300 Hz; (c) 500 Hz; (d) 800 Hz.

foils of various thickness, resulting in a total thickness of 500 μm. To avoid any irregularity of the surface, the PETG foil as dielectric material is wrapped around the leading edge and extends to far downstream. Two DRE arrays are used to amplify stationary CFI modes and the parameters are summarized in table 3.1. Regarding the IR measurement, in order to improve the contrast between the low and high shear flow regions (i.e. the laminar and turbulent regions), two halogen lamps (500 W each) are used to irradiate the wing surface. The flow topology is visualized by the IR thermography, without a fine temperature calibration. The flow velocity fields are quantified by the planar PIV, for which the measuring plane is fixed at $x/c_x = 0.15$. Figure 3.5(a) illustrates the experimental setup and (b) shows the experimental picture of PIV setup with the working laser. The laser and camera are shifted together by a traversing system which enables maintaining their alignment and focus during scanning. Specifically, 1000 image pairs are acquired at the frequency of 13 Hz. As a result, the average uncertainty of w in the free stream is estimated as 0.017% U_∞ and the maximum uncertainty of w in the boundary layer is estimated as 0.1% U_∞.

3.3.2. PRESSURE DISTRIBUTION AND LST ANALYSIS

Due to the flow blockage and wake effects of current test section, the angle of attack α of the $K-M3J$ and freestream velocity U_∞ are slightly adjusted in order to match the target C_p of $M3J$. The ultimate results indicate that a significant matching of C_p could be achieved at the condition of $\alpha = 3.5°$ and $U_\infty = 22$ m/s, as illustrated in figure 3.3. It should be noted that, this match is achieved at conditions of $U_\infty = 25$ m/s for the $M3J$ and $U_\infty = 22$ m/s for the $K-M3J$, corresponding to the global Reynolds number $Re = 2.17 \times 10^6$ of $M3J$ and $Re = 7.72 \times 10^5$ of $K-M3J$ respectively (in the X direction). This result verifies the capability of the $K-M3J$ to replicate the near-leading-edge C_p of the $M3J$, enabling comparisons between the two models in terms of more comprehensive investigations into the receptivity and development of CFIs. In addition, the almost invariant C_p of lower and upper pressure taps demonstrate the spanwise uniformity of the $K\!-\!M3J$ thus the infinity swept wing boundary layer condition. Additional tuft visualizations (not shown here) reveal that only minimal separation occurs near the trailing edge, verifying the outcomes of the previous CFD simulation.

Along with the flow measurement results, the LST analysis is performed based on the experimental pressure distributions to estimate the boundary layer stabilities of $K\!-\!M3J$. Specifically, the average pressure distributions from the lower and upper pressure taps ($U_\infty = 22\,\mathrm{m/s}$) are employed in the boundary layer solver to estimate the velocity fields for the LST analysis. Through the process detailed in section 2.5.2, the N factors are calculated for CFI modes of various λ and f. Specifically, f varies from 0 Hz to 1000 Hz with a step of 100 Hz, whereas λ ranges from 5 mm to 10 mm with a step of 1 mm. The resulting N factors are illustrated only for several cases for brevity, as shown in figure 3.6. Specifically, figure 3.6(a) presents a comparison of stationary CFI modes (i.e. $f = 0\,\mathrm{Hz}$) with various wavelengths. Evidently, smaller wavelength modes exhibit more pronounced growth in the upstream region. Whereas the modes of 7 mm $\sim$ 8 mm take the dominance in the downstream region and could be regarded as the critical stationary CFI modes under the current experiment conditions. The critical stationary CFI modes agree well with those of the $M3J$ [86, 99], demonstrating the similarity of boundary layer characteristics between $K\!-\!M3J$ and $M3J$. As a result, 8 mm is chosen as the DRE spacing λ_{DRE} in subsequent preliminary experiments, aiming at exciting the critical stationary CFI modes predicted by LST.

Figure 3.6(b)-(d) further illustrate the N factors of travelling CFI modes of 8 mm, which obtain the largest values at $f = 300\,\mathrm{Hz}$. Specifically, travelling CFI modes are significantly amplified as f increases from 0 Hz to 300 Hz. Nonetheless, when f further increases to 500 Hz, the travelling CFI modes start to decrease significantly. In fact, once f exceeds 800 Hz, no substantial N factors could be observed for travelling CFI modes. As a result, it can be expected that travelling CFI modes of lower frequencies (around 300 Hz) are more unstable in the boundary layer, compared to the modes of higher frequencies. This observation agrees well with the results of Yadala *et al.* [99] and underscores the need for operating PAs at higher forcing frequency f_{AC} to prevent the introduction of low-frequency travelling CFI modes.

3.3.3. INFRARED THERMOGRAPHY MEASUREMENT

In this section, the IR camera is employed to visualize the spatial topology of primary stationary vortices. The baseline case (i.e. no DRE and PA-*off*) is monitored at the condition of $U_\infty = 22\,\mathrm{m/s}$ and $\alpha = 3.5°$. Nonetheless, neither stationary CF vortices nor laminar-turbulent transition are observed by the IR camera. This implies that a broad laminar flow regime extension is achieved along the pressure side of the $K\!-\!M3J$ at current conditions. In fact, even increasing U_∞ to higher values, the distinct jagged pattern usually associated with the laminar-turbulent transition is still not detected by the IR camera. This indicates that the transition occurs far downstream due to the mild favourable pressure gradient of $K\!-\!M3J$ and suggests that the stronger CF amplitude conditioning using DRE should be introduced. A low-

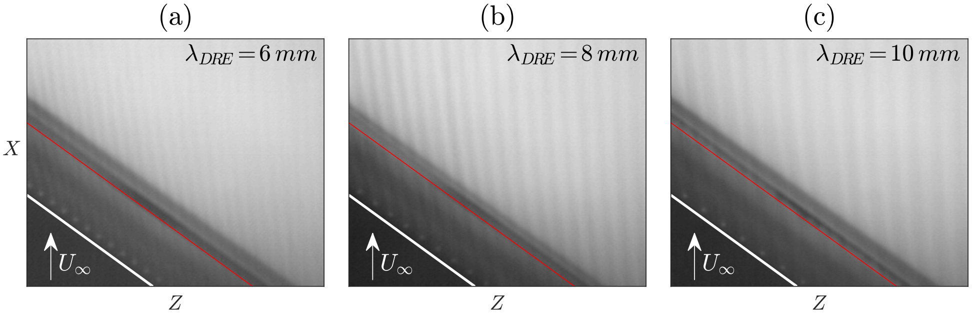

FIGURE 3.7: IR images of clean cases modulated by DREs of (a) $\lambda_{DRE} = 6$ mm; (b) $\lambda_{DRE} = 8$ mm; (c) $\lambda_{DRE} = 10$ mm. Leading edge is indicated by the white line and the PA intersection is indicated by the red line.

amplitude array DRE-L is tentatively installed near the leading edge ($x/c_x = 0.02$) to enhance stationary CFI modes. The DRE array used here features a spanwise spacing λ_{DRE} of 8 mm, corresponding to the critical stationary mode resulting from LST. In the clean case (i.e. with DRE and PA-*off*), however, still no distinct stationary CF vortex is observed except further downstream (not shown here). Recalling that such DRE used here has been working efficiently on the reference model $M3J$ [86], the observed weak vortices once again demonstrate that the boundary layer of $K-M3J$ essentially resembles the near-leading-edge boundary layer region of the $M3J$.

After removing the DRE-L, a high-amplitude array DRE-H is installed at the same location of $x/c_x = 0.02$. Specifically, DRE-H arrays of various spanwise spacings are investigated, namely $\lambda_{DRE} =$ 6 mm, 8 mm and 10 mm. The corresponding time-average IR images (clean cases) are shown in figure 3.7, with the flow coming from the bottom to the top. The white line refers to the leading edge and the red line indicates the PA intersection. It should be noted that the dark region near the bottom, which encompasses PA essentially represents the laminar flow. The lower temperature in this region is caused by the absence of black paint, leading to reduced heat absorption and emission, in comparison to the downstream areas. As shown in figure 3.7, the installation of DRE-H arrays result in the formation of uniform and prominent stationary vortices. This outcome coincides with the results from the pressure measurements, where relatively smooth pressure distribution and minimal flow separation near the trailing edge are confirmed. As an imitation of the $M3J$'s C_p near the leading edge, CFIs develop in a mild manner along the entire chord of $K-M3J$. Nonetheless, it appears that the DRE array of $\lambda_{DRE} = 8$ mm induces the most pronounced stationary vortices in the entire domain. Whereas, the DRE of $\lambda_{DRE} = 6$ mm produces more pronounced stationary vortices in the upstream region. This outcome coincides well with the previous LST results regarding the stationary CFI modes. Therefore, the validity of LST for predicting and designing the experiment aforehand is preliminarily confirmed.

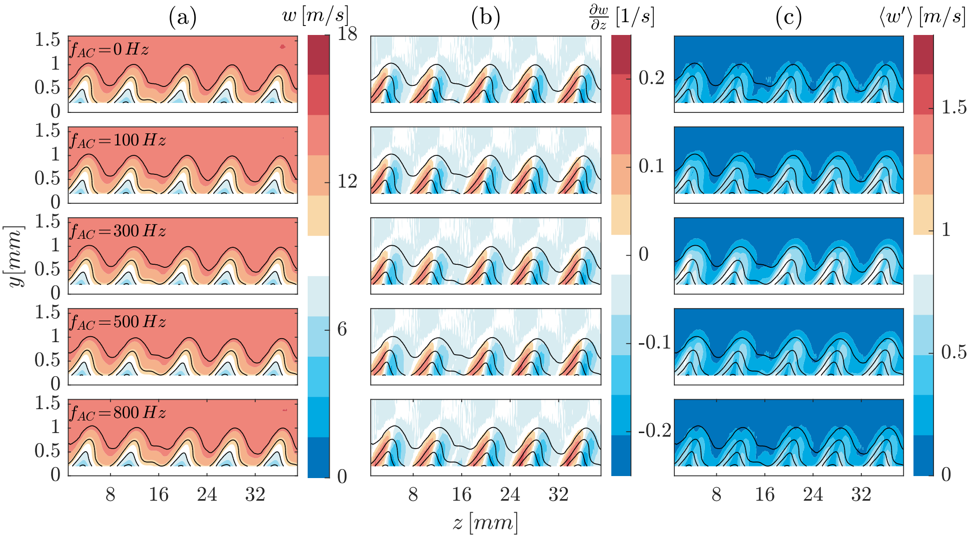

FIGURE 3.8: (a) Time-average spanwise velocity field w (looking from the upstream); (b) Spanwise gradient of time-average spanwise velocity $\partial w/\partial z$; (c) Velocity standard deviation $\langle w' \rangle$. The measurement plane is fixed at $x/c_x = 0.15$ and black iso-lines illustrate w (5 levels from 0 to 18 m/s).

3.3.4. PIV MEASUREMENT

In this section, the planar PIV measurement is implemented to give a quantitative view of the flow evolution as well as to validate conclusions of previous sections. The PIV measurements are carried out within the yz plane at $x/c_x = 0.15$. The flow is modulated by the DRE-H array utilized previously (i.e. $\lambda_{DRE} = 8$ mm). The supply power of PA is appropriately adjusted to avoid the initiation of turbulence and flow separation. Given the low turbulence intensity of A-tunnel ($T_u < 0.1\%$), the contamination of uncontrolled perturbations (e.g. ambient turbulence and wind tunnel noise) is critically eliminated. Therefore, the potentially observed unsteady velocity disturbances are assumed to be solely attributed to the PA operation.

Results of time-average spanwise velocity w, spanwise gradient $\partial w/\partial z$ and standard deviation $\langle w' \rangle$ at $x/c_x = 0.15$ are present in figure 3.8. Due to the laser light reflection and the high velocity uncertainty near the wall, velocity data in these regions ($y < 0.2$ mm) are deemed not sufficiently reliable and excluded from further analysis. According to the time-average velocity contours, five pronounced stationary vortices in total can be observed in the FOV, featuring a spanwise wavelength of 8 mm due to the DRE forcing. Moreover, these nearly equally-sized stationary vortices demonstrate the invariant spanwise conditioning, agreeing well with the pressure measurements. In addition, the stationary configurations (figure 3.8(a)) and spanwise gradient (figure 3.8(b)) of these stationary CF vortices remain nearly invariant in spite of various f_{AC}, indicating that plasma-induced perturbations are only weakly amplified, as expected. The velocity standard deviations are shown in figure 3.8(c), as a measure of the amplitudes of unsteady velocity fluctuations. Evidently, the amplitudes of unsteady fluctuations hold a function of f_{AC}. Within all tested f_{AC}, the velocity fluctuations are significantly enhanced when f_{AC} increases, while tend to decrease when f_{AC} further increases to 800 Hz. Specifically, the velocity fluctuations are most enhanced at $f_{AC} = 300$ Hz. In contrary, no significant alteration of velocity fluctuations is observed at $f_{AC} = 800$ Hz, though the fluctuation receptivity is supposed to be maximum due to the higher $f_{AC} = 800$ Hz. This result further coincides with the LST results thus validating the conclusions of previous sections.

3.4. CONCLUSION

In this chapter, the procedure to design a new swept wing model, namely the K–$M3J$ is presented in detail. Specifically, this model reproduces the near-leading-edge boundary layer development of the reference model $M3J$. First, a 2D wing shape is designed by using *Xfoil* based on the near-leading-edge Cp of the $M3J$. Subsequently the performance of the 2D wing shape is verified by the RANS $k-\epsilon$ turbulence model in *Comsol* where the test section wall effect is considered. The special design of the CAD model enables the $K-M3J$ to focus on plasma-based experiments. Consequently, the performance of the $K-M3J$ is verified by various measurement techniques including pressure measurement, IR thermography and planar PIV. The measured pressure coefficient C_p agrees well with the target $M3J$ and demonstrates the achievement of spanwise-invariant conditions at $U_\infty = 22$ m/s and $\alpha = 3.5°$. Based on the measured pressure distribution, the stability properties of the $K-M3J$ are predicted by LST. Consequently, DREs of various spanwise spacing are employed to trigger specific stationary CFI modes. According to the IR results, the DRE of $\lambda_{DRE} = 8$ mm appears to be the most effective thus demonstrating the LST predictions regarding the stationary CFI modes. Furthermore, the PIV results indicate that the low-frequency unsteady fluctuations are most amplified at $f_{AC} = 300$ Hz, in line with the LST predictions regarding travelling CFI modes. The preliminary experiment results validate the ability of the $K-M3J$ to study PA effects on the receptivity and near-leading-edge growth of CFIs.

4

UNSTEADY EFFECTS OF PLASMA IN SWEPT WING BOUNDARY LAYERS

This Chapter investigates the characteristics and development of plasma-induced unsteady fluctuations on the M3J model at $Re = 2.17 \times 10^6$*. Two important parameters of the PA operation are scrutinized, namely the forcing frequency and the streamwise location of PAs. DREs are installed near the leading edge to promote and condition a set of critical stationary CFI modes. Numerical solutions of the boundary layer equations and LST are used in combination to provide predictions of CFIs. The laminar-turbulent transition front is visualized and quantified by IR. Measurements of the velocity fields are performed using HWA scans at specific chordwise locations.*

Peng, K., Avallone, F. and Kotsonis, M., 2022. *Unsteady disturbances in a swept wing boundary layer due to plasma forcing.* Physics of Fluids, 34(11).

4.1. Introduction

While the use of PAs for swept wing transition control has been proposed in several variations, several challenges remain in their realistic implementations. One of the largely unknown factors influencing the PA efficacy is the introduction of non-deterministic PA disturbances, as detailed in section 1.3.4. These non-deterministic disturbances can be unavoidably amplified in the boundary layer, particularly when they coincide with the critical travelling CFIs. Therefore, the successful deployment of plasma-based LFC strategies for swept wing transition control, necessitates the elucidation of the origin and developing mechanisms of these unsteady disturbances.

This Chapter aims at the investigation of plasma-induced unsteady disturbances in a swept wing boundary layer dominated by stationary CF vortices, representative of typical cruise flight regimes. According to previous numerical studies of Wassermann & Kloker [94] and Bonfigli & Kloker [9], the frequency and the origin location of unsteady disturbances have pronounced effects on the boundary layer development. As such, two corresponding parameters of the PA forcing are investigated in this Chapter, namely the forcing frequency f_{AC} and the forcing location x/c_x. The choice of these parameters is directly related to the operation of PA and the stability characteristics of the boundary layer. The unsteady dynamics within the plasma discharge formation inherently depend on the applied forcing frequency f_{AC} [64]. On the other hand, the receptivity, the growth and topology of primary travelling CFIs and secondary CFIs are known to be highly dependent on the primary stationary CF vortex development, which in turn is related to the given streamwise location of their interactions [61].

It should be emphasized here that the current study is aimed at investigating the plasma-induced unsteady disturbances instead of delaying transition. As such, PAs are operated at significantly lower power and lower f_{AC} compared to previous studies reporting transition delay (Yadala *et al.* [99], $f_{AC} = 10\,\mathrm{kHz}$), thus minimizing the BFM effect and isolating the effects of unsteady instabilities.

4.2. Experimental Setup

In this Chapter, the experiment is conducted on $M3J$ in the LTT, under the condition of $U_\infty = 25.5\,\mathrm{m/s}$, corresponding to the $Re = 2.17 \times 10^6$. During the experiment, the $M3J$ model is placed at $\alpha = 3.3°$ and the pressure side is investigated. The pressure coefficient C_p is already shown in figure 2.1(a), demonstrating the spanwise-invariant condition of the swept wing boundary layer. The primary goal of this Chapter is to elucidate the effects of plasma-induced unsteady disturbances on a swept wing boundary layer dominated by stationary CFIs, in the framework of the BFM strategy. An essential requirement for such flow is the existence and development of stationary CF vortices, which serve as the target of the BFM technique. The critical stationary CFI mode (predicted by LST presented in section 4.3) is forced using a DRE array installed on the wing surface at $x/c_x = 0.02$. The characteristics of the DRE array are given in table 4.1. Additionally, the typical 2D spanwise-invariant DBD PA is utilised and configured based on the BFM principle. The widths of exposed and encapsulated electrodes are 5 mm and 10 mm respectively. To investigate the influence of the PA streamwise location, three spanwise-invariant actuators are printed and positioned at

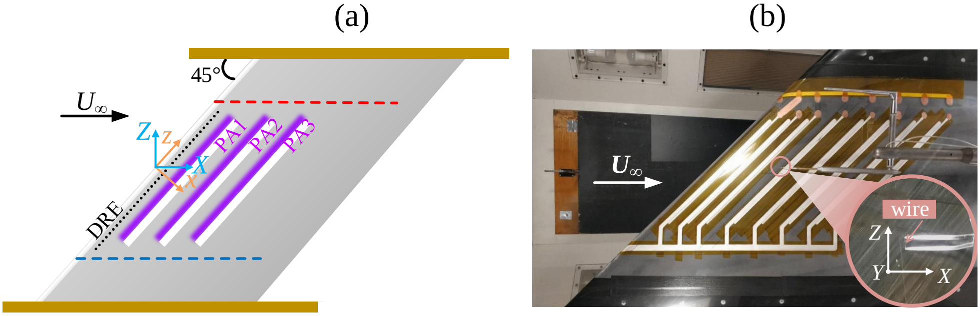

Figure 4.1: (a) Diagram of $M3J$ with PA arrays. Red and blue dashed lines illustrate locations of upper and lower pressure taps; (b) Experimental photograph of the HWA arrangement (note that more PA arrays are visible than used in the present work).

Case	λ_{DRE}	$\bar{\lambda}_{DRE}$	x/c_x	D (mm)	h_{DRE} (mm)
DRE	8	1	0.02	1.772 ± 0.017	0.1147 ± 0.0023

Table 4.1: Geometric parameters and chord locations of DRE arrays

locations of $x/c_x = 0.035$, 0.073 and 0.11 respectively, as shown in figure 4.1(a). A sheet of 500 μm thick PETG foil is used as the dielectric material. In order to form a smooth wing surface and avoid geometrical irregularities, the PETG foil is made large enough to wrap around the leading edge and extend downstream until the trailing edge. The three PAs are henceforth referred to as PA1, PA2 and PA3, respectively. A Trek 20/20C HS high-speed high-voltage amplifier is used as the power supply, delivering a sinusoidal high voltage signal at selected combinations of voltage $V_{p\text{–}p}$ and forcing frequency f_{AC}. During the experiment the three actuators are powered individually, with only one actuator active per time. An IR camera IR-full is mounted outside of the wind tunnel test section to investigate the laminar-turbulent transition. The IR camera acquires at a sampling frequency of 4 Hz and approximately 80 IR images are recorded per case, which are later averaged in order to minimise the background noise.

HWA is utilised to quantify the flow velocity and the arrangement is shown in figure 4.1(b). The hotwire is calibrated in-situ daily and appropriate corrections are applied for small changes in freestream temperature and barometric pressure during the experiment. The hotwire signal for each measurement point is recorded for a period of 2 s. Due to the deterministic operation of PAs, the induced flow disturbances are expected to be phase-conditioned to the forcing signal [87]. In order to perform phase-resolved analysis, the $V_{p\text{–}p}$ signals are acquired in synchronisation to the hotwire velocity signals. To monitor the developing boundary layer, the hotwire scans are conducted at two fixed chordwise locations, namely $x/c_x = 0.15$ and 0.2. Each scanning plane encompasses 30×32 points in y and z axes respectively and features a spanwise spacing resolution of $d_z = 0.5$ mm. The wall-normal spacing resolution is set as $d_y = 0.0667$ mm for $x/c_x = 0.15$ and $d_y = 0.0733$ mm for $x/c_x = 0.2$. Specifically, the velocity components are non-dimensionalized by the total freestream

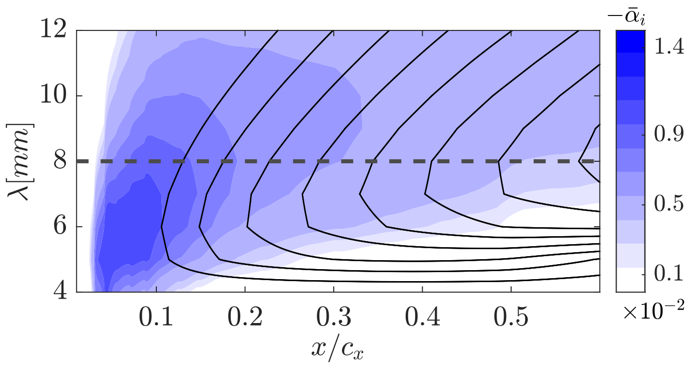

FIGURE 4.2: Non-dimensional amplification $-\bar{\alpha}_i$ and N factor diagram (black iso-lines) of stationary CFIs ($f=0$ Hz). The black dashed line indicates the wavelength λ of 8 mm. The N iso-lines increase from 1 (from left to right) with an interval of 1.

velocity $U_\infty = 25.5$ m/s with z non-dimensionalized as $\bar{z} = z/\lambda_{DRE}$. In addition, y is non-dimensionalized as $\bar{y} = y/\delta_0$ where δ_0 is the Blasius length scale as described in section 4.3.

4.3. PRELIMINARY LST ANALYSIS

In order to gain a preliminary prediction of the behaviours of stationary and travelling CFIs, the LST analysis is applied at the experimental conditions. Prior to the LST analysis, the mean flow fields of the baseline boundary layer are calculated based on the experimental pressure distributions of the windtunnel model (figure 2.1(a)). In this Chapter, the Blasius length scale $\delta_0 = \sqrt{\nu s_0/u_0} = 3.48 \times 10^{-4}$ m is used as the reference length. Specifically, ν is the kinematic viscosity, $s_0 = 0.138$ m is the surface distance from the attachment line to $x/c_x = 0.15$ and $u_0 = 16.65$ m/s is the edge velocity at $x/c_x = 0.15$.

Figure 4.2 shows the non-dimensional streamwise amplification $-\bar{\alpha}_i = -\alpha_i\delta_0$ and N factors of stationary CFI modes. In spite of the earlier growth of smaller wavelength modes, the mode of $\lambda = 8$ mm emerges as the most integrally amplified in the considered domain, in agreement with previous studies at similar conditions [87, 99]. Figure 4.3 illustrates N factors of travelling CFI modes of $f = 100$, 200 and 300 Hz. The result indicates that negative travelling CFI modes are significantly amplified within $f < 100$ Hz while positive travelling CFI modes are most amplified around $f = 200$ Hz. In fact, positive travelling CFI modes are completely suppressed once f surpasses 1000 Hz (not shown here). Compared with positive travelling CFI modes, negative modes are evidently weaker (more evident at higher frequencies) which agrees well with the observation of Guo & Kloker [40]. The apparent stabilisation of both directional modes at high frequencies indicates that PAs should be operated at high f_{AC} to avoid directly introducing travelling CFIs of low frequencies. Additionally, the current results indicate that low-frequency positive travelling modes are expected to play a more important role in the transition dynamics compared with their negative

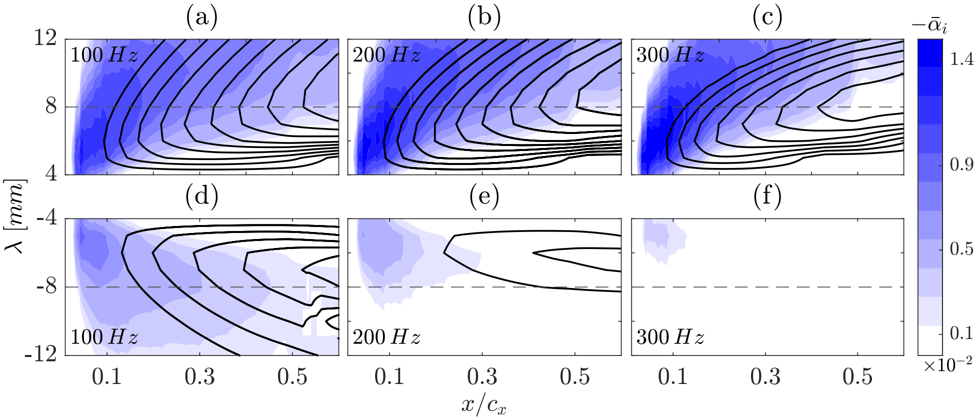

FIGURE 4.3: Same caption as figure 4.2 but for (a)-(c) positive travelling CFI modes and (d)-(f) negative travelling CFI modes. The black dashed line indicates the wavelength λ of ±8 mm.

counterparts due to their relatively higher amplification.

4.4. EFFECTS ON LAMINAR-TURBULENT TRANSITION

In this section, the effects of f_{AC} and PA location on the topology and location of laminar-turbulent transition are parametrically investigated by means of IR thermography. Due to the external radiation from the halogen lamps, the laminar flow region features a higher temperature than turbulent flow in IR images. The PA electrodes appear as dark strips of lower temperature due to their low emissivity.

The surface temperature topology for PA1 is visualized by the time-average IR field and illustrated in figure 4.4. Qualitatively similar topology is found for the other two PA cases (not shown here for brevity). In addition, to investigate PA effects on stationary CF vortices, a spatial Fast Fourier Transform (FFT) is applied on the time-average IR field in the spanwise direction. The spectral results are illustrated in plots next to the IR fields, corresponding to the region outlined by the magenta box. The abscissa of the spectra is x/c_x (from 0.12 to 0.16) and the ordinate is the non-dimensional wavenumber $\bar{\gamma}=1/\bar{\lambda}$, with a resolution $\Delta\bar{\gamma} = 0.0349$. The wavenumber $\bar{\gamma}=1$ corresponds to the critical stationary mode of $\lambda=8$ mm. In the PA-*off* case, the typical jagged transition front occurs around x/c_x=0.4, demonstrating the dominance of stationary CFIs in the boundary layer. As expected, an evident spectral peak is found at $\bar{\gamma}=1$, further confirming the conditioning of critical stationary vortices which result from the upstream DRE excitation.

The operation of PA1 exerts a significant alteration on the transition front. Compared with the PA-*off* case, the transition front evidently moves upstream and becomes spatially blurred, losing the distinct jagged pattern. This effect is more pronounced for low-frequency plasma excitation at $f_{AC}=200$, 300 and 500 Hz. The corresponding wavenumber spectra quantitatively demonstrate the topological observations as the $\bar{\gamma}=1$ signature is significantly weaker for these cases. The change in transition topol-

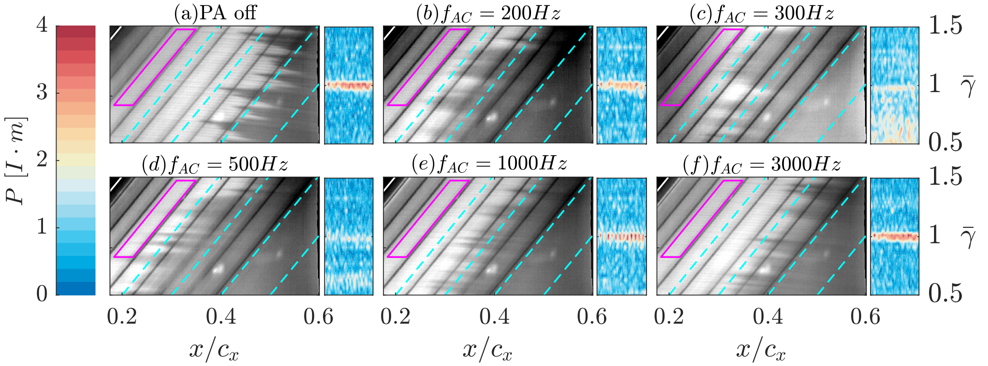

FIGURE 4.4: Time-average IR imaging, where PA1 works with $V_{p\text{–}p} = 10\,\text{kV}$ at (a) $f_{AC} = 0\,\text{Hz}$ (PA-*off*); (b) $f_{AC} = 200\,\text{Hz}$; (c) $f_{AC} = 300\,\text{Hz}$; (d) $f_{AC} = 500\,\text{Hz}$; (e) $f_{AC} = 1000\,\text{Hz}$; (f) $f_{AC} = 3000\,\text{Hz}$. The flow comes from left and the leading edge is shown by the white line in the upper-left corner. The wavenumber spectra correspond to IR domain outlined by magenta lines. Cyan dashed lines denote constant chord positions.

ogy offers a first indication of the transitional scenario alteration due to the enhanced travelling CFIs by PA, as these are known to decrease the spatial coherence of the transition front [87]. Compared with the low f_{AC} forcing, the high $f_{AC} = 3000\,\text{Hz}$ forcing appears to have a milder effect on the transition. At this condition, the transition front is located further downstream and is less blurred, indicating that travelling CFIs are less dominant (also demonstrated by the pronounced spectral peak at $\bar{\gamma} = 1$ in figure 4.4(f)). The current observation agrees well with the reported LST predictions, in which high-frequency travelling CFIs are found to be linearly stable in the present flow.

The transition shift $\Delta\,(x_t/c_x)$ (as mentioned in section 2.4.1) at $V_{p\text{–}p} = 10\,\text{kV}$ for various f_{AC} is summarised in figure 4.5. Overall, a negative transition shift $\Delta\,(x_t/c_x)$ is observed for all cases, indicating that transition moves upstream due to the PA operation. Furthermore, within the low-frequency range of $f_{AC} < 800\,\text{Hz}$, PA1 appears to have the most evident promoting effect on transition shift $\Delta(x_t/c_x)$, in comparison to PA2 and PA3. Considering PA1 is located closer to the leading edge, it can be expected that induced low-frequency disturbances will experience a longer chordwise amplification and result in stronger accumulated amplitudes compared with those in PA2 and PA3 cases [84]. However, by increasing f_{AC} to higher values, the transition shift $\Delta(x_t/c_x)$ of PA1 decays rapidly, indicating the limited enhancing effects of PA1 on high-frequency disturbances. In fact, the high f_{AC} operation is expected to impart more energy into the boundary layer, as the plasma-generated body force magnitude is increasing with f_{AC} [20]. Consequently, the plasma-induced velocity disturbances of high frequencies are expected to have larger initial amplitudes than in the case of low-frequency forcing. Still, the transition shift $\Delta(x_t/c_x)$ at the low f_{AC} operation surpasses that of high f_{AC} forcing, demonstrating that low-frequency unsteady disturbances are more dominant than high-frequency instabilities. On the other hand, significantly weaker effects on the transition shift $\Delta(x_t/c_x)$ are found

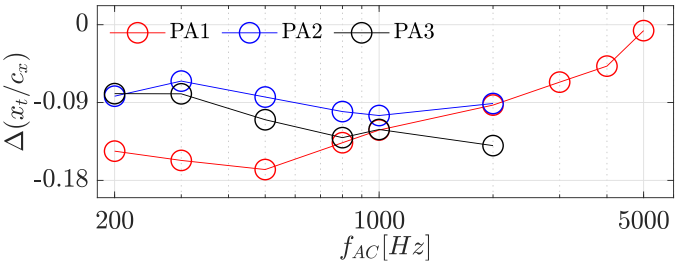

FIGURE 4.5: Transition shift $\Delta\ (x_t/c_x)$ at $V_{p\text{–}p} = 10\,\text{kV}$ for various f_{AC}. The abscissa follows a logarithmic scale and data points are plotted at f_{AC}=200, 300, 500, 800, 1000, 2000, 3000, 4000 and 5000 Hz.

for PA2 and PA3 when operated at low f_{AC}. Instead, the operation of the two downstream PAs has an increasingly strong effect on the transition location with increasing f_{AC}. The overall transition advancement reported in the present section, further highlights the potentially detrimental effects of plasma-induced unsteady disturbances when they feature frequencies as the critical travelling CFI modes (i.e. low-frequencies), within the context of the BFM method. Nonetheless, the effects of these plasma-induced unsteady instabilities still cannot be conclusively determined as they are also found to potentially delay the transition by weakening stationary CFIs through interactions [25, 40].

4.5. EFFECTS ON FLOW FLUCTUATIONS

In this section, a single hotwire probe is used to quantify flow velocities in the boundary layer. To avoid the dielectric layer and electrode degradation during the lengthy hotwire measurements, PAs are operated in a limited range of parameters, namely a single voltage amplitude of $V_{p\text{–}p}=8\,\text{kV}$ and frequencies of $f_{AC} = 200\,\text{Hz}$ and 3000 Hz. In order to assess the statistical properties of plasma-induced disturbances, Power Spectral Density (PSD), bandpass filtering and spanwise-wavenumber spectra of the hotwire measurements are discussed in the following sections.

4.5.1. SPECTRAL CHARACTERISTICS

As mentioned before, the inherent unsteadiness within the PA forcing is expected to induce unsteady disturbances in the boundary layer. Ultimately, the interaction between stationary and travelling CFIs as well as the secondary instability mechanism (associated with stationary CF vortices) can be affected, with repercussions on the final transition breakdown. Previous sections have shown that the underlying mean velocity gradient locations within the stationary CF vortex have a strong correlation with the developing types of CFIs [61, 94]. Specifically, the locations associated to type *I* mode and type *III* mode are shown by the region *A* and region *B* outlined in figure 4.6(a)). At similar conditions as in the present work, the type *I* mode features higher frequencies (in the order of kHz) while the type *III* mode develops at lower frequencies (in the order of Hz) [86]. It follows that the CFI types can be

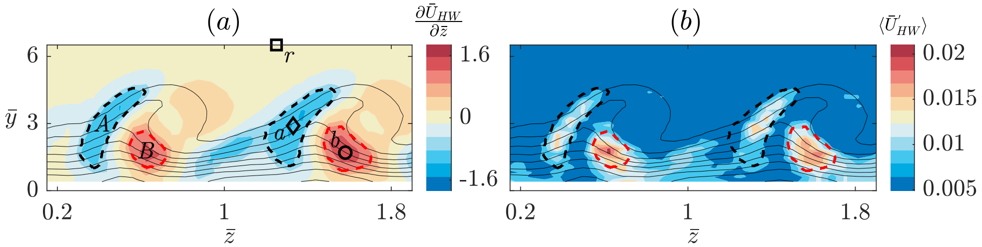

Figure 4.6: (a) Spanwise gradient of mean velocity $\partial \bar{U}_{HW}/\partial \bar{z}$ and (b) Non-dimensional velocity fluctuation amplitude $\langle \bar{U}'_{HW} \rangle$ for PA-*off* at $x/c_x = 0.2$. Location-a and location-b indicate the local peaks of velocity gradients. Location-r is used to monitor freestream conditions. Black and red dashed lines outline the minimum and maximum velocity spanwise gradient regions A and B respectively.

identified based on their corresponding dominant frequencies in combination with their localisations within the underlying stationary vortex structure. As such, a PSD analysis is applied on the hotwire signal (for frequency information) where two monitoring points are defined based on local extrema of spanwise velocity gradient $\partial \bar{U}_{HW}/\partial \bar{z}$, namely location-$a$ and location-b as shown in figure 4.6(a). The PSD amplitude of the velocity fluctuation U'_{HW} is calculated by the average periodogram method [96] and non-dimensionalized as $\bar{P} = (\frac{\Delta f}{U_\infty^2} PSD)^{\frac{1}{2}}$, where $\Delta f = 3.125$ Hz is the frequency resolution.

Figure 4.7 displays the non-dimensional spectra amplitude $\bar{P}$ at $x/c_x = 0.15$ under conditions of $f_{AC} = 200$ Hz and 3000 Hz. Additionally, the amplitude $\bar{P}$ corresponding to a location outside the boundary layer (location-r) is plotted as a reference, indicating the far-field and freestream conditions. Generally, for $f_{AC} = 200$ Hz, the reference signals demonstrate a negligible level of electro-magnetic interference. Several discrete peaks of random high frequencies are only found for PA3. In contrast, weak electro-magnetic interference from the PA operation is observed for reference signals in cases of $f_{AC} = 3000$ Hz. Nonetheless, these undesired noise sources are assumed to have negligible influence on the measurement due to their relatively lower amplitudes in comparison to plasma-induced velocity fluctuations. An additional feature of the PSD is the low-power broad hump centralised around $f = 10$ kHz, which is related to the inherent characteristics of the hotwire bridge, thus not corresponding to physical events [86].

As shown in figure 4.7(a) and (b), at both location-a and location-b, the PA forcing at $f_{AC} = 200$ Hz evidently amplifies velocity fluctuations compared with PA-*off*. Specifically, strong spectral peaks are found at $f = 200$ Hz and higher super-harmonics. At location-b, low-frequency velocity fluctuations ($f < 1000$ Hz) appear as more amplified than high-frequency components, especially for PA1 which is located most upstream. On the other hand, fluctuations within a broad range of high frequencies ($f > 1000$ Hz) are evidently amplified at location-a by PA3. In cases of forcing at $f_{AC} = 3000$ Hz as shown in figure 4.7(c) and (d), the amplitudes $\bar{P}$ at both monitoring locations under PA-*on* further confirm the unsteady nature of plasma forcing. As shown in PA1 case at $f_{AC} = 3000$ Hz (figure 4.7(d)), low-frequency fluctuations (which

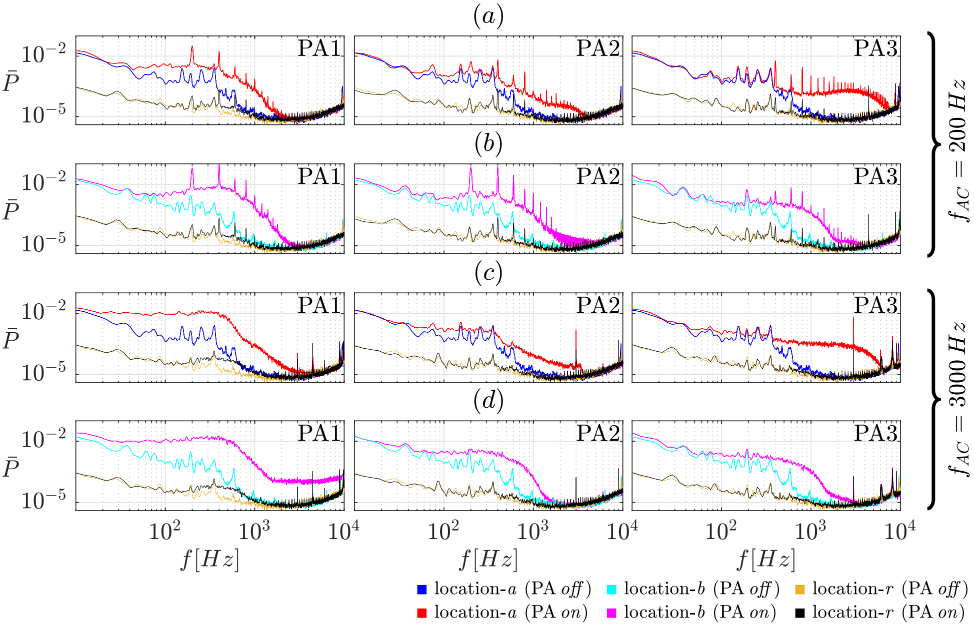

Figure 4.7: Non-dimensional spectra $\bar{P}$ of velocity fluctuations at $x/c_x = 0.15$ for (a) location-a, $f_{AC} = 200$ Hz; (b) location-b, $f_{AC} = 200$ Hz; (c) location-a, $f_{AC} = 3000$ Hz; (d) location-b, $f_{AC} = 3000$ Hz.

are locally unstable as predicted by LST) are still enhanced at location-b, despite the high-frequency plasma excitation. The triggering of these low-frequency fluctuations has been previously observed by Serpieri *et al.* [87] where PAs operated at high f_{AC} as well. One possible source of these low-frequency fluctuations could be attributed to the stochastic processes of the inherent micro-discharge in the plasma formation, as identified by Moralev *et al.* [64]. Moreover, this enhancing effect on low-frequency fluctuations (at location-b) shows a strong dependence on PA locations as it decreases from PA1 to PA3, which is similar to the trend observed at $f_{AC} = 200$ Hz. In contrast, high-frequency fluctuations are significantly amplified at location-a by the most downstream PA (i.e. PA3).

To identify the spatial localisation of the various spectral signatures observed, the time series of velocity fluctuations are bandpass-filtered using digital 4th-order Butterworth filters. These filters feature a selected center frequency f_B with a narrow pass-band width of 4 Hz. Representative frequency-filtered velocity fluctuations are illustrated in figure 4.8, corresponding to the $f_{AC} = 3000$ Hz case in figure 4.7. As expected, the unsteady fluctuations in PA-*off* cases have extremely low amplitudes and are significantly amplified at distinct frequencies by PA forcing depending on the PA location. Based on the frequencies and locations of these amplified fluctuations, two specific CFIs are recognised, namely the type I and type III modes. In combination with the PSD results, the low-frequency fluctuations ($200\,\text{Hz} < f < 800\,\text{Hz}$) centralized within region B are related to type III modes and the high-frequency fluctuations

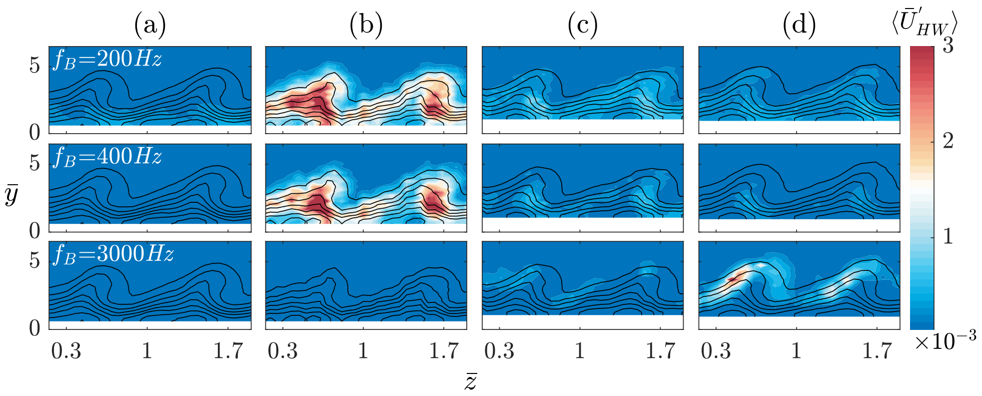

FIGURE 4.8: Bandpass filtered velocity fluctuation fields $\langle \bar{U}'_{HW} \rangle$ for (a) PA-*off*; (b) PA1; (c) PA2; (d) PA3. Measurements are carried out at $x/c_x = 0.15$, with PAs working at $f_{AC} = 3000$ Hz and $V_{p\text{-}p} = 8$ kV. The black iso-lines illustrate non-dimensional mean flow $\bar{U}_{HW}$ (20 levels from 0 to 0.85).

(2000 Hz $< f <$ 4000 Hz) centralized within region A are related to type I modes.

4.5.2. STREAMWISE AMPLIFICATION

The identified types of CFIs are quantified in the following manner. Two spatial masks are defined as regions for which the underlying spanwise velocity gradient $\partial \bar{U}_{HW}/\partial \bar{z}$ reaches a certain threshold. The mask for the PA-*off* case at $x/c_x = 0.2$ is given as an example in figure 4.6(a) with corresponding fluctuations in figure 4.6(b). Specifically, region A ($\partial \bar{U}_{HW}/\partial \bar{z} < -0.63$) is used to trace type I modes and region B ($\partial \bar{U}_{HW}/\partial \bar{z} >$ 0.94) for type III modes. While the absolute value of these thresholds is chosen heuristically, the thresholds are kept constant for the entire parameter range, ensuring comparable outcomes. It is important to emphasize that the thresholds selected are applicable solely to the present experimental conditions. As a matter of fact, these thresholds may be subject to the changes of Reynolds number, necessitating further investigation. According to the PSD results, the velocity fluctuations are strongly amplified at the forcing frequency f_{AC} and its harmonics. As such, fluctuations at selected frequencies are quantified by adapting the bandpass filter frequency, namely $f_B = 200,\ 400,\ 600$ and 800 Hz for the low-frequency type III modes and $f_B = 2000,\ 2400,\ 3000,\ 3600$ and 4000 Hz for the high-frequency type I modes. The non-dimensional amplitudes of frequency-filtered velocity fluctuations are spatially integrated in the mask regions following:

$$\bar{A}(f_B) = \frac{1}{s_t} \int\int_s \langle \bar{U}_{HW} \rangle ds \tag{4.1}$$

where s_t denotes the area of the corresponding region A or B. The non-dimensional amplitudes of velocity fluctuations at selected frequencies f_B are reported in figure 4.9. Specifically, integral amplitudes of type I and type III modes are distinguished by markers $\diamond$ and $\circ$ respectively. The PA-*off* case at $x/c_x = 0.2$ is chosen as a reference and shown in black color.

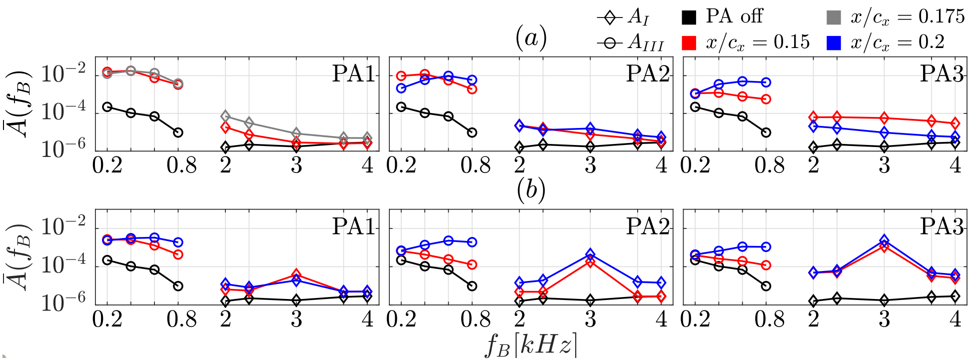

Figure 4.9: Spatially integrated amplitude $\bar{A}(f_B)$ for type *I* and type *III* modes where PAs work at (a) $f_{AC} = 200$ Hz; (b) $f_{AC} = 3000$ Hz. The data points are plotted at f_B=200, 400, 600, 800, 2000, 2400, 3000, 3600 and 4000 Hz.

Figure 4.9(a) illustrates cases of $f_{AC} = 200$ Hz for all PAs. Unfortunately, the case of $x/c_x = 0.2$ is not recorded for PA1 due to actuator malfunction during the experiment. Instead, a supplementary measurement of PA1 at $x/c_x = 0.175$ is used for the following discussion. The current results shed light on the effects of low forcing frequency $f_{AC} = 200$ Hz and PA location on the induced type *I* and type *III* modes. Inspecting the fluctuation amplitudes at $x/c_x = 0.15$, type *III* modes are found to be significantly amplified by PAs, compared with the reference. Moreover, the amplifying effect decreases from PA1 to PA3, agreeing well with the observed PSD. In contrast, type *I* modes are noticeably amplified by PA3 even though the forcing frequency is fixed at 200 Hz. This should be attributed to the fact that, secondary instabilities of type *I* are known to develop and amplify when the underlying stationary vortex has sufficiently modulated the boundary layer [96]. The PA3 is indeed located reasonably downstream, and as such, the present effect highlights the important role of PA location in inducing this type of disturbances.

As the flow develops downstream (i.e. $x/c_x = 0.2$), the type *III* modes generally amplify and reach comparable amplitudes for all tested PAs, despite their notably different amplitudes at $x/c_x = 0.15$. Moreover, it appears that, at $x/c_x = 0.2$, type *III* modes of higher harmonics are more amplified than those of primary forcing frequency. The origin of this effect is currently not clear, although the cascade of energy to higher harmonics might be indicative of non-linear interactions. The type *I* modes significantly amplified by PA3 at $x/c_x = 0.15$, rapidly decay at $x/c_x = 0.2$, for which the amplitudes remain as low as in cases of PA1 and PA2. The sudden attenuation contradicts the established behaviours of nominal type *I* instabilities which, in unforced flows, experience a fast growth and lead to transition rapidly once stationary CFIs reach amplitude saturation. Nevertheless, in the current experiment, the amplitude of stationary CF vortices at $x/c_x = 0.2$ (defined as the maximum spanwise standard deviation of mean flow $\langle \bar{U}_{HW} \rangle_z$) attains a value of 0.12 for PA3 (0.116 for the PA-*off* case). This is notably lower than the typical saturation amplitude (e.g. 0.21 by Serpieri & Kotsonis [86] and approximately 0.2 by Downs & White [34]). As such, the

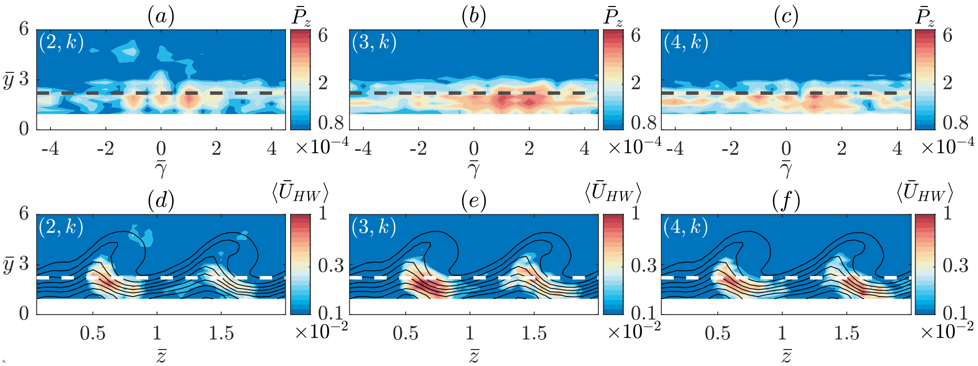

FIGURE 4.10: (a)-(c) Spanwise-wavenumber spectra $\bar{P}_z$; (d)-(f) Frequency-filtered fluctuation $\langle\bar{U}_{HW}\rangle$ for PA3 at $x/c_x = 0.2$ ($f_{AC} = 200$ Hz). Dashed line indicates the $\bar{y}$ location of the maximum $\langle\bar{U}_{HW}\rangle_z$.

unstable shear (which supports type *I* modes) appears not strong enough to sustain the growth of these high-frequency type *I* modes resulting in their eventual decay.

Figure 4.9(b) illustrates all PA cases for $f_{AC} = 3000$ Hz. Compared with PA-*off*, the low-frequency type *III* modes are evidently enhanced by the PA forcing despite the high f_{AC}. Specifically, these type *III* modes are most amplified by PA1. In contrast, an opposite tendency is observed for type *I* modes which are significantly amplified by PA3 while only limitedly enhanced by PA1 (more evident at $x/c_x = 0.2$). Different from the observation of $f_{AC} = 200$ Hz, the type *I* modes induced by PA3 remain at high amplitudes, contributing significantly to the growth of CFIs. For each case, while there is an overall increase in amplitudes of type *I* modes, the modes corresponding to the forcing frequency are particularly enhanced.

4.5.3. SPANWISE-WAVENUMBER SPECTRA

As indicated by the LST results, primary unsteady structures in the swept wing boundary layer are essentially comprised of positive and/or negative travelling CFIs from the perspective of modal decomposition. Within the presently used coordinate system, the positive and negative modes propagate outboard ($+z$) and inboard ($-z$) respectively in the yz plane (as shown in figure 1.8(a)). The LST results in section 4.3 predict that these travelling pairs feature different growth rates for a given frequency and spanwise wavelength combination. Therefore, one can expect the negative and positive travelling modes to play different roles in the instability development and ultimately the ensuing transition. In this section, spanwise-wavenumber spectra are calculated, aiming at investigating the physical features and spatial organisation of these travelling modes.

The deterministic conditioning of induced flow disturbances due to the PA unsteady forcing, enables the phase-resolved analysis of the hotwire time series. Capitalising on the synchronization between hotwire and PA voltage signals, the temporal velocity series are re-organised to align with a constant initial-phase with respect to the voltage signal. Consequently, the re-organised velocity sequences are subjected to a

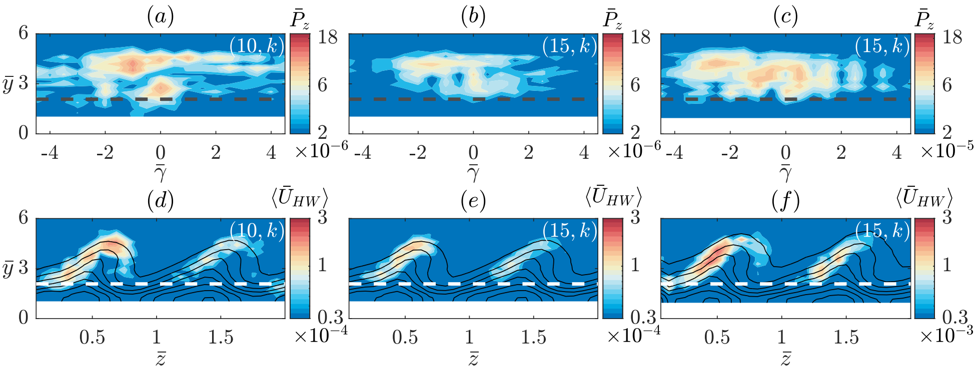

Figure 4.11: (a)-(c) Spanwise-wavenumber spectra $\bar{P}_z$; (d)-(f) Frequency-filtered fluctuation $\langle\bar{U}_{HW}\rangle$ for PA3 at $x/c_x = 0.15$. (c) & (f) are at $f_{AC} = 3000$ Hz while the rest are at $f_{AC} = 200$ Hz. Dashed line indicates the $\bar{y}$ location of the maximum $\langle\bar{U}_{HW}\rangle_z$.

two-dimensional FFT operation (in time and spanwise space z). The outcome provides a frequency-wavenumber spectrum at each y location [15]. In order to compare the travelling pairs, the amplitudes of the one-sided frequency-wavenumber spectra are extracted at desired frequencies (e.g. the forcing frequency and its harmonics). For consistency with established experimental and numerical studies, the double-spectral notation (h, k) is adopted to refer to generalised CFI modes featuring integer multiples of the reference frequency f_0 and spanwise wavenumber γ_0, namely $h = f/f_0$ where $f_0 = 200$ Hz and $k = \gamma/\gamma_0$ where $\gamma_0 = 1/\lambda_0$, $\lambda_0 = 8$ mm. Figure 4.10(a)-(c) illustrates representative spanwise-wavenumber spectra of low-frequency travelling modes for PA3 ($f_{AC} = 200$ Hz, $x/c_x = 0.2$), while figure 4.10(d)-(f) shows the corresponding velocity fluctuation fields $\langle\bar{U}_{HW}\rangle$. Similar outcomes are found in cases of PA1 and PA2 and not shown here for brevity. The spanwise-wavenumber spectral amplitude is non-dimensionalized as $\bar{P}_z = \frac{\Delta f \Delta\gamma}{U_\infty}P$, where $\Delta f = 0.5$ Hz and $\Delta\gamma = 62.5\,\mathrm{m}^{-1}$ are the frequency and wavenumber resolution respectively. The black dashed line represents the maximum spanwise standard deviation (mode shape) of the time-average velocity $\langle\bar{U}_{HW}\rangle_z$, indicating the approximate wall-normal location of the maximum amplitude of stationary CF vortices. As shown in figure 4.10(a)-(c), for low-frequency modes of $(2, k)$, $(3, k)$ and $(4, k)$, significant spectral amplitudes are found in the vicinity of the maximum $\langle\bar{U}_{HW}\rangle_z$, showing that the wall-normal distribution of travelling CFI modes strongly depends on the frequency, as observed by Casacuberta *et al.* [18]. Compared with the negative travelling modes $(h, -k)$, positive travelling modes $(h, +k)$ are evidently more amplified by the PA forcing. The dominance of positive travelling modes is also experimentally observed by Borodulin *et al.* [11, 14] and agrees well with previous LST predictions.

It must be noted here that the employed actuators are fabricated, installed and operated in a nominally spanwise-invariant manner. As such, the actuators are expected to locally induce 2D modes, i.e. $(h, 0)$. Notwithstanding, significant spectral amplitudes are found for travelling modes of $(h, \pm1)$ which feature a spanwise wavelength corresponding to the DRE spacing. The appearance of these modes

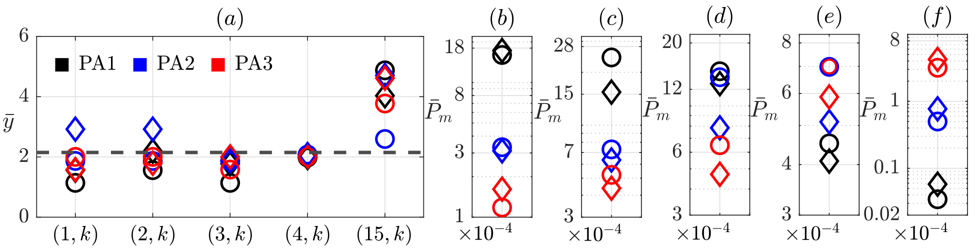

FIGURE 4.12: (a) Wall-normal location $\bar{y}_m$; (b)-(f) Spectral amplitude $\bar{P}_m$ for travelling modes at $x/c_x = 0.2$ (except PA1 at $x/c_x = 0.175$). (b)-(f) correspond to $(1, k)$, $(2, k)$, $(3, k)$, $(4, k)$ and $(15, k)$ modes respectively. The $(15, k)$ modes correspond to cases of $f_{AC} = 3000$ Hz and the rest to $f_{AC} = 200$ Hz. The marker ◇ denotes negative travelling modes while ○ denotes positive travelling modes.

can be attributed to the non-linear interaction between the DRE-induced stationary mode $(0, 1)$ and plasma-induced unsteady modes $(h, 0)$. As a consequence, these low-frequency travelling modes (where positive travelling modes play a dominant role) interact with the stationary mode $(0, 1)$ and result in type *III* modes, as confirmed by the corresponding $\langle \bar{U}_{HW} \rangle$ fields in figure 4.10(d)-(f). Figure 4.11 illustrates the spanwise-wavenumber spectra and velocity fluctuation $\langle \bar{U}_{HW} \rangle$ of high-frequency modes for PA3 ($x/c_x = 0.15$). It should be noted that figures 4.11(c) & (f) are at the condition of $f_{AC} = 3000$ Hz while the rest are at $f_{AC} = 200$ Hz. In contrast to low-frequency modes, considerable spectral amplitudes are found above the maximum $\langle \bar{U}_{HW} \rangle_z$ for high-frequency modes of $(10, k)$ and $(15, k)$. Moreover, in contrast to the trend found for low-frequency modes, negative travelling modes appear to be more amplified regarding the high-frequency modes.

To evaluate the PA effects on the negative and positive travelling modes, maximum spectral amplitudes and their corresponding wall-normal locations are quantified for cases at $x/c_x = 0.2$ (except PA1, which is measured at $x/c_x = 0.175$). For $f_{AC} = 200$ Hz, only low-frequency modes (i.e. $(1, k)$, $(2, k)$, $(3, k)$ & $(4, k)$) are considered since high-frequency modes feature negligible amplitudes at these conditions. In contrast, the high-frequency mode $(15, k)$ is extracted from cases of $f_{AC} = 3000$ Hz. The wall-normal location $\bar{y}_m$ and amplitude $\bar{P}_m$ where the negative and positive travelling modes attain a maximum are tracked within $-4 \le k \le -1$ and $+1 \le k \le +4$ respectively. The results are summarised in figure 4.12 where the marker ◇ denotes negative travelling modes while the marker ○ indicates positive travelling modes. The black dashed line in figure 4.12(a) indicates the average $\bar{y}$ location of maximum $\langle \bar{U}_{HW} \rangle_z$ for all cases at $x/c_x = 0.2$.

As shown in figure 4.12(a), the low-frequency modes are located lower and closer to the maximum $\langle \bar{U}_{HW} \rangle_z$ while the high-frequency modes are distributed above the maximum $\langle \bar{U}_{HW} \rangle_z$, confirming the association with type *III* and type *I* instabilities, respectively. Nonetheless, no clear trend in $\bar{y}_m$ is found when these modes are distinguished by their travelling directions. Figure 4.12(b)-(f) illustrates the amplitude $\bar{P}_m$ for the maximum positive and negative travelling modes. For cases at $f_{AC} = 200$ Hz, the positive travelling modes are generally more amplified than negative travelling modes for $(2,k)$, $(3,k)$ and $(4,k)$, though no clear trend is found for $(1,k)$. In contrast, negative travelling modes prevail among the high-frequency modes of $(15,k)$ for $f_{AC}=3000\,\mathrm{Hz}$, agreeing well with the previous observation.

4.6. CONCLUSION

4.6.1. EFFECTS OF PLASMA ACTUATOR LOCATION AND FREQUENCY

This Chapter experimentally inspects the effects of the PA forcing in a swept wing boundary layer. More specifically, forcing frequency f_{AC} and forcing location of PAs are investigated with respect to the laminar-turbulent transition and instability development. Critical stationary CF vortices are conditioned using DREs to reproduce a critical scenario corresponding to realistic flight conditions. In agreement with LST results, the quantified transition locations demonstrate that low-frequency plasma forcing acts towards significant promotion of transition, particularly in regard to the most upstream forcing location (PA1). In contrast, the influence of low-frequency forcing is considerably weakened at more downstream forcing locations (PA2 & PA3). Considering that the boundary layer is unstable to travelling instability modes at all PA locations, the upstream introduction of low-frequency disturbances provides longer streamwise distance for spatial development, thus resulting in higher instability amplitude and earlier transition. This outcome further confirms the previous observations of Yadala *et al.* [99] and Serpieri *et al.* [87]. Instead, although visibly altering the transition front topology, the PA forcing at high frequencies appears to have an overall weaker effect on transition location.

The velocity fluctuations are further quantitatively investigated by hotwire scans at $x/c_x=0.15$ and 0.2 respectively. Similar to previous experiments of Serpieri *et al.* [87] and Baranov *et al.* [4], considerable spectral energy appears at low frequencies even when forcing is applied at high $f_{AC}=3000\,\mathrm{Hz}$. This is attributed to the intrinsic unsteadiness in the discharge, similar to what was found in 2D boundary layers by Moralev *et al.* [64]. The power spectral density and narrow bandpass filtering demonstrate the efficacy of the upstream PA forcing to enhance low-frequency type *III* instabilities while the downstream PA forcing appears to amplify high-frequency type *I* instabilities.

The results highlight the strong dependence of plasma-induced CFIs on f_{AC} and PA locations. In a boundary layer dominated by stationary CF vortices, it can be concluded that low-frequency type *III* instabilities are playing a dominant role for all PA locations when forcing is performed at low $f_{AC}=200\,\mathrm{Hz}$. Though pronounced high-frequency type *I* instabilities are provoked by the downstream PAs, they consequently decay, possibly due to the insufficient strength of the flow shears produced by the still growing (i.e. not saturated) stationary CF vortices. In contrast, at high forcing frequency f_{AC} of 3000 Hz, the effect on high-frequency type *I* instabilities is evidently pronounced. Ultimately, the strong sensitivity of the emerging type of unsteady disturbances appears to strongly correlate with the local receptivity of the boundary layer. At more upstream locations, the boundary layer is locally receptive and unstable to primary travelling modes, while at more downstream locations, to high-frequency secondary modes.

4.6.2. A COMMENT ON BFM EFFICACY

Reconciling previous studies of Yadala *et al.* [99] and Serpieri *et al.* [87], as well as the current experiment, the stochastic plasma-induced disturbances at both low and high frequencies can potentially damage the PA effectiveness for transition delay, at least within the context of BFM. For instance, to achieve the BFM control, the PA generally requires high power input and needs to be positioned close to the leading edge in order to favourably manipulate the CF component. As a consequence, the low-frequency disturbances could be initiated with high amplitudes and at extremely upstream locations. At these regimes, the flow receptivity to type *III* instabilities is high and can favour the growth of low-frequency CFIs thus weakening the BFM performance. Similarly, if the actuator is placed more downstream, then it inevitably operates in a region of heightened receptivity to type *I* instabilities, which are shown to be triggered by both high and low frequency PA forcing.

As such, minimizing unwanted unsteady disturbances introduced by PAs emerges as a key point towards improving BFM efficacy. Such effort needs to take into consideration of the complete stability and receptivity characteristics of the flow. The PA used in the current experiment is essentially tailored to produce a spanwise-invariant body force distribution. Possible unsteadiness in the body force can give rise to the $(1, 0)$ mode as found in figure 4.10 and 4.11. Meanwhile, the stationary $(0, 1)$ mode is enhanced in the present boundary layer due to the DRE conditioning, and in a possible application by general surface roughness. As a consequence, non-linear interactions between these two dominant modes result in the significant growth of travelling modes $(1, \pm 1)$. Following relevant numerical works of Guo & Kloker [41] and Dörr & Kloker [30, 32], the $(1, \pm 1)$ modes are unstable travelling modes featuring significant amplification in CF dominated boundary layers. Therefore, the wing surface roughness (either discrete or random) appears as a second key factor in BFM control.

Finally, the outcomes from the spanwise-wavenumber spectra inspire an alternative plasma-based approach for the CFI control. As illustrated, the typical type *III* instabilities are essentially dominated by the positive travelling modes. Therefore, tailored PA operation can be envisioned where the phase of the supplied voltage signal is adjusted such to introduce negative travelling waves to directly compensate type *III* instabilities. However, such wave-cancellation technique needs sensors to detect the phase of travelling waves, which raises additional requirements for designing the control system for practical applications.

5

Experimental Validation of the BFM Principle

In this Chapter, the PA forcing effects on the base flow and developing CFIs are experimentally investigated on the $K-M3J$ model. A spanwise-invariant PA is configured near the leading edge according to the BFM strategy. The simplified body force model and LST analysis are used to infer the stability characteristics of the boundary layer subject to BFM. The base flow velocity is measured by stereo PIV at various PA operating conditions. Similarly, the developing CFIs, triggered through DREs, are quantified by planar PIV. The current results shed light into the underlying principles of BFM-based PA operation, in the context of laminar flow control.

Peng, K., Arkesteijn, J.P.W., Avallone, F. and Kotsonis, M., 2022. *Experimental base flow modification on a swept wing using plasma forcing.* Physics of Fluids, 34(10).

5.1. INTRODUCTION

As summarized in section 1.3.3, the working principle and efficacy of the plasma-based BFM strategy were mainly confirmed by a batch of numerical studies, though this technique was indeed experimentally demonstrated to delay transition [99]. The direct effect of an operating PA on the CF component of a swept wing boundary layer has yet to be characterised experimentally. More importantly, the relation between PA operating parameters and the eventual attenuation of CF component needs to be established, in order to fully elucidate the working principle of this method. Furthermore, low-frequency disturbances can possibly be induced by the PA forcing, as a result of the inherent micro-discharge formations of plasma [64]. As a consequence, travelling CFIs could be parasitically induced by the PA due to their relatively larger growth rate in respect to stationary CFIs. Therefore, a boundary layer manipulated by BFM-based PA is expected to be dominated by both stationary and travelling CFIs, which necessitates the elucidation of PA's effects on both types.

In this Chapter, a typical spanwise-invariant PA is installed on the $K-M3J$ model to achieve the BFM control. The effects of plasma-based BFM are specifically investigated in view of two main targets, namely the base flow and CFIs. The achieved CF reduction and the base flow direction are traced under various momentum coefficient c_μ, which in turn is controlled by the applied high voltage amplitude $V_{p\text{–}p}$. Moreover, the streamwise growth of CFIs is investigated under the constant PA action with various DREs.

5.2. EXPERIMENTAL SETUP AND METHODOLOGY

5.2.1. SWEPT WING MODEL AND WIND TUNNEL FACILITY

In this Chapter, the experiments are conducted in the A-tunnel which features a sufficiently low turbulence intensity ($T_u < 0.1\%$). The experimental flow conditions essentially resemble those of Chapter 3 (i.e. $\alpha = 3.5°$, $U_\infty = 22\,\mathrm{m/s}$ and $Re = 7.72 \times 10^5$). The used $K-M3J$ model is purposely designed to replicate the near-leading-edge pressure coefficient C_p of the frequently used reference $M3J$ model, as described in Chapter 3. The flow over the swept wing's pressure side is investigated and the corresponding experimental pressure coefficient C_p is already given in figure 3.1. Zig-zag turbulators are placed at $x/c_x = 0.8$ on the pressure side and $x/c_x = 0.2$ on the suction side to excite the turbulent boundary layer in order to avoid the flow separation at trailing edge.

For the base flow measurements (section 5.4), the velocity components are non-dimensionalized by the total freestream velocity U_∞, while for the CFI characterisation (section 5.5), velocity components are non-dimensionalized by the spanwise freestream velocity component w_∞. Additionally, y is non-dimensionalized as $\bar{y} = y/\delta_0$ where δ_0 is the Blasius length scale. $\delta_0 = \sqrt{\nu s_0/u_0} = 1.77 \times 10^{-4}\,\mathrm{m}$ is used as the reference length where $u_0 = 12.13\,\mathrm{m/s}$ is the boundary layer edge velocity at $x/c_x = 0.0594$. Specifically, ν is the kinematic viscosity while $s_0 = 0.0251\,\mathrm{m}$ is the surface distance from the leading edge to $x/c_x = 0.0594$.

Two PIV arrangements are used to quantify the flow fields, namely the stereoscopic PIV returning three velocity components $[u\ v\ w]$ for the base flow characterisation and

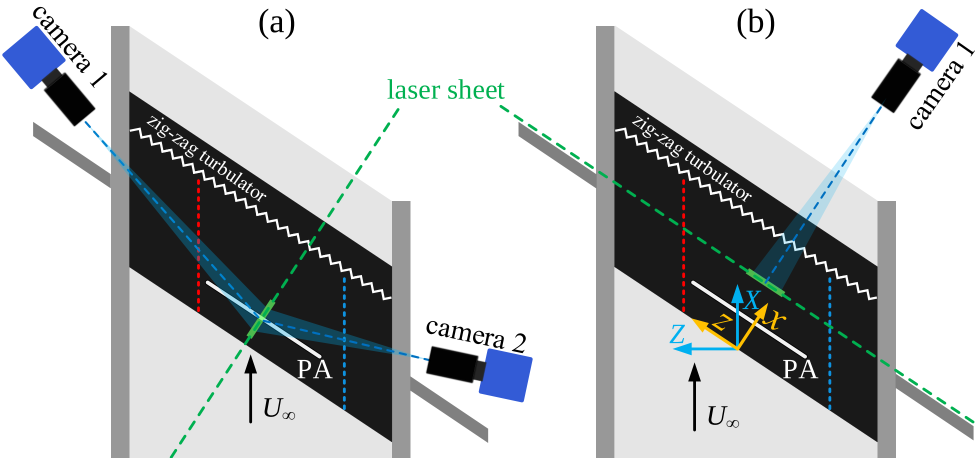

FIGURE 5.1: Schematics of (a) stereo PIV arrangement and (b) planar PIV arrangement used in this Chapter.

the planar PIV returning two velocity components $[v\ w]$ for the investigation of CFIs. In the stereo PIV arrangement, the flow field is measured with the laser sheet oriented in the xy plane (the z position of the measurement plane is fixed at the PA mid-span). Two LaVision Imager cameras (sCMOS, 2560 px × 2160 px) are placed on each side of the test section with a suitable stereoscopic aperture angle, acquiring at the sampling frequency of 13 Hz. A schematic of the stereo PIV setup is displayed in figure 5.1(a). The flow field is constructed as the ensemble average of 500 instantaneous stereo PIV vector fields. For the planar PIV arrangement, an automated traversing system shifts the laser and camera units together, thus maintaining their alignment. The schematic of the planar PIV setup is displayed in figure 5.1(b). The measurements are taken at several chordwise locations from x/c_x=0.125 to 0.3 with an interval of 0.025. Due to the minimal curvature of the wing model in this domain, the measurement planes are approximately normal to the local wall tangent at all locations. The data are acquired at the sampling frequency of 13 Hz. Time-average and standard deviation fields are extracted from 1000 instantaneous vector fields per case. Given the low temporal resolution (compared to the flow dynamics) of both PIV measurements, the time-average velocity and standard deviation fields acquired by both stereo PIV and planar PIV are uncorrelated.

It should be noted that, due to the laser light reflection and the high velocity uncertainty near the wall, velocity information in these regions is deemed not sufficiently reliable and discarded from further analysis. Namely data at $y < 0.1$ mm are not considered for the stereo PIV results while data at $y < 0.2$ mm are cropped for the planar PIV results. The time-average uncertainty [83] is calculated for both stereo PIV and planar PIV in the boundary layer and the freestream, respectively. For the stereo PIV, the maximum statistical uncertainty in the boundary layer is estimated as $0.24\%U_\infty$ for the u component and $0.87\%U_\infty$ for the w component. In the freestream, the average uncertainty is estimated as $0.017\%U_\infty$ for u and $0.047\%U_\infty$ for w. For

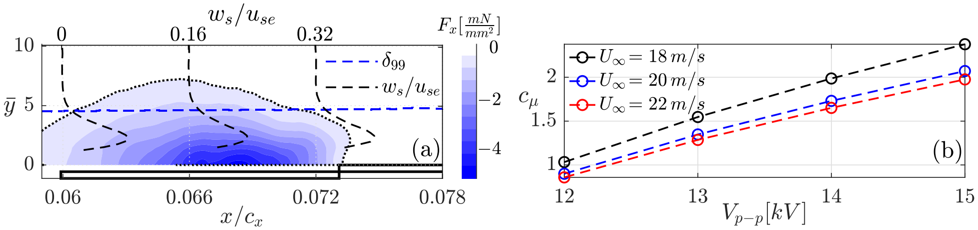

FIGURE 5.2: (a) Experimentally-measured body force distribution F_x at $V_{p\text{–}p} = 14$ kV. The dot line denotes $F_{x,10\%} = 10\%\, F_{x,max}$. Black dashed lines illustrate the spanwise-averaged profiles of w_s/u_{se} for the reference case at x/c_x=0.06, 0.066 and 0.072 (abscissa-shifted by 0.16). Blue dashed line refers to the unforced boundary layer thickness δ_{99}; (b) PA momentum coefficient c_μ corresponding to various input voltage amplitude $V_{p\text{–}p}$.

planar PIV, the maximum uncertainty for the w component is identified as $0.22\%U_\infty$ in the boundary layer while the average uncertainty in the freestream is $0.029\%U_\infty$.

5.2.2. PLASMA ACTUATOR AND DISCRETE ROUGHNESS ELEMENTS

A spanwise-invariant DBD PA is placed parallel to the leading edge with the interface between exposed and encapsulated electrodes located at x/c_x=0.073. The spanwise invariance of the actuator mitigates the possible introduction of unwanted spanwise modulation of the flow. A Trek 20/20C HS amplifier is chosen as the power supply for PA, through which the sinusoidal high voltage signal is generated and delivered to the actuator [87].

The flow field in the vicinity of an operating PA is acquired in a separate PIV experiment, which acquires at the sampling frequency of 20 kHz. Using the time-resolved method (section 2.3.2), the body force distribution of the used PA is calculated for various peak-to-peak voltage $V_{p\text{–}p}$, based on quiescent flow measurements enabled through planar PIV measurements. In addition, for the entirety of this Chapter, the PA is operated at a fixed carrier frequency $f_{AC} = 5$ kHz. The x-aligned body force component F_x in quiescent conditions is illustrated in figure 5.2(a) for $V_{p\text{–}p} = 14$ kV. To visually compare the spatial topology of the body force distribution with the characteristic scale of the experimentally-measured boundary layers, several CF component profiles w_s/u_{se} and the boundary layer thickness δ_{99} (where $u = 99\%u_\infty$, u_∞ is the local freestream component u at the boundary layer edge) are extracted from the stereo PIV measurements for the reference case ($U_\infty = 22$ m/s, PA-*off*). Specifically, u_{se} is the local streamline-aligned velocity at the boundary layer edge. As shown in figure 5.2(a), the employed body force extends almost throughout the boundary layer. Although at different forcing amplitude, the general topology appears similar to the most efficient forcing configuration found by Dörr & Kloker [29]. That is, the most effective PA forcing is attained when the volume force distribution covers almost the complete boundary layer but does not extend beyond the boundary layer edge. For various flow conditions pertaining to this study and PA operating

U_∞	18 m/s	20 m/s	22 m/s
$V_{p\text{–}p} = 12\,\text{kV}$	$c_\mu = 1.03$	$c_\mu = 0.9$	$c_\mu = 0.86$
$V_{p\text{–}p} = 15\,\text{kV}$	$c_\mu = 2.38$	$c_\mu = 2.07$	$c_\mu = 1.98$

TABLE 5.1: PA momentum coefficient c_μ at various $V_{p\text{–}p}$ and U_∞

Case	λ_{DRE}	$\bar{\lambda}_{DRE}$	x/c_x	D (mm)	h_{DRE} (mm)
DRE-*L*	8	1	0.02	1.772 ± 0.017	0.1147 ± 0.0023
DRE-*H*	8	1	0.02	1.772 ± 0.017	0.2179 ± 0.0031

TABLE 5.2: Geometric parameters and chord locations of DRE arrays

parameters, the actuation momentum coefficient is calculated as below [99]:

$$c_\mu = \frac{\int\int_s F_x ds}{\frac{1}{2}\rho u_e^2 \theta_u} \tag{5.1}$$

where u_e is the local edge velocity in the x axis direction (at x/c_x=0.073) and θ_u is the local boundary layer momentum thickness, based on u. The dependence of c_μ on $V_{p\text{–}p}$ and U_∞ is illustrated in figure 5.2(b). For the remainder of this Chapter, various momentum coefficients c_μ are used (table 5.1) and serve as a measure of the relative PA forcing strength.

As mentioned earlier, stationary CFIs dominate transition at realistic cruise flight conditions. To clarify the effect of the BFM strategy, the existence and development of stationary CFIs are required conditions for this experiment. In this study, DRE arrays featuring a spacing of $\lambda = 8$ mm are placed at $x/c_x = 0.02$ to promote critical stationary CF vortices (i.e. the most unstable mode according to the LST results, as described in section 5.3) of different amplitudes. In this Chapter, two distinct DRE arrays are used, namely the DRE-*L* and the DRE-*H*. The height and diameter of the used DRE arrays have been characterised using a precision laser profilometer and summarized in table 5.2. Due to the receptivity to different h_{DRE}, the DRE-*L* leads to a scenario where the flow exhibits a linear development while the nonlinearity is significantly affecting the flow in DRE-*H*.

5.3. ESTIMATION OF BFM EFFICACY

As discussed in previous sections, PA can potentially induce perturbations at non-deterministic frequencies, which in turn enhance the travelling CFIs and other types of boundary layer instabilities, even at low T_u conditions [100]. Nevertheless, since the BFM strategy is designed to directly reduce the CF component (i.e the driver of CFIs), both stationary and travelling CFIs are expected to be suppressed. To preliminarily assess the described effects, the simplified body force model is employed. The experimental pressure distribution and measured velocity profiles u and w at x/c_x=0.0551 ($U_\infty = 22\,\text{m/s}$) are used as top and inflow boundary conditions for this model, in which the time-invariant, incompressible Navier-Stokes equations are numerically solved, using the finite element multiphysics tool *Comsol*. The

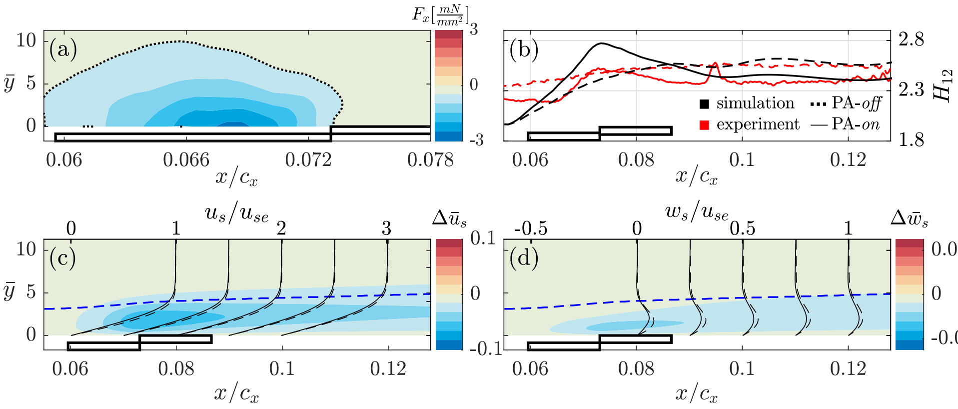

FIGURE 5.3: (a) Experimentally-determined body force; (b) Shape factor H_{12}; (c) Contours of streamline-aligned velocity reduction $\Delta\bar{u}_s$ due to plasma forcing; (d) Contours of CF velocity reduction $\Delta\bar{w}_s$. Blue dashed line in (c) and (d) indicates the boundary layer thickness δ_{99} (PA-*off*). Velocity profiles u_s/u_{se} and w_s/u_{se} are illustrated at x/c_x=0.08, 0.09, 0.1, 0.11 and 0.12, where corresponding u_s/u_{se} is abscissa-shifted by 0.5 and w_s/u_{se} by 0.25. PA operating at $c_\mu = 1.65$ and $U_\infty = 22\,\mathrm{m/s}$.

experimentally-determined body force ($c_\mu = 1.65$) is set as a steady source term in the NS momentum equations (as shown in figure 5.3(a)) and is adjusted to qualitatively match the experimentally-measured boundary layer velocity at PA-*on*. As shown in figure 5.3(b), the simulated shape factor H_{12} qualitatively matches the experimental case, especially for PA-*off*. The simulation also captures the abrupt increase of the shape factor due to the flow-opposing plasma forcing (i.e. local blockage) while no flow separation is observed, in either numerical or experimental fields. The streamline-aligned velocity u_s and CF velocity w_s are calculated and subtracted from the PA-*off* case (e.g. $\Delta\bar{u}_s = \bar{u}_{s,on} - \bar{u}_{s,off}$). The velocity profiles u_s/u_{se} and w_s/u_{se} are compared at several streamwise locations (x/c_x=0.08, 0.09, 0.1, 0.11 and 0.12) and displayed by dashed lines for PA-*off* and solid lines for PA-*on* respectively. Consistent with the results of Yadala *et al.* [99], u_s and w_s are found to be reduced by the BFM-based PA forcing, providing a first confirmation of the principle mechanism of BFM strategy.

To further assess the BFM effects on the boundary layer stability, the LST analysis is employed. Based on the numerically calculated boundary layer, the Orr-Sommerfeld equation is solved in spatial formulation with various combinations of angular frequency $\bar{\omega}$ ($= 2\pi f s_0/u_0$) and spanwise wavenumber $\bar{\beta}$ ($= 2\pi s_0/\lambda$). The non-dimensional growth rate -$\bar{\alpha}_i = -\alpha_i\delta_0$ and N factor are calculated for various frequencies and spanwise wavelengths, as shown in figure 5.4. The N factors are illustrated by the iso-lines where dashed lines refer to PA-*off*. The change in growth rate is calculated as $\Delta\bar{\alpha}_i = -\bar{\alpha}_{i,on} - (-\bar{\alpha}_{i,off})$ and indicated by the coloured contours. As shown in the PA-*off* case in figure 5.4(a), the stationary CFI modes appear to be most integrally amplified at a wavelength of approximately $\lambda = 8\,\mathrm{mm}$ in the domain of interest. This agrees well with the results of Chapter 3 at similar flow conditions. Within the concerned domain and for the entirety of this Chapter, the mode of

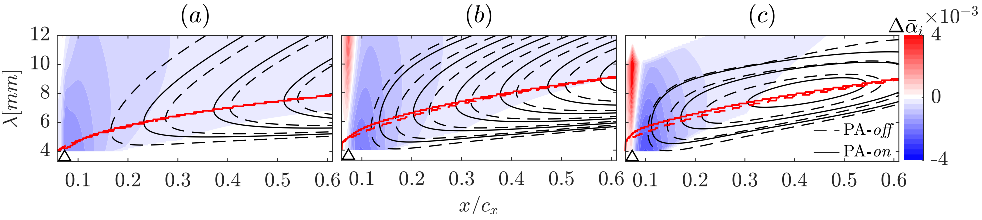

FIGURE 5.4: Change in amplification rate $\Delta\bar{\alpha}_i$ (coloured) and N factor (iso-lines) due to the plasma forcing at c_μ=1.65 for (a) Stationary CFI modes; (b) Travelling CFI modes at $f=200$ Hz; (c) Travelling CFIs at $f=400$ Hz. The N iso-lines increase from 1 with an interval of 0.5. Additionally, the dashed iso-lines refer to PA-*off* and solid iso-lines refer to PA-*on*. The triangle indicates the PA location while red lines indicate λ of the mode attaining the locally maximum N factor.

$\lambda=8$ mm is selected as the critical stationary mode. Regarding the travelling CFI modes, the N factor attains a maximum for modes at approximately $f=200$ Hz and rapidly decreases when f further increases.

As expected, the reduced CF component due to the PA forcing results in reduced growth rate for both stationary and travelling CFI modes. However, compared with stationary CFI modes, the stabilizing effect appears to be more evident on travelling CFI modes. This effect is consistent with the observations of Dörr & Kloker [29], which were attributed to the larger influence of 2D mean flow deformation on travelling CFI modes. Furthermore, the BFM effect is more evident for modes of smaller λ as a significant reduction is observed in both stationary and travelling CFI modes especially in the upstream portion of the considered domain. Additionally, the maximum N factor is traced in the streamwise direction and the corresponding λ is illustrated by the red lines (dashed lines refer to PA-*off*). The result evidently demonstrates that the forcing exerts a selective effect on the λ of the most amplified modes. Specifically, the travelling modes appear as more susceptible to this effect as λ of the most amplified mode noticeably becomes larger.

5.4. EFFECTS ON BASE FLOW

In this section, the attained base flow modification by the PA action is described, followed by an evaluation of amplitudes of streamline-aligned flow components (i.e. u_s and w_s) and the direction of the base flow. The flow field is constructed as a time-average ensemble of the stereo PIV vector fields, through which the three-dimensional velocity vector $[u\ v\ w]$ is recorded. The PIV results are shown in the body-fitted xy plane. It must be emphasised that the base flow experiment and following analysis in this section are performed on a clean wing, namely without DRE. This was chosen to ensure a largely spanwise invariant development of the boundary layer, which is essentially to avoid any stationary or travelling CF vortices due to the low residual roughness on the surface as well as minimal freestream turbulence in the wind tunnel. The velocity components u and w are later used to calculate the streamline-aligned velocity u_s and the corresponding CF component w_s. The velocity transformation from the wing-attached reference system to the streamline reference system is applied

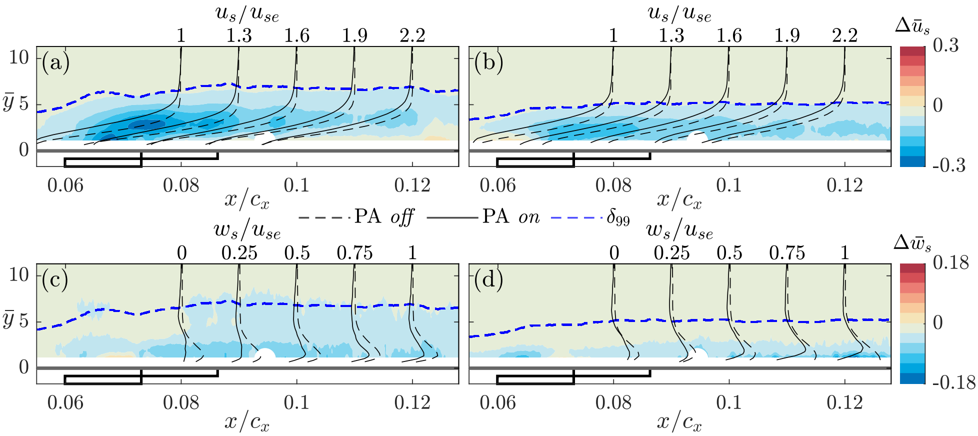

FIGURE 5.5: Velocity reduction $\Delta\bar{u}_s$ for (a) c_μ=2.38 and (b) c_μ=1.98; Velocity reduction $\Delta\bar{w}_s$ for (c) c_μ=2.38 and (d) c_μ=1.98. Blue dashed line indicates the boundary layer thickness δ_{99} for PA-*on*. Velocity profiles of u_s/u_{se} and w_s/u_{se} are shown at x/c=0.08, 0.09, 0.1, 0.11 and 0.12. The velocity profiles u_s/u_{se} are abscissa-shifted by 0.3 and w_s/u_{se} by 0.25.

as below [60]:

$$\begin{pmatrix} u_s \\ w_s \end{pmatrix} = \begin{pmatrix} \cos\,\phi_s(x) & \sin\,\phi_s(x) \\ \cos\,\phi_s(x) & -\sin\,\phi_s(x) \end{pmatrix} \begin{pmatrix} u \\ w \end{pmatrix}$$

where $\phi_s(x)$ is the local angle between the inviscid external streamline and x axis and defined as $\phi_s(x) = \tan^{-1}(w_\infty(x)/u_\infty(x))$ where $u_\infty(x)$ and $w_\infty(x)$ are the local freestream velocity components (in the direction of x and z respectively).

Figure 5.5 illustrates two representative cases ($c_\mu = 2.38$ and $c_\mu = 1.98$) where the relative changes of velocities $\Delta\bar{u}_s = u_{s,on} - u_{s,off}$ and $\Delta\bar{w}_s = w_{s,on} - w_{s,off}$ are calculated. The velocity profiles u_s/u_{se} and w_s/u_{se} are compared at chordwise locations from x/c_x=0.08 to 0.12 with a step of 0.01. The data in the white circle around $x/c_x = 0.094$ are discarded due to the laser light reflection. Nevertheless, the present results demonstrate that the PA effect on the base flow is mainly limited inside the boundary layer. As shown in figure 5.5(a), u_s is significantly reduced by the PA action for both low and high c_μ cases. A region of decelerated flow is found above the grounded electrode where the body force is typically centralised (i.e. the region of plasma discharge, figure 5.2(a)). The decelerating effect also imposes a direct influence on the boundary layer thickness δ_{99}, which is locally increased. On the other hand, the velocity profiles of u_s/u_{se} become less full under the PA forcing, indicating that du_s/dy (a measure of the skin friction coefficient) is reduced in the vicinity of PA. This result, however, is not contradictory to the observation of Dörr & Kloker [29] where u_s and skin friction are found amplified since the corresponding PA forcing is applied in z and z_s direction. In addition, the velocity reduction effect shows a strong dependence on c_μ as the PA loses control authority on the boundary layer when c_μ is reduced (comparing figure 5.5 (a) and (c)), in agreement with Yadala *et al.* [99, 100].

A similar trend is found for w_s (figure 5.5(b) and (d)), where the CF component

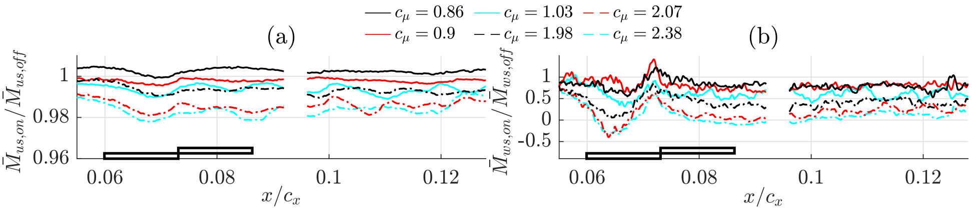

FIGURE 5.6: Momentum integral modification due to the PA forcing of (a) $\bar{M}_{us,on}/\bar{M}_{us,off}$ and (b) $\bar{M}_{ws,on}/\bar{M}_{ws,off}$.

w_s experiences a notable reduction due to the PA forcing. The evident decrease of the maximum CF component, which develops in the vicinity of the centralised body force, agrees well with the numerical predictions of Dörr & Kloker [29]. On the other hand, the present results illustrate that the PA imparts momentum along both x_s and z_s direction, as expected from the working mechanism of the BFM method. Nonetheless, the larger reduction values found of u_s demonstrate that the PA imparts more momentum against u_s, in the present case. This highlights the important role of BFM forcing orientation with respect to the local CF component. Considering the inviscid streamline inclination, for a 2D straight actuator, moving the actuator close to the attachment line can maximize the BFM effects. However, moving the PA close to the attachment line should take the PA strength (i.e. c_μ) into consideration to avoid possible boundary layer separation.

To further quantify the PA influence on the base flow, non-dimensional momentum integrals along y, namely $\bar{M}_{us}$ and $\bar{M}_{ws}$ (based on u_s and w_s) are calculated at each chord location x/c_x following equation 5.2.

$$\bar{M}_{us} = \frac{1}{\delta_{99}} \int_0^{\delta_{99}} |\rho \bar{u}_s| \bar{u}_s dy \tag{5.2a}$$

$$\bar{M}_{ws} = \frac{1}{\delta_{99}} \int_0^{\delta_{99}} |\rho \bar{w}_s| \bar{w}_s dy \tag{5.2b}$$

where ρ is the constant flow density. The ratio $\bar{M}_{on}/\bar{M}_{off}$ is calculated as a measure of the boundary layer momentum change due to the PA forcing. The momentum integral change $\bar{M}_{on}/\bar{M}_{off}$ at various c_μ is displayed in figure 5.6. The outcomes demonstrate a general momentum loss in u_s within the boundary layer. The PA ability in reducing $\bar{M}_{us}$ appears as a strong function of c_μ where the larger c_μ benefits the PA authority on the base flow modification. In the cases of higher c_μ, the $\bar{M}_{us}$ undergoes an evident decrease above the ground electrode where the body force is localised. Moreover, the decrease of $\bar{M}_{us}$ appears to remain downstream in the measuring domain. Nonetheless, the streamline-aligned component u_s of the boundary layer is comprised of the majority of flow momentum. As such, the relative PA effects on the u_s momentum are minimal as the maximum decrease of the ratio $\bar{M}_{us,on}/\bar{M}_{us,off}$ is only around 2%. In contrast, a significant effect of the PA forcing is observed on the considerably weaker CF component w_s. A significant reduction of $\bar{M}_{ws,on}/\bar{M}_{ws,off}$ is found above the encapsulated electrode, indicating the strong local

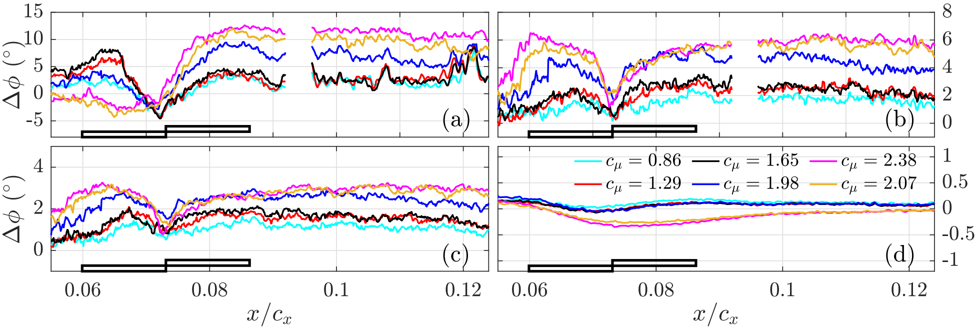

FIGURE 5.7: Base flow angle change $\Delta\phi$ for various c_μ at (a) $y/\delta_{99} = 0.3$; (b) $y/\delta_{99} = 0.5$; (c) $y/\delta_{99} = 0.7$; (d) $y/\delta_{99} = 3$.

effect of PA. At the condition of higher c_μ, the ratio $\bar{M}_{ws,on}/\bar{M}_{ws,off}$ even becomes negative above the encapsulated electrode, indicating that the momentum of the CF component undergoes a local inversion due to the forcing. In spite of the lower absolute reduction in w_s found in figure 5.5, the present results demonstrate that the relative change of w_s is more significant due to the weaker CF component. It can be concluded that the BFM strategy modifies the base flow mainly by modifying the target w_s.

Due to the dissimilar effects of BFM on u_s and w_s, the local direction of the plasma-affected boundary layer is expected to deviate from the natural (i.e. unforced) trajectory and shift towards the external freestream line. To confirm this assumption, the base flow angle is quantified by equation 5.3:

$$\phi(y/\delta_{99}) = \tan^{-1}(\bar{w}(y/\delta_{99})/\bar{u}(y/\delta_{99})) \tag{5.3}$$

The relative angle change $\Delta\phi = \phi_{on} - \phi_{off}$ is calculated for various c_μ and illustrated in figure 5.7. The results are calculated at several wall-normal locations, namely $y/\delta_{99} = 0.3,\ 0.5,\ 0.7$ and 3, referring to conditions inside and outside the boundary layer respectively. The results inside the boundary layer ($y/\delta_{99} = 0.3,\ 0.5\ \&\ 0.7$) evidently demonstrate the re-orientation of the boundary layer flow due to the PA forcing. Specifically, the angle change $\Delta\phi$ appears to be determined by both y/δ_{99} and c_μ, where the lower y/δ_{99} and larger c_μ lead to a larger alteration. In agreement with the behaviour of $\bar{M}_{ws,on}/\bar{M}_{ws,off}$ observed in figure 5.6(b), a similar trend is found for the base flow angle change $\Delta\phi$. Initially, the base flow is locally deviated by the PA forcing and further recovers until the PA interface, after which $\Delta\phi$ increases again and remains downstream. For cases of higher c_μ, the base flow is even inverted towards the opposite direction. On the other hand, the flow outside the boundary layer ($y/\delta_{99} = 3$) appears to be minimally influenced (figure 5.7(d)). Small deviations within $\pm 0.5°$ are nevertheless observed, which are expected to diminish further away from the wing surface.

A simple schematic is given in figure 5.8 to conceptualise the above process. As demonstrated in figure 5.8(a), inside the boundary layer ($y/\delta_{99} < 1$), the flow direction is determined by the vector components u_s and w_s while determined only by u_s outside

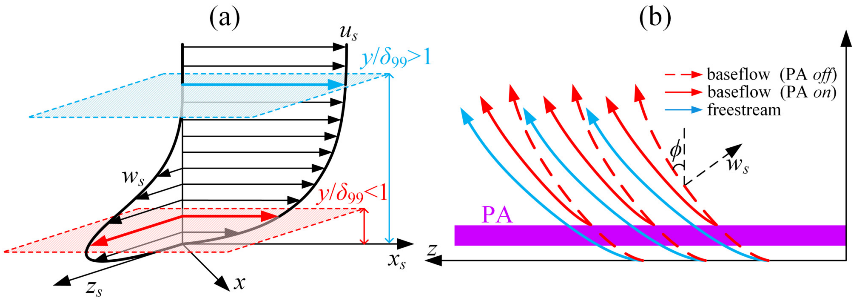

Figure 5.8: Schematic of (a) swept wing boundary layer profiles and corresponding velocity vectors in the xz plane; (b) trajectories of the boundary layer flow and freestream line.

the boundary layer ($y/\delta_{99} > 1$). Figure 5.8(b) illustrates how the PA forcing modifies the base flow trajectory within the boundary layer. At unforced flow conditions (PA-*off*), the base flow will be slightly offset from the freestream line due to the existence of w_s. When the PA is on, the freestream remains unchanged due to the limited PA effect outside the boundary layer. However, the base flow undergoes a considerable distortion due to the significant reduction of w_s. As a result, the modified base flow vectors are directed towards the freestream direction.

The results of this section generally follow observations of Wassermann & Kloker [94] and Dörr & Kloker [29]. In their numerical simulations, a two-dimensional mean-flow distortion is induced by hole-array suction or distributed PA forcing, respectively, generally followed by a diminishing CF component. The resulting distortion significantly suppresses the growth of critical stationary CFIs and becomes a decisive factor for stabilising the boundary layer. Recalling the previously observed w_s reduction and identified base flow shift, the present results experimentally confirm the ability of BFM-based PA forcing to impose a similar two-dimensional distortion on the current base flow.

5.5. Effects on Crossflow Instabilities

In this section, the streamwise evolution of stationary and travelling CFIs is investigated under the PA forcing. During the experimental investigation, the PA is operated at a fixed set of parameters ($V_{p\text{–}p} = 14\,\text{kV}$, $U_\infty = 22\,\text{m/s}$, $c_\mu = 1.65$). Two DRE cases of different forcing amplitudes are investigated, primarily aimed at introducing stationary CF vortices of low (DRE-L) or high (DRE-H) amplitude respectively. The motivation in varying the initial amplitudes of stationary CFI modes is to examine the influence of the BFM effect on linearly (i.e. low amplitude) and non-linearly growing (i.e. high amplitude) CFI modes.

5.5.1. Stationary Structures

The time-average velocity $\bar{w}$ at $x/c_x = 0.225$ for the representative case DRE-H is illustrated in figure 5.9(a), revealing uniform stationary vortices appearing at the

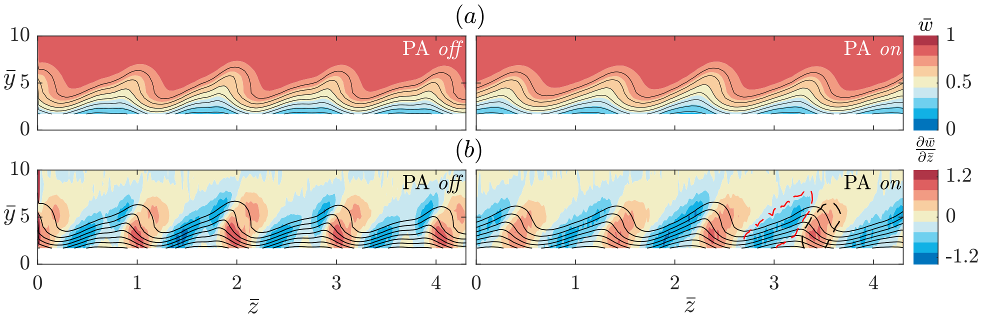

FIGURE 5.9: (a) Time-average velocity fields $\bar{w}$ and (b) Spanwise gradient of mean flow $\partial\bar{w}/\partial\bar{z}$ for DRE-H case. Measuring plane location is at $x/c_x = 0.225$, black iso-lines illustrate $\bar{w}$, 10 levels from 0 to 0.9. The regions outlined by dashed lines in (b) are based on thresholds of -0.23 and 0.5 respectively.

spacing dictated by the forcing DRE. Similar observation is found in the DRE-L case (not shown here for brevity), albeit the stationary vortices appear significantly weaker. In addition, to investigate the PA effects on the discrete stationary modes, the spanwise periodicity of the mean flow $\bar{w}$ is leveraged, through a spatial FFT of the velocity field (figure 5.9(a)) at constant $\bar{y}$. Spectral amplitudes $\bar{A} = A_{FFT}/w_\infty$ for both DRE-L and DRE-H cases are given in figure 5.10, illustrated from $x/c_x = 0.125$ to 0.3. The black dashed lines indicate the non-dimensional wavenumber $\bar{k}$ of 0.5, 1 and 2 ($\bar{k} = 1/\bar{\lambda}$, $\bar{\lambda} = \lambda/\lambda_{DRE}$), corresponding to λ of 16 mm, 8 mm and 4 mm respectively. Hereafter, the stationary mode featuring $\lambda_{DRE} = 8$ mm refers to the fundamental mode (i.e. $\bar{k} = \bar{\lambda} = 1$). The spectral results generally confirm the dominance of the fundamental mode in the boundary layer, for both DRE-L and DRE-H cases. As shown in figure 5.10(a), DRE-L effectively forces the fundamental mode for PA-*off* where evident peaks are found in the spectra. Moreover, high energy peaks are also found at the super-harmonic mode $\bar{k} = 2$ while no distinct sub-harmonic can be identified. When PA is on, the fundamental mode and super-harmonics are evidently weakened by the PA forcing. This result coincides with the general expectations of the BFM technique, as predicted by the simplified body force model (figure 5.4(a)). In spite of the attenuation of discrete spectral peaks (at the super-harmonic modes) due to the PA forcing, evident disturbances are found amplified in a broad range of $\bar{k} < 1$. While no conclusive reasoning can be provided on the origin of these long-wavelength disturbances, several possible factors can be proposed. Among others, these can include possible slow variance or modulation of plasma discharge strength along the spanwise direction due to misalignments in actuator fabrication and placement. A dedicated sensitivity study to such parameters would be important to elucidate this effect, however it falls beyond the scope of the present work.

Based on the observed weakening of stationary CFI modes due to the PA forcing, secondary effects can be expected on other important features such as the velocity gradients. Figure 5.9(b) illustrates the spanwise gradient of the time-average velocity $\partial\bar{w}/\partial\bar{z}$. Inside the core of the stationary CF vortices, two distinct regions are identified where $\partial\bar{w}/\partial\bar{z}$ obtains a local minimum and maximum respectively (regions outlined by

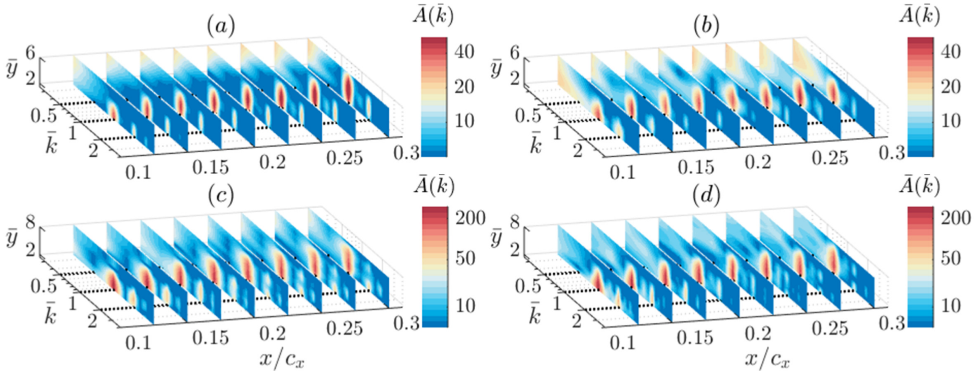

FIGURE 5.10: Non-dimensional spectral amplitude $\bar{A}(\bar{k})$ for (a) DRE-*L*, PA-*off*; (b) DRE-*L*, PA-*on*; (c) DRE-*H*, PA-*off*; (d) DRE-*H*, PA-*on*. Spectral planes are plotted from $x/c_x = 0.125$ to 0.3 with a step of 0.025. Wavenumbers $\bar{k}$ of 0.5, 1 and 2 correspond to wavelengths λ of 16 mm, 8 mm and 4 mm (black dashed lines). The colorbar follows a logarithmic scale.

dashed lines in figure 5.9(b)). Particularly in cases of strongly amplified stationary CF vortices, early theoretical and numerical work has identified the minimum spanwise gradient region to be related to the emergence of type *I* secondary instability while the maximum spanwise gradient region to be associated with the type *III* primary travelling instability [61, 94]. For PA-*off*, two local peaks are observed in both minimum and maximum gradient regions, which results from the emergence of the harmonic mode of $\lambda = 4$ mm. In contrast, the gradient regions become more continuous and centralised for PA-*on*, signalling that the PA forcing has an inhibitory effect on the harmonic mode, which is confirmed by the spectral analysis (figure 5.10). Additionally, the PA forcing noticeably reduces the maximum gradient amplitudes, indicating that the shear stress (modulated by stationary CF vortices) is weakened by the PA forcing. As earlier noted, the spanwise shear modification in the flow can be expected to have an influence on the development of travelling CFIs and other unsteady disturbances. Dedicated discussion on these effects is provided in section 5.5.3.

To further quantify the PA effects on the evolution of the fundamental mode and its harmonics, the corresponding Fourier modes are reconstructed through the inverse Fourier transform. The maximum standard deviation of the reconstructed velocity profiles is calculated as the amplitude of the interested stationary mode. The quantity is denoted as $\langle \bar{w}(\bar{k}) \rangle_{max}$ and the corresponding location is denoted as $\bar{y}_{max}$. Figure 5.11 illustrates the modal amplitudes pertaining to the two DRE cases with selected Fourier modes of $\bar{k}=0.5$, 1, 2 and 4 (corresponding to $\lambda=16$, 8, 4, 2 mm). Specifically, in the DRE-*L* case, the cyan line in figure 5.11(a) illustrates amplitudes of the fundamental mode estimated by LST at PA-*off*, artificially scaled to match with the experimental amplitude of PA-*off* at $x/c_x = 0.3$. The blue line illustrates the LST amplitudes of PA-*on* and matches with the LST amplitude of PA-*off* at the starting point ($x/c_x=0.0594$).

Evidently, the experimental growth rate of the fundamental mode agrees well

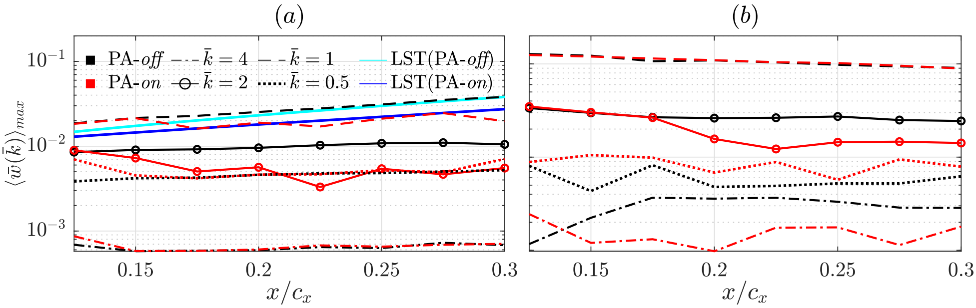

Figure 5.11: Amplitudes of stationary Fourier modes for (a) DRE-L; (b) DRE-H. Data points are plotted from x/c_x=0.125 to 0.3 with a step of 0.025. The wavenumber $\bar{k}$ = 0.25, 0.5, 1 and 2 correspond to λ = 16, 8, 4 and 2 mm respectively.

with the LST prediction, confirming the linearity of the DRE-L case. For PA-*on*, the fundamental mode amplitudes qualitatively match with the LST prediction. A significant reduction of the fundamental mode (approximately 32.1% at x/c_x=0.25) is found in experimental results, demonstrating the stabilising effect of the BFM technique. Similarly, the PA forcing effectively reduces the super-harmonic mode $\bar{k}$ = 2 while having no evident effect on the sub-harmonic mode $\bar{k}$ = 0.5. The amplitude reduction of the super-harmonic stationary modes can be attributed to several combined effects. Firstly, as the fundamental mode is suppressed, the resulting non-linear growth of higher-order harmonics can be expected to be delayed. Secondly, as originally hypothesised for the BFM technique, the suppression of the CF component in the plasma region stabilises the boundary layer for CFI modes of all wavelengths, including the $\bar{k}$=2 mode. Figure 5.11(b) illustrates the modal amplitudes for the DRE-H case. As expected from the relatively higher h_{DRE}, the fundamental mode in the imaged domain features significantly larger amplitudes compared with DRE-L. In addition, the fundamental mode is not growing and even mildly decays downstream, no longer agreeing with the LST prediction. This signifies a possible non-linear amplitude saturation, which is reached upstream of the measurement domain. In combination to the development of the characteristic secondary lobe of CF vortices evident in figure 5.9(a), this behaviour indicates the non-linear stage of stationary CFIs for the DRE-H case. Considering the PA forcing, compared with DRE-L, the fundamental mode in the DRE-H case appears almost unaffected by the BFM effect. On the other hand, the super-harmonic modes $\bar{k}$=2 and $\bar{k}$=4 are significantly weakened by the PA forcing, similar to the observations in DRE-L. This outcome can be attributed to the specific DRE amplitude (i.e. h_{DRE}), which in turn conditions the strength of stationary CF vortices arriving at the PA forcing region. Specifically, the inability of BFM to impart noticeable changes on the fundamental mode within the measurement domain can be related to the already high amplitude of the latter as they reach the plasma forcing region. In addition, even if there would be a local amplitude decrease due to BFM, the saturation of the fundamental mode upstream of the observed domain would prevent it from growing further in both PA-*on* and PA-*off* cases. In contrast, it appears that the super-harmonic modes are more susceptible to

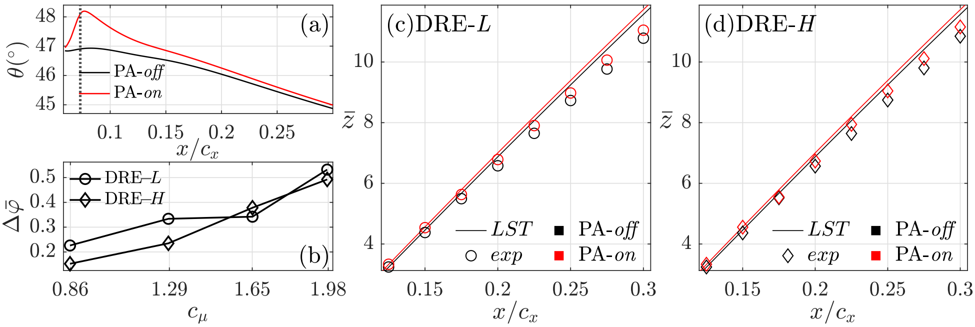

FIGURE 5.12: (a) Wavenumber vector angle θ of the fundamental stationary mode calculated from LST. Vertical dashed line indicates the PA location; (b) Experimentally determined relative phase shift of the fundamental mode versus momentum coefficient c_μ at $x/c_c = 0.275$; Fundamental mode trajectories from experiment and LST for (c) DRE-L and (d) DRE-H.

the BFM authority, which reconciles well with the LST results where N factors are more effectively reduced for sub-critical stationary modes in the considered domain (figure 5.4(a), $x/c_x = 0.125$ to 0.3). These observations suggest that the BFM's effects can show a dependence to the wavelengths of incoming stationary CFIs. If so, the wavelength of the instabilities arriving at the PA location can be a deciding factor for the success of BFM method, in addition to the expected influence of the momentum coefficient (i.e. relative forcing strength). Further parametric variations of forced mode wavelengths are deemed necessary in future work in order to clarify this point.

5.5.2. STATIONARY STRUCTURE TRAJECTORY

In addition to modifying amplitudes of stationary structures, the BFM strategy shows an evident effect on the stationary CF vortices' trajectories. During the experiment, the PA forcing was found to produce a notable spanwise shift of stationary CF vortices along the z axis in both DRE cases, as already demonstrated by the DRE-H case in figure 5.9(a). Specifically, while the CF vortices remain topologically similar between PA-*on* and PA-*off* cases, they are evidently shifted towards $+z$ thus the wavenumber vector is forced towards the x axis. This shift has been also observed in previous experimental and numerical studies and related to the local plasma-based BFM effects [4, 29]. It can be hypothesised that the spanwise shift of stationary CF vortices is coupled to the previously observed re-orientation of the base flow (figure 5.8), further reflecting the global alteration of the boundary layer. To verify the experimentally observed spanwise shift of the CF vortices, a theoretical prediction of trajectory of the fundamental mode is calculated based on the previous LST results ($c_\mu = 1.65$), following equation 5.4.

$$z = \int_0^x \tan\theta \, dx \tag{5.4}$$

where θ is the angle between the fundamental mode trajectory and the x axis. By convention, the angle θ is calculated as $\theta = \tan^{-1}(\beta_r/\alpha_r) + \pi/2$ in this Chapter and illustrated in figure 5.12(a). Specifically, α_r is the real component of the complex streamwise wavenumber α and β_r is the real spanwise wavenumber β [58]. As expected, θ is significantly altered at the PA forcing location (dashed line) while it collapses back to the non-forced values (PA-*off*) shortly downstream, demonstrating the localised effects of the PA forcing. In order to track the trajectory of the fundamental mode from the experimental data, the spanwise shift is calculated as $\bar{\varphi} \cdot \lambda_{DRE}$ at the location $\bar{y}_{max}$ where $\bar{\varphi} = \varphi/2\pi$ is the non-dimensional phase extracted from the spanwise FFT spectrum (figure 5.10). It should be noted that, the experimental spanwise shift $\bar{\varphi} \cdot \lambda_{DRE}$ is calculated in reference to the X axis and needs to be transformed to the x axis for comparison with LST results. The combined results are depicted in the xz plane and shown in figure 5.12(c) and (d). As expected, in the DRE-L case, the spanwise shift of the CF vortices is detected by LST and the results show a good agreement with the experimental measurements, though a small discrepancy is found downstream. Moreover, the vortex trajectory for PA-*on* appears to be parallel to the one of PA-*off*, due to the recovered angle θ downstream of the forcing area. Moreover, the vortex trajectories of DRE-H show a similarity to those of the DRE-L case. It appears that the modified trajectory of the stationary modes is independent from the local vortex amplitude and more likely to be determined by the modified boundary layer stability properties. Supplementary measurements at various PA forcing conditions (i.e. $12 - 15\,\mathrm{kV}$ and $U_\infty = 22\,\mathrm{m/s}$) are implemented to further elucidate the effects of forcing strength on the spanwise shift of CF vortex trajectories. The non-dimensional FFT phase $\bar{\varphi}$ of the fundamental mode is calculated at x/c_x=0.275 and the phase shift due to the PA forcing is then estimated as $\Delta\bar{\varphi}= \bar{\varphi}_{on} - \bar{\varphi}_{off}$. As shown in figure 5.12(b), for both DRE cases, the phase shift of the fundamental modes monotonically increases with c_μ. It can be concluded that the BFM-based PA generates a significant modification on the boundary layer, which in turn can be reflected by the stationary CF vortex trajectories.

The CF vortex trajectory shift due to plasma forcing provides some interesting insights into the effects of BFM in relation to other control strategies. It can be proposed that the change of CF vortex trajectories can be further used to distinguish *net* BFM effects in application cases of spanwise modulated or discrete PA. As mentioned before, discrete PA (which are commonly used for the UFD strategy [31, 93]) have been found to generate a combination of UFD and BFM effects under specific operating parameters (e.g. PA spacing, forcing amplitudes and forcing direction). Based on the current results, it can be concluded that for applications of discrete PA, the relative importance of BFM effects can be inferred by the change of CF vortex trajectories. Furthermore, the current outcome implies that the BFM strategy could be potentially beneficial to the direct attenuation strategy. Specifically, one of the application challenges for the direct attenuation strategy is the strict position accuracy with respect to the target stationary CF vortices. To resolve this problem, a BFM-based PA can be operated upstream of the control region to re-orient the target CF vortices (granted they are properly detected) to the desired locations by finely adjusting c_μ.

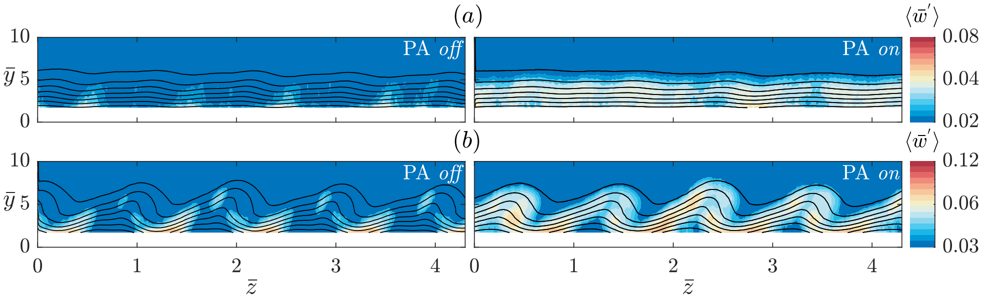

FIGURE 5.13: Standard deviation of temporal velocity fluctuations $\langle \bar{w}' \rangle$ for (a) DRE-L; (b) DRE-H. Measuring plane location is at $x/c_x = 0.225$ and black iso-lines illustrate $\bar{w}$, 10 levels from 0 to 0.9.

5.5.3. UNSTEADY STRUCTURES

Notwithstanding the identified sensitivity to DRE amplitudes, the general amplitude reduction of stationary CFIs and the trajectory alteration are attributed to the prime BFM mechanism, which reflects the overall boundary layer stabilisation. Nonetheless, the PA forcing can also impose additional effects on the boundary layer. As earlier mentioned, realistic DBD forcing can inherently induce unsteady perturbations, which feature larger growth rates (than stationary CFI modes). Figure 5.13 illustrates the standard deviation of temporal spanwise velocity fluctuations $\langle \bar{w}' \rangle$ for both DRE cases at $x/c_x = 0.225$. Evidently, unsteady fluctuations are considerably enhanced by the PA forcing, possibly resulting from quasi-stochastic processes in the PA micro-discharge, as suggested by Moralev *et al.* [64]. As expected, due to the stronger stationary CF vortices (i.e. stronger shear stress modulation) for DRE-H, the plasma-induced fluctuations are largely amplified and located in two distinct regions corresponding to the minimum and maximum $\partial \bar{w}/\partial \bar{z}$. In contrast, the unsteady fluctuations for DRE-L are only mildly amplified without an evident spatial arrangement, due to the relatively weak stationary vortices. Based on the predictions of LST calculations shown earlier, it is likely that part of these coherent structures is related to the development of naturally unstable modes such as type *III*, which essentially result from the interaction between stationary and travelling CFIs or secondary instabilities of type *I* and type *II* modes. However, these fluctuations cannot be conclusively segregated due to the absence of frequency information in the PIV measurements. As such, the fluctuation field will be further treated as a whole.

The amplitudes of the unsteady fluctuations are further evaluated as below [34]:

$$\bar{B} = \frac{1}{z_{max}} \frac{1}{\delta_{99}} \int_0^{z_{max}} \int_0^{\delta_{99}} \langle \bar{w}' \rangle ds \tag{5.5}$$

where z_{max} is the spanwise extent of the measurement plane. The integral amplitudes $\bar{B}$ are collected in figure 5.14 along with the ratio $\bar{B}_{on}/\bar{B}_{off}$ (blue line). In contrast to the identified reduction of stationary CFIs due to the BFM effect, considerable unsteady disturbances are enhanced by the PA operation despite the remarkably reduced N factors for travelling CFI modes predicted by LST. Compared with DRE-L, the fluctuation amplitudes are evidently higher in the DRE-H case though the ratio

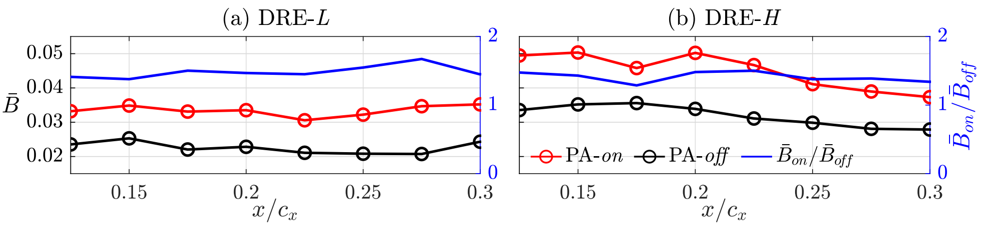

FIGURE 5.14: Integral amplitudes of unsteady disturbances for (a) DRE-L; (b)DRE-H. The blue line illustrates the ratio $\bar{B}_{on}/\bar{B}_{off}$ and refers to the right y axis.

$\bar{B}_{on}/\bar{B}_{off}$ maintains the same level for both DREs.

The considerable unsteady fluctuations observed in this section, reconcile with the work of Downs & White [34]. In their highest T_u case, stationary CFI modes are found to be weakened through non-linear interaction with travelling CFIs of sufficient amplitudes. Though the current experiment was conducted in different windtunnel conditions (i.e. low T_u), there still remains the possibility that plasma-induced fluctuations contribute to the reduction of stationary CFI modes, as observed in section 5.5.1. Nonetheless, this assumption can't be confirmed in the present work. For future work to validate this assumption, the DRE array needs to be placed downstream of PA to eliminate the BFM effects.

Overall, it can be concluded that the PA forcing essentially imposes two (potentially competing) effects in the boundary layer. One is generally reducing stationary CFIs and the other is enhancing unsteady fluctuations.

5.6. CONCLUSION

In this Chapter, a DBD plasma actuator specially configured to enable the BFM strategy is used to control a swept wing boundary layer. The spanwise-invariant PA is constructed and positioned close to the leading edge (x/c_x=0.073). The actuator is oriented to produce a volume-distributed body force normal to the leading edge in a direction against the incoming flow. The base flow modification is investigated under various PA momentum coefficients c_μ. Consistent with past evidence of Serpieri *et al.* [87] and Yadala *et al.* [99] as well as the working BFM hypothesis, the CF component is for the first time experimentally proven to be reduced by the BFM-based PA forcing. As expected, higher c_μ leads to a more effective reduction of the CF component. In addition it is found that the BFM strategy is more effective in manipulating the CF component w_s, even though the added momentum is delivered in the bulk velocity u_s direction. As a result, the dissimilar reduction between u_s and w_s leads to a directional alteration of the base flow. The flow direction is found significantly affected near the wall while remains unchanged in the freestream, showing a strong near-wall influence of the PA forcing.

PA effects on both stationary CFIs and unsteady disturbances are investigated by planar PIV. Two DRE arrays featuring different height (h_{DRE}) are placed near the leading edge, thus conditioning linear and non-linear growth of stationary CF vortices, respectively. Both DRE cases demonstrate that the super-harmonic modes are significantly reduced due to BFM, while the fundamental mode reduction is only found in the low-amplitude DRE case. The disparity of the BFM effects in reducing the fundamental modes appears to be attributed to h_{DRE} and, in turn, the amplitudes of the stationary CF vortices in the region interacting with the plasma body force. At least in the linear growth DRE case, the general amplitude reduction of stationary CFIs agrees with the LST results, demonstrating the BFM effect due to the PA forcing.

A particular effect identified in the present study is a notable spanwise shift of the stationary CF vortex trajectories due to the PA forcing. The effect is experimentally observed as well as predicted by LST. The modification of the trajectory is found to originate from the change of local boundary layer stability in the plasma region. While this shift is expected to be largely irrelevant to the effectiveness of BFM as a transition delay technique, the ability of the PA forcing to shift CF vortices might be leveraged in other flow control techniques in which spatial phase of the instabilities is important (e.g. the localized suction technique [37] and the plasma-based direct attenuation strategy [30]).

Finally, in contrast to the reduced stationary CFIs, unsteady velocity fluctuations are found to be intensively amplified by the PA forcing in both DRE amplitude cases. These enhanced unsteady disturbances can possibly contribute to the reduction of stationary CFIs. On the other hand, their significant growth rates can destabilise the boundary layer thus weakening the BFM net effect. These competing effects emerge as a key point and challenge in need of further investigation towards improving the BFM performance.

6

PARAMETRIC DEPENDENCY OF THE PLASMA-BASED BFM EFFECT

In this Chapter, CFIs and laminar-turbulent transition are controlled on the M3J model, through the plasma-based BFM technique. The simplified body force model and LST are applied to predict the net BFM effect on CFIs. Experiments are conducted in the LTT with a spanwise-invariant PA installed near the leading edge and operated at constant input voltage and frequency. Various parameters of the plasma-based BFM technique are investigated, namely the Reynolds number Re, angle of attack α *and the wavelength* λ *of excited stationary CFI modes. Stationary and travelling CFIs are quantified by planar PIV while the transition topology and location are recorded by IR thermography. The results generally confirm the stabilization effect of plasma-based BFM on the swept wing boundary layer and transition delay is achieved within specific combinations of Re,* α *and* λ.

K.Peng, F.Avallone and M.Kotsonis. *Plasma-based base flow modification on swept wing boundary layers: dependence on flow parameters.* (under review, Journal of Fluid Mechanics)

6.1. INTRODUCTION

The efficacy of plasma-based BFM in reducing the CF component and stationary CFIs has been demonstrated numerically and experimentally by previous Chapters. However, the results also imply that the effects of the plasma-based BFM on CFIs can be complex, especially considering the manifestations of PAs in realistic flow conditions. In these cases, a DBD PA supplied with AC high voltage power will excite a strongly dynamic forcing. As summarized in section 1.3.4, the PA forcing comprises two parts, namely a steady and unsteady component. Specifically, the non-deterministic unsteady component appears to be an unavoidable effect of the plasma-based BFM (due to the quasi-stochastic nature of plasma micro-discharge formations), further influencing the transitional process. This complexifies the transition control goal because the induced travelling CFIs may non-linearly interact with stationary CFIs, causing a rapid spectral broadening of the perturbation system and ultimately advancing transition, as found by Arndt *et al.* [2], Corke *et al.* [19].

In conclusion, the plasma-based BFM technique comprises two major effects, namely the 'nominal' net BFM effect responsible for the global stabilisation of the boundary layer, and an intrinsic forcing unsteadiness which can introduce unwanted travelling CFIs. Therefore, the successful deployment of plasma-based BFM control necessitates the elucidation of these two competing effects. The present work deploys a range of methodologies to elucidate these effects. Firstly, a low-fidelity numerical evaluation of the net BFM effect on primary stationary and travelling CFI modes is performed, through the simplified body force model and LST analysis, coupled with an experimentally-derived plasma body force distribution. The effects of plasma-based BFM on CFIs and transition are further experimentally investigated by planar PIV and IR thermography respectively, under variation of critical parameters such as Reynolds number Re, angle of attack α and wavelengths λ of critical stationary CFI modes.

6.2. EXPERIMENTAL SETUP AND METHODOLOGY

In this Chapter, the experimental measurements are performed on the swept wing model $M3J$ in the LTT, which features a low $T_u < 0.03\%$. Measurements are performed at various angle of attack α (ranging from 2.3° to 4°) and various global Re (ranging from 2.5×10^6 to 3.7×10^6), for which the flow approximately attains infinite swept wing conditions. Figure 6.1(a) illustrates the $M3J$ geometry (in the x axis) and a representative pressure coefficient C_p distribution under conditions of $\alpha=2.5°$ and $Re=2.5\times10^6$. The similarity of the two pressure coefficients confirms the attainment of spanwise-invariant conditions at current flow parameters. Specifically, the numerical calculation of section 6.3 only considers the case of $Re = 2.5 \times 10^6$. The numerical velocity quantities are non-dimensionalized by the freestream velocity $u_\infty = 20.6\,\mathrm{m/s}$ which corresponds to $Re=2.5 \times 10^6$. Whereas in section 6.4, various Re cases are considered (from $Re = 2.5 \times 10^6$ to $Re = 3.7 \times 10^6$). Therefore, the PIV-measured velocity components for various Re cases are non-dimensionalized by the corresponding freestream velocity U_∞. The spanwise distance z and wall-normal distance y are non-dimensionalized by the global reference length δ_0. Specifically, δ_0 is

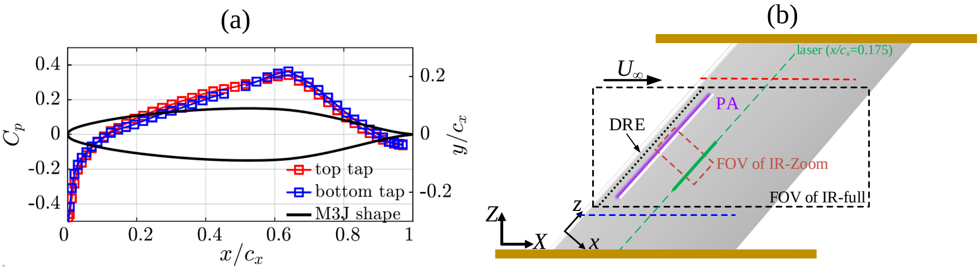

FIGURE 6.1: (a) Cross-section of $M3J$ (in the x direction) and experimental pressure coefficient C_p at $\alpha = 2.5°$ and $Re = 2.5 \times 10^6$; (b) Sketch of $M3J$ with PA. The pressure tap locations are displayed by red and blue dashed lines. Two dashed boxes in (b) indicate fields of view (FOV) for cameras IR-Full and IR-Zoom respectively.

Case	λ_{DRE}	$\bar{\lambda}_{DRE}$	x/c_x	d_{DRE} (mm)	h_{DRE} (mm)
DRP	/	/	0.015-0.025	/	0.012 ± 0.005
DRE-A	6	50	0.02	1.772 ± 0.017	0.1147 ± 0.0023
DRE-B	8	66.67	0.02		
DRE-C	10	83.33	0.02		

TABLE 6.1: Geometric parameters and chord locations of roughness arrays

the Blasius length scale identified in the simplified body force model of section 6.3. δ_0 is calculated as $\delta_0 = \sqrt{\nu s_0/u_0} = 1.2 \times 10^{-4}$ m where $u_0 = 15.42$ m/s is the boundary layer edge velocity at $x/c_x = 0.0083$. ν refers to the air kinematic viscosity and $s_0 = 0.0151$ m is the surface distance from the stagnation point to $x/c_x = 0.0083$.

To enhance the stationary CFIs, two types of surface roughness arrays are designed and manufactured to enhance stationary CFIs, namely the DRP and DREs (detailed in section 2.2). Specifically, the DRP is used to trigger a broad-spectrum of stationary CFIs, appearing in non-deterministic spanwise wavelengths. In contrast, for triggering deterministic, single-wavelength modes, DRE arrays are used. Several DRE arrays of various spanwise spacings (i.e. $\lambda_{DRE} = 6$ mm, 8 mm and 10 mm) are designed and fabricated in-house. The reported geometrical parameters of DRP and DREs are summarised in table 6.1. In this Chapter, the symbols λ_6, λ_8 and λ_{10} refer to the dimensional wavelengths of 6 mm, 8 mm and 10 mm. These wavelengths are non-dimensionalized by δ_0, resulting in $\bar{\lambda}_6 = 50$, $\bar{\lambda}_8 = 66.67$ and $\bar{\lambda}_{10} = 83.33$. Corresponding wavenumbers can be defined as $k_6 = 1/\lambda_6$, $k_8 = 1/\lambda_8$ and $k_{10} = 1/\lambda_{10}$ (thus $\bar{k}_6 = 1/\bar{\lambda}_6$, $\bar{k}_8 = 1/\bar{\lambda}_8$ and $\bar{k}_{10} = 1/\bar{\lambda}_{10}$).

To enable the plasma-based BFM, a 2D spanwise-invariant DBD PA is utilised, with both exposed and encapsulated electrodes feature a streamwise width of 5 mm. Specifically, the encapsulated electrode is configured upstream of the exposed electrode with the interface located at x/c_x=0.035. A PETG foil with a thickness of 500 μm is used as the dielectric material, which is further wrapped around the leading edge of the wing and extends downstream to avoid potential surface irregularities. For the entirety of this work, the PA is powered by a GBS Electronik Minipuls 4 high-voltage amplifier, where the supplied voltage V_{p-p} is fixed at 6.5 kV and the actuation frequency f_{AC} is fixed at 12.5 kHz.

Velocity vector fields are extracted by planar PIV for various Re number conditions while the $M3J$ model is set at $\alpha = 2.5°$. Micron-diameter seeding particles are illuminated by a Quantel Evergreen Nd:YAG dual cavity laser (200 mJ at the wavelength of 532 nm), providing a laser sheet aligned to the yz plane at x/c_x=0.175. Per test case, one LaVision imager camera (sCMOS, 2560 px × 2160 px) acquires 600 image pairs at a sampling frequency of 15 Hz. For the various Re number cases, the inter-frame time interval of image pairs is properly adjusted such that the freestream particle displacement is around 12 pixels. Particle images are further processed in LaVision Davis 10 through cross-correlation to obtain the velocity vector $[v\,w]$. The average flow field is constructed as the average of 600 instantaneous PIV vector fields. Specifically, the resulted velocity vectors near the wall ($y < 0.3$ mm) show extremely large values instead of diminishing to zero, due to the laser light reflections and significant velocity uncertainty in that region. These velocity data are considered as unreliable and are discarded in subsequent analyses. Additionally, y_{min} refers to $y = 0.3$ mm for the entire work of this Chapter. The case of DRE-A at $Re = 3.7 \times 10^6$, which is anticipated to have the highest level of velocity uncertainty, is used to compute the time-averaged uncertainty. As a consequence, the maximum uncertainty for w is found as $0.5\%\,U_\infty$ in the boundary layer region, while the average uncertainty is identified as $0.012\%\,U_\infty$ in the freestream region.

Two Optris PI640 IR cameras IR-full and IR-zoom are utilised to measure the wing surface temperature. The FOVs of IR-full and IR-zoom are outlined in figure 6.1(b). Specifically, the FOV of camera IR-zoom contains a domain from $x/c_x = 0.0565$ to 0.2385. Approximately 40 images are recorded by these cameras for each run at a sampling frequency $f_s = 4$ Hz, which are later time-averaged to reduce background noise. Additionally, several halogen lamps are used to radiate the wing model in order to improve the thermal contrast. The effects of PA on transition are thoroughly investigated, through the quantification methods of location and blurriness introduced in section 2.4.1.

6.3. Estimation of Net BFM Effect

In this section, the simplified body force model is employed to evaluate the plasma-induced modification of the base flow on the $M3J$ wing. By using the finite element multiphysics tool *Comsol*, the simplified body force model essentially solves the incompressible Navier-Stokes equations coupled with a volume-distributed body force term, representing the plasma forcing effect. To cross-verify the *Comsol* predictions, solutions of 2.5D boundary layer equations are calculated, based on the experimental wing pressure distribution of a reference case ($Re = 2.5 \times 10^6$ and $\alpha = 2.5°$). The resulting velocity field $[u\,v\,w]$ at $x/c_x = 0.083$ are further adopted as inflow boundary conditions to the simplified body force model. Evidently, the velocity profiles calculated from *Comsol* exhibit a satisfactory agreement with the boundary layer solutions, as validated by figure 6.2 at several chord locations. To obtain the body force distribution of the PA, an additional PIV characterisation experiment is conducted in quiescent flow, at conditions of V_{p-p}=7 kV and f_{AC}=12.5 kHz. It

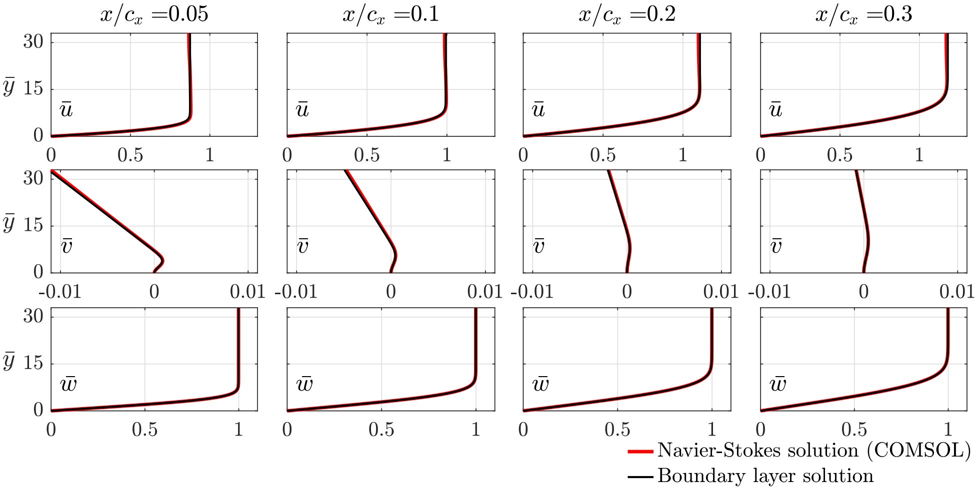

FIGURE 6.2: Velocity profiles resulting from the solution of 2.5D boundary layer equations and the full Navier-Stokes equations (i.e., *Comsol*). The columns from left to right correspond to x/c_x=0.05, 0.1, 0.2 and 0.3 respectively.

should be stressed that the supplied voltage used in the statistical measurement is slightly higher than the V_{p-p}=6.5 kV used in the subsequent PIV measurements (section 6.4). The V_{p-p} is deliberately moderated to mitigate potential degradation of the PA electrodes during extended PIV measurements. Nevertheless, this minor adjustment does not substantially impact the ensuing analyses, particularly in light of the qualitative nature of the numerical calculations.

Figure 6.3(a) illustrates the time-average velocity field (x-component), which is used to calculate the body force distribution, through the time-average method (section 2.3.2). Figure 6.3(b) illustrates the estimated body force distribution F_x, which is further used in the simplified model as a source term of the NS momentum equations. The streamline-aligned velocity u_s and CF component w_s are calculated based on the transformation used in Chapter 5 and non-dimensionalized as $\bar{u}_s$ and $\bar{w}_s$. The plasma-caused alterations are further calculated for $\bar{u}_s$ and $\bar{w}_s$ and denoted as $\Delta\bar{u}_s$ and $\Delta\bar{w}_s$ respectively (e.g. $\Delta\bar{u}_s$=$\bar{u}_{s,on} - \bar{u}_{s,off}$). The results are presented in figure 6.3(c) and (d), where the velocity profiles u_s/u_{se} and w_s/u_{se} are compared at several streamwise chord locations. Particularly, u_{se} is the boundary layer edge velocity of u_s. As expected, both streamline-aligned velocity and CF component are reduced due to the PA forcing. Overall, the current results of $\bar{u}_s$ and $\bar{w}_s$ show sufficient agreement to Chapter 5 and provide a first quantification of net BFM effect.

The LST analysis is further performed on the calculated base flow to evaluate the PA effects on CFIs. Non-dimensional spatial growth rate $-\bar{\alpha}_i = -\alpha_i\delta_0$ and N factor (the streamwise integral of -$\bar{\alpha}_i$) are calculated for both PA-*off* and PA-*on* conditions. Several studies have shown that travelling CFI modes essentially consist of negative and positive travelling modes, which propagate along and against the CF

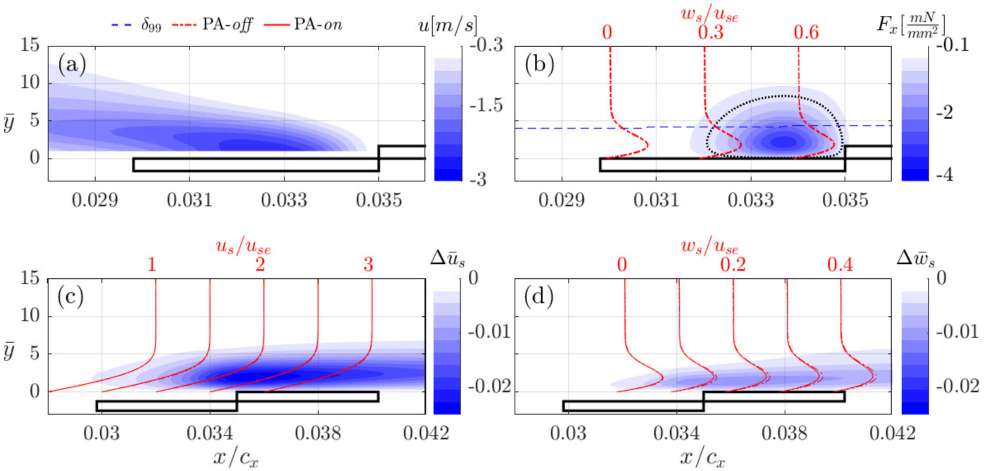

6

FIGURE 6.3: (a) Time-average velocity field u; (b) Body force F_x (x-component). The dotted line denotes F_x=10%$F_{x,max}$, where $F_{x,max} = max(F_x)$. The CF profiles w_s/u_{se} are at x/c_x=0.03, 0.032 and 0.034 respectively. The boundary layer thickness δ_{99} is computed under plasma-*off*; (c) Streamline-aligned velocity reduction $\Delta\bar{u}_s$. The u_s/u_{se} profiles are illustrated at x/c_x=0.032, 0.034, 0.036, 0.038 and 0.04 with abscissa-shift of 0.5; (d) Same as (c) but for CF velocity reduction $\Delta\bar{w}_s$ and CF profiles of w_s/u_{se} (with abscissa-shift of 0.1).

direction respectively. Nonetheless, compared to negative travelling modes, positive travelling modes feature significantly higher growth rates and are more dominant in the boundary layer development, as discussed in previous sections. Therefore, the following discussion only considers positive travelling CFI modes. Figure 6.4 illustrates the plasma-induced alteration of non-dimensional growth rate $\Delta\bar{\alpha}_i = (-\bar{\alpha}_{i,on} - (-\bar{\alpha}_{i,off}))$ and N factor, which are denoted by colours and contours respectively. As expected, both stationary and travelling CFI modes are reduced via the net BFM effect due to the reduction of their source, namely the CF component, agreeing well with previous studies [29, 87]. Near the PA location, travelling CFI modes appear to suffer a larger reduction of growth rates, especially those of smaller wavelengths. This disproportionate reduction of stationary and travelling CFI modes is also observed by Dörr & Kloker [29], Guo & Kloker [40], which may be related to the distinct wavenumber vector directions of these modes, as suggested by Guo & Kloker [40].

Considering the potential inception and amplification of travelling CFI modes through realistic (i.e. deterministic and non-deterministic) PA operation, it becomes intriguing to investigate the plasma-caused alterations of the boundary layer's response to stationary and travelling CFI modes. Despite the localized momentum modification due to the PA forcing, its impact on the boundary layer extends considerably downstream. Hence, it is reasonable to compare the N factor of CFI modes, as it reflects their integrated responses due to the overall alteration of the boundary layer. As such, the ratio of N_t/N_s is selected to reflect the susceptivity of boundary layer to stationary and travelling modes, where N_s and N_t refer to N factors of stationary and travelling CFI modes respectively. The ratio N_t/N_s of two representative cases

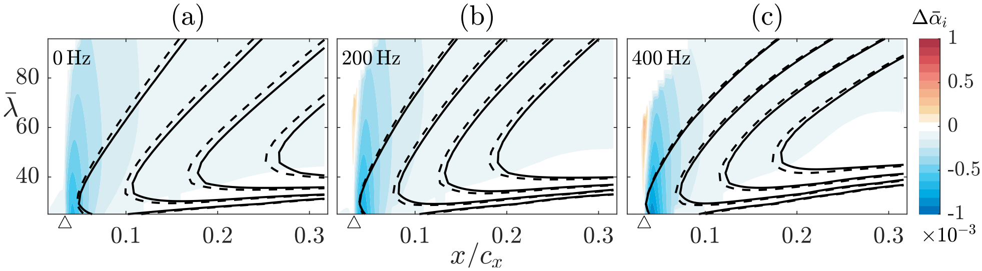

FIGURE 6.4: Change of growth rate $\Delta\bar{\alpha}_i$ (coloured) and N factor (iso-lines) for (a) stationary CFI modes and (b)-(c) travelling CFI modes. N factor iso-lines increase from 1 with an interval of 1 (starting from left). Dashed iso-lines refer to PA-*off* and solid iso-lines refer to PA-*on*. The triangle indicates the PA intersection.

is illustrated in figure 6.5(a) and (b), where travelling CFI modes are considered at $f = 200$ Hz and $f = 400$ Hz respectively, while sharing the same wavelengths $\bar{\lambda}$ as stationary CFI modes.

A noteworthy observation is that, for both PA-*off* and PA-*on*, the ratio N_t/N_s for all examined modes consistently increases from 0 to 1. This phenomenon can be traced to the more upstream locations of the neutral points of stationary CFI modes compared to their travelling counterparts (given the same spanwise wavelength). Nonetheless, the ratio rapidly surpasses 1, due to the more pronounced downstream growth rates of travelling modes. The ratio N_t/N_s exhibits a noticeably higher value downstream under the PA-*on* condition, indicating an enhanced susceptibility of the boundary layer to travelling CFI modes due to the PA forcing. This observation also holds true for other frequencies of travelling modes such as $f = 400, 500$ and 600 Hz and is not shown here for brevity. The ratio of envelop N factors is further calculated for stationary and travelling CFI modes and denoted as N_t^{env}/N_s^{env}. Figure 6.5(c) illustrates the ratio N_t^{env}/N_s^{env} for the reference case of $Re = 2.5 \times 10^6$ and an additional case of higher $Re = 3.5 \times 10^6$. The CFI modes used to calculate N factor envelopes are selected in the range of most amplified CFI modes (i.e. $3\,\text{mm} \leq \lambda \leq 11.5\,\text{mm}$ and $0\,\text{Hz} \leq f \leq 600\,\text{Hz}$, with an interval of 0.5 mm and 10 Hz respectively).

Under unforced flow conditions (PA-*off*), the ratio N_t^{env}/N_s^{env} shows values greater than 1 for both low and high Re cases. This outcome implies that travelling CFIs display higher integrated growth compared to stationary CFI modes, a trend commonly observed across various studies [7, 95]. However, the ratio N_t^{env}/N_s^{env} generally exhibits smaller values at higher Re compared to lower Re. This suggests that while travelling CFI modes indeed exhibit greater integrated growth than stationary CFI modes, the growth discrepancy tends to diminish with increasing Re. When the PA is on, the ratio N_t^{env}/N_s^{env} of both low and high Re cases is significantly affected. Evidently, a rise of N_t^{env}/N_s^{env} is found downstream of the PA location and its increase becomes more prominent while moving downstream. This indicates that within the linear growth stage of these CFI modes, the net BFM effect exerts a stronger suppressive effect on stationary CFI modes compared to travelling CFI modes of comparable wavelengths. It is important to note that this conclusion cannot

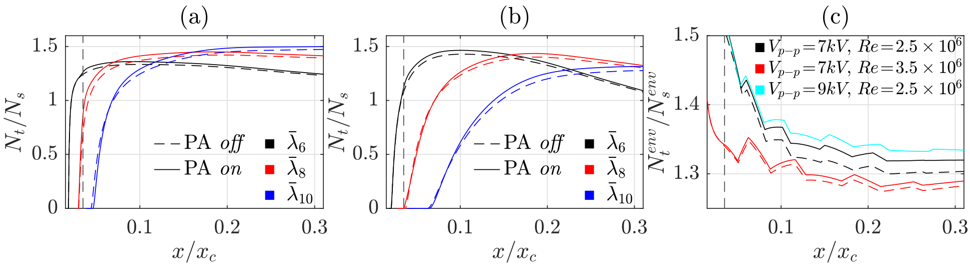

FIGURE 6.5: N factor ratio N_t/N_s for CFI modes of (a) $f = 200$ Hz and (b) $f = 400$ Hz; (c) Envelope N factor ratio N_t^{env}/N_s^{env} for various cases.

be interpreted as an indication that travelling CFI modes will obtain larger amplitudes (compared to their stationary counterparts) within the boundary layer. This is due to the fact that the ratio N_t^{env}/N_s^{env} only reflects the integrated growth ratio (thus not the amplitude ratio), but does not inform on receptivity or initial amplitudes of these modes. Nonetheless, a primary conclusion can be drawn here regarding the net BFM effect. That is, the net BFM effect weakens both stationary and travelling CFI modes. However, the suppression of stationary CFI modes is more pronounced, thus rendering the boundary layer more susceptible to travelling CFI modes. Additionally, this BFM-caused susceptibility (to travelling CFI modes) is more pronounced at lower *Re*, as implied by the larger increase of N_t^{env}/N_s^{env} at lower *Re* (figure 6.5(c)). This can probably be attributed to the larger forcing authority of PA at lower *Re*. This assumption is further evaluated by considering an additional case of $V_{p-p} = 9$ kV and $Re = 2.5 \times 10^6$, which exhibits a stronger body force than the case of $V_{p-p} = 7$ kV and $Re = 2.5 \times 10^6$. The result is shown by the cyan line in figure 6.5(c). The BFM-caused susceptibility (to travelling CFI modes) becomes more pronounced in conditions where the PA forcing shows a larger authority (i.e. lower *Re* or larger PA forcing). This observation suggests the possibility that the boundary layer susceptibility to travelling modes is related to the actual magnitude of the boundary layer CF component. This notion arises due the fact that lower *Re* and larger PA forcing essentially refer to scenarios of weaker CF components. However, it is important to underscore that there is currently insufficient evidence to confirm or refute this assumption, highlighting the need for dedicated investigations.

This result demonstrates that the BFM imposes a larger reduction to stationary modes (in the linear growth), essentially rendering the boundary layer more affected by unsteady modes. Moreover, this effect is more evident at low *Re* where the PA forcing has larger authority for manipulating the boundary layer. It can be assumed in extreme conditions, the PA forcing totally compensates the CF component, rendering the swept wing boundary layer two-dimensional. As a result, stationary CF modes are totally suppressed while unsteady CF modes are replaced by 2D unsteady instabilities such as TS waves, resulting an infinite N_t^{env}/N_s^{env}. Additionally, due to the less domination of CFIs caused by the CF reduction, the boundary layer may suffer the contamination of other instabilities such as TS waves. The growth rate -$\bar{\alpha}_i$ of two-dimensional TS waves (i.e. $\lambda = 0$ mm) are calculated in the range of 350 Hz $\leqslant f \leqslant$ 800 Hz.

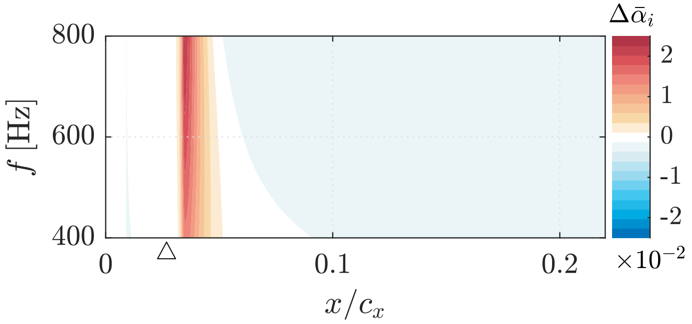

FIGURE 6.6: Growth rate reduction for TS waves.

Regarding current flow conditions and PA settings, the growth rate -$\bar{\alpha}_i$ of TS waves ultimately remain negative for both PA-*off* and PA-*on* (not shown here), indicating that the boundary layer still remains stable for TS waves after the PA modulation. Nonetheless, the growth rate reduction $\Delta\bar{\alpha}_i$ is calculated and illustrated in figure 6.6. As expected, $\Delta\bar{\alpha}_i$ shows a noticeable increase near the PA forcing, due to the locally significant CF reduction. It can be concluded that the BFM-based PA renders the boundary layer locally more two-dimensional thus weakening the suppression on TS waves. In fact, considering the two-dimensional structure and inherently unsteadiness of the PA forcing, typical TS waves may be initially amplified along with CFIs in the vicinity of PA. As a consequence, TS waves may go through a local amplification thus destabilizing the boundary layer in some extreme conditions where the PA forcing features a significant momentum coefficient c_μ. However, no sufficient evidences can be found in this work and such study of TS waves will require a dedicated effort that goes beyond the scope of this study.

6.4. EFFECTS OF PLASMA-BASED BFM ON CROSSFLOW INSTABILITIES

In this section, a 2D spanwise-invariant PA is installed and operated on the $M3J$ wing towards enabling BFM control at various *Re* number conditions. The boundary layer stability is conditioned using DRP or DREs near the leading edge, corresponding to cases DRP, DRE-A, DRE-B and DRE-C respectively (Table 6.1). Roughness conditioning is used to enhance stationary CFI modes under conditions of both PA-*off* and PA-*on*. Flow velocity fields are quantified by planar PIV measurements in the yz plane at $x/c_x = 0.175$. The following analysis aims at describing the influence of plasma-based BFM on both stationary and travelling CFIs.

6.4.1. STATIONARY CROSSFLOW INSTABILITIES

Figure 6.7(a) illustrates the time-average velocity field $\bar{w}$ (contour) and spanwise gradient $\partial\bar{w}/\partial\bar{z}$ (color) in the case of $Re = 2.5 \times 10^6$. Among all tested cases, DRP induces the least significant stationary flow perturbation, presenting a scenario of

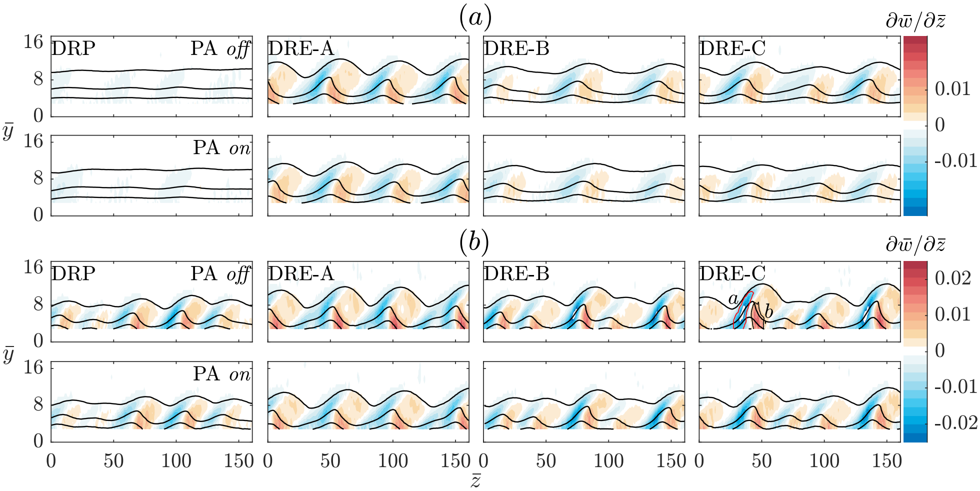

Figure 6.7: Spanwise gradient $\partial\bar{w}/\partial\bar{z}$ (color) at (a) $Re = 2.5 \times 10^6$ and (b) $Re = 3.7 \times 10^6$. Measurements are taken for DRP, DRE-A, DRE-B and DRE-C (from left to right columns) at $x/c_x = 0.175$. Black iso-lines illustrate the time-average velocity $\bar{w}$, 5 levels from 0 to 0.7.

weakly amplified stationary CFI modes. In contrast, the mean flow fields of all DRE cases show evident spanwise-periodic modulation, presenting scenarios where stationary CFI modes are significantly enhanced. Among the DRE cases, DRE-A (corresponding to a forced spanwise wavelength of 6 mm) produces considerably amplified and coherent stationary vortices. This is in agreement with the preliminary LST predictions which suggest that stationary CFI modes of smaller λ obtain larger N factors in the near-leading-edge region.

In all DRE cases the flow fields undergo evident changes when the PA starts working. Noticeably, the PA operation shifts the location of stationary CF vortices towards the $+z$ direction (i.e. more aligned with the outer inviscid streamlines). This spanwise shift of CF vortices appears as a typical outcome of the BFM strategy, attributed to the localised reduction of the CF component, as concluded in Chpater 5. More importantly, the local maximum and minimum of the spanwise velocity gradient $\partial\bar{w}/\partial\bar{z}$ are significantly weakened by the PA forcing, indicating a weakening of the stationary CF vortices. Similar observations are also found for cases at higher $Re = 3.7 \times 10^6$ (figure 6.7(b)). Alternatively, the reduction of stationary CFI modes is demonstrated and reflected by the degradation of stationary mode shape. The stationary mode shape is calculated as the spanwise standard deviation of w and denoted as $\langle w \rangle_z$. The mode shape profiles are illustrated in figure 6.8 at $Re = 2.5 \times 10^6$ and $Re = 3.7 \times 10^6$ respectively. As expected, the spanwise modulation of stationary modes is integrally weakened by the PA forcing. In addition, the secondary hump on the perturbation profiles (denoted by the circular marker) is modified by the PA as well. This secondary hump is related to the characteristic lobe structure of stationary CFIs, which coincides with the advent of non-linear interactions [42, 96]. In terms of the lowest Re cases (figure 6.8(a)), the secondary hump only occurs in DRE-A under

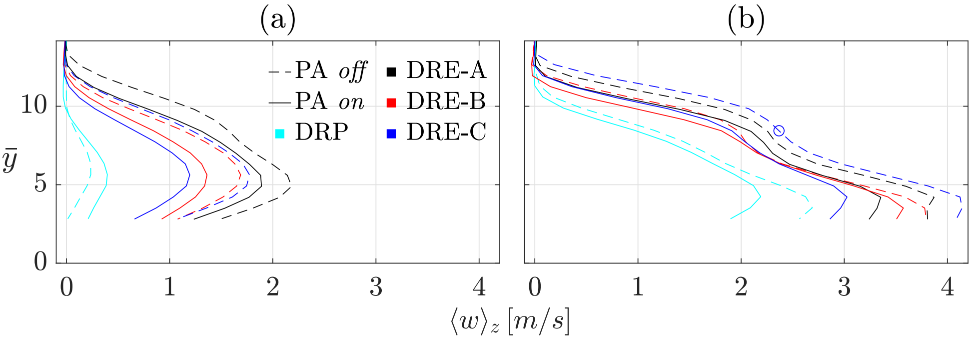

Figure 6.8: Standard deviation profiles of $\langle w \rangle_z$ at (a) $Re = 2.5 \times 10^6$ and (b) $Re = 3.7 \times 10^6$.

the condition of PA-*off*. This result indicates that stationary CFI modes of DRE-A develop fastest thus first reaching the non-linear stage, demonstrating the importance of stationary mode's receptivity. Considering that the lobe structure is commonly associated with the stationary mode saturation and onset of secondary CFIs [86], the PA forcing appears to retard the evolution of stationary CFI modes.

To better isolate the forced stationary CFI modes, the spanwise periodicity of the mean flow is leveraged through a spatial FFT of the time-average velocity fields. Representative spatial spectra at $Re = 2.5 \times 10^6$ are illustrated in figure 6.9. For PA-*off*, no significant spectral energy is observed in DRP while the $\bar{k}_6$ and $\bar{k}_8$ modes are evidently amplified in DRE-A and DRE-B, along with their harmonic modes. In spite of the successful excitation of stationary CFI modes corresponding to λ_{DRE} in DRE-A and DRE-B, the opposite is observed in DRE-C. Instead of the $\bar{k}_{10}$ mode, the $\bar{k}_6$ mode is most enhanced by DRE-C, though weaker than the one found in DRE-A. Additionally, multiple spectral modes are amplified which are not necessarily related to $\bar{k}_{10}$ or its harmonics. The apparent inability of configuration DRE-C to trigger the respective wavelength of CFIs should be attributed to the fact that the $\bar{k}_6$ mode is significantly more unstable than the $\bar{k}_{10}$ mode at the upstream region of DRE forcing, as indicated by the LST results. Notwithstanding, when PA is on, these DRE-induced spectral modes including their harmonics are evidently inhibited. In contrast, the plasma forcing appears to increase the amplitude of stationary CFIs in the DRP case.

The spanwise wavenumber spectra are further used to quantify the integral amplitude of stationary CFI modes. Specifically, the spectral energy of discrete Fourier modes is integrated from $\bar{y}_{min}$ to $\bar{y} = 25$ (i.e. $y = 3$ mm) and denoted as $\bar{A}_s(\bar{k})$. Peaks at $\bar{k}_{10}$, $\bar{k}_6$, $\bar{k}_8$ and $\bar{k}_6$ are chosen as the dominant spectral modes for DRP, DRE-A, DRE-B and DRE-C respectively. The results are illustrated in figure 6.10 at various Re numbers. Overall, the plasma-based BFM leads to a suppression of stationary CFI modes for all DRE cases as also observed in Chapter 5. It is noticed that the modes around $\bar{k}_{10}$ in DRP are slightly enhanced at lower Re though further reduced when increasing Re. Though the origin of this amplification cannot be conclusively determined here, the slow variance or modulation of PA discharge along the spanwise direction appears as a potential cause, which can result from the possible PA

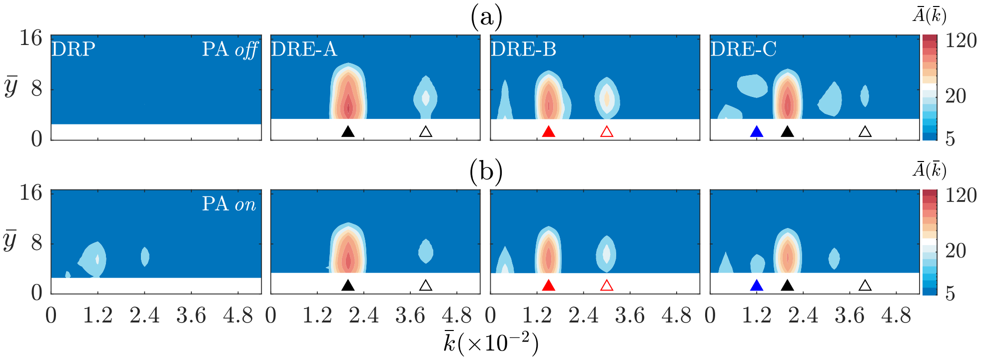

FIGURE 6.9: Non-dimensional spectral amplitude $\bar{A}(k)$ for (a) PA-*off* and (b) PA-*on* at $Re = 2.5 \times 10^6$. Black solid triangle: $\bar{k}_6$; Black empty triangle: $2\bar{k}_6$; Red solid triangle: $\bar{k}_8$; Red empty triangle: $2\bar{k}_8$; Blue solid triangle: $\bar{k}_{10}$.

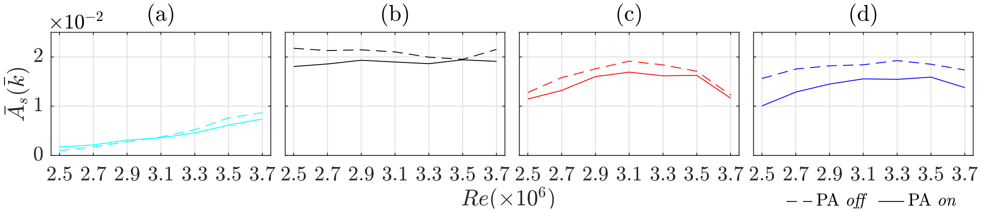

FIGURE 6.10: Non-dimensional amplitude $\bar{A}_s(k)$ of dominant spectral modes for (a) DRP; (b) DRE-A; (c) DRE-B; (d) DRE-C.

misalignment (due to the manual placement of PA on the wing model). Nonetheless, these additional modes are expected to have insignificant effects on the transition dynamics due to their weak amplitudes. This holds particularly true for DRP cases at higher *Re* and DRE cases where these additional modes are effectively suppressed by the strong dominant modes induced by the DREs.

6.4.2. TRAVELLING CROSSFLOW INSTABILITIES

The amplitude reduction of stationary CFI modes underlines the positive effects of plasma-based BFM on stabilizing the boundary layer. Notwithstanding, previous Chapters have shown that the PA operation inevitably induces travelling CFIs in the boundary layer, which might be attributed to quasi-stochastic processes within the PA micro-discharge [64]. Furthermore, the previous LST results indicate that the net BFM effect favours the suppression of stationary over travelling CFI modes, essentially renders the boundary layer more susceptive to travelling CFIs. In combination, these factors highlight the significance of travelling CFI modes in realistic applications of plasma-based BFM, adding complexity to the successful implementation of this method.

Figure 6.11 illustrates the unsteady velocity fluctuation $\langle \bar{w}' \rangle$ (color levels) overlaid with time-average velocity (contour lines) at $Re = 2.5 \times 10^6$ and $Re = 3.7 \times 10^6$

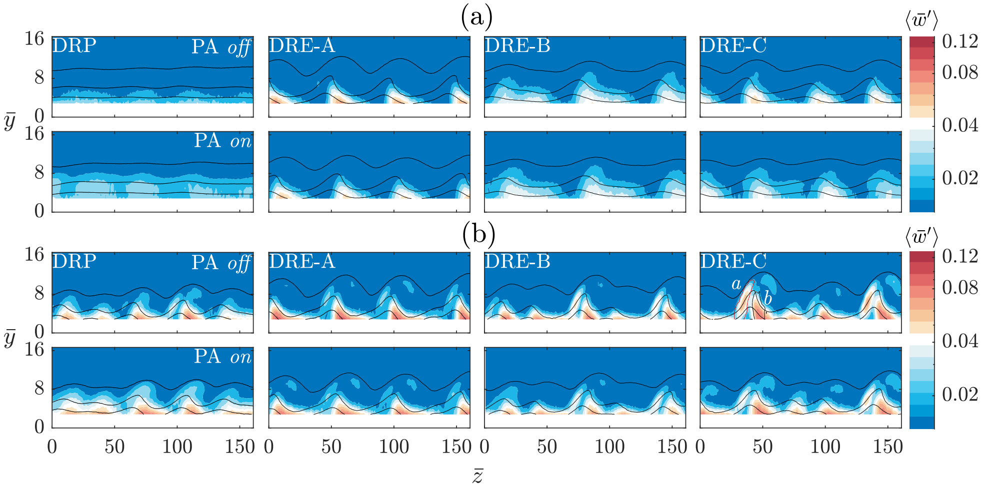

FIGURE 6.11: Non-dimensional standard deviation of temporal velocity fluctuation $\langle \bar{w}' \rangle$ for (a) $Re = 2.5 \times 10^6$ and (b) $Re = 3.7 \times 10^6$. The colorbar follows a logarithmic scale.

6

respectively. At the condition of $Re = 2.5 \times 10^6$ and PA-*off*, unsteady fluctuations already become non-negligible in the near wall region within the stationary vortex structures. Compared to the DRP case, the unsteady fluctuations are evidently more spanwise-periodic in DRE cases due to the stronger modulation of stationary CFI modes. Among all DRE cases, the unsteady fluctuations are more centralised and compact in DRE-A case, corresponding to the highly amplified state of the stationary vortices in this case. Recalling figure 6.8(a), the level of unsteady fluctuations further demonstrates that the primary CFIs of DRE-A are at a non-linear stage of growth and subject to a strong mutual interaction at $Re = 2.5 \times 10^6$ and $x/c_x = 0.175$. In contrast, the primary CFIs in DRE-B and DRE-C cases reveal a weaker interaction. When the PA is on, the plasma forcing evidently amplifies unsteady fluctuations in the DRP case, resulting in a boundary layer significantly contaminated by unsteadiness. In contrast, the PA forcing appears to only marginally affect the DRE cases. In these cases, the spanwise-modulated fluctuations become weaker centrally and tend to spread spatially w.r.t stationary structures. Similar results are observed at $Re = 3.7 \times 10^6$, though the unsteady fluctuations exhibit higher amplitudes and more pronounced modulation in the spanwise direction for both PA-*off* and PA-*on*.

These unsteady fluctuations are mainly amplified in regions of strong spanwise gradients, as shown in figure 6.7. The spatial locations of these unsteady fluctuations highly resemble the primary type *III* mode and the secondary type *I* mode [94]. However, these typical fluctuations cannot be conclusively segregated here considering the low acquisition frequency of the utilised PIV measurement technique. Nonetheless, these fluctuations are carefully examined given their intrinsic associations with type *III* and type *I* modes, as well as the mutual interactions of primary CFI modes. Hereafter, the fluctuations corresponding to the minimum $\partial \bar{w}/\partial \bar{z}$ and the maximum $\partial \bar{w}/\partial \bar{z}$ are denoted as fluctuation-a and fluctuation-b, as outlined by the red and black lines in

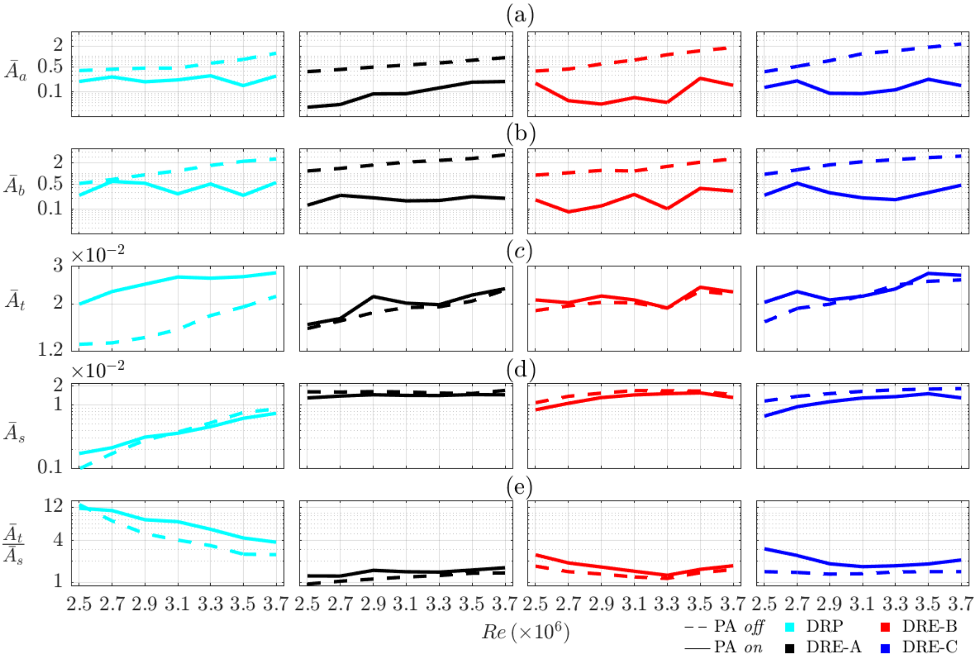

FIGURE 6.12: (a) Fluctuation-a amplitude $\bar{A}_a$; (b) Fluctuation-b amplitude $\bar{A}_b$; (c) Unsteady fluctuation amplitude $\bar{A}_t$; (d) Stationary CF mode amplitude $\bar{A}_s$; (e) Ratio of $\bar{A}_t/\bar{A}_s$. The vertical coordinates follow a logarithmic scale.

figure 6.7(b) and figure 6.11(b). These fluctuation structures are quantified following the method in Chapter 4, where the fluctuation $\langle \bar{w}' \rangle$ is integrated within specific spatial regions (i.e. masks). Specifically, the region of $\partial\bar{w}/\partial\bar{z} < -0.5\max(\partial\bar{w}/\partial\bar{z})$ is used to trace fluctuation-a structure and the region of $\partial\bar{w}/\partial\bar{z} > 0.5\max(\partial\bar{w}/\partial\bar{z})$ for fluctuation-b structure. While the threshold of 0.5 is chosen heuristically, it is kept constant for the entire parameter range, ensuring comparable outcomes. The amplitudes of the two fluctuation structures are ultimately calculated as below,

$$\bar{A}_i = \frac{1}{s_{m,i}} \int\!\!\int_s \langle \bar{w}' \rangle ds \tag{6.1}$$

where $i = a, b$ and s_m denotes the mask area.

The resulting amplitudes $\bar{A}_a$ and $\bar{A}_b$ are illustrated in figure 6.12(a) and (b) respectively. In accordance with the observations in figure 6.11, the amplitudes of fluctuation-a and fluctuation-b structures are significantly reduced by the PA forcing for all DRP and DRE cases. To facilitate the discussion, the total unsteady fluctuations and stationary CFIs are further quantified. Specifically, the total unsteady fluctuations over the entire domain are quantified as below [34],

$$\bar{A}_t = \frac{1}{\delta_{99} - y_{min}} \frac{1}{z_{max}} \int_0^{z_{max}} \int_{y_{min}}^{\delta_{99}} \langle \bar{w}' \rangle dz dy \tag{6.2}$$

where z_{max} is the spanwise extent of the PIV domain (figure 6.11) and y_{min} is the nearest to the wall position, reliably resolved by the PIV measurement (section 6.2). The results are summarised in figure 6.12(c) revealing a general amplification of travelling CFIs due to the PA forcing in all DRP and DRE cases. Though the LST results in section 6.3 indicate that the net BFM effect essentially weakens both types of CFIs, the impact of intrinsic non-deterministic unsteadiness of the PA forcing results in a relatively more amplified $\bar{A}_t$. Additionally, it is not surprising to find that $\bar{A}_t$ displays an opposing tendency compared to $\bar{A}_a$ and $\bar{A}_b$ when PA is on. This is due to the fact that unsteady fluctuations are mildly amplified by the PA outside of the region of structures a and b (typically evident in DRP cases) and are accumulatively reflected by $\bar{A}_t$. Furthermore, the amplitudes of total stationary CFI modes $\bar{A}_s$ are simply calculated as the integral of spanwise standard deviation of $\langle\bar{w}\rangle_z$ as below,

$$\bar{A}_s = \frac{1}{\delta_{99} - y_{min}} \int_{y_{min}}^{\delta_{99}} \langle\bar{w}\rangle_z dy \tag{6.3}$$

The results are shown in figure 6.12(d). As expected, the amplitudes of total stationary amplitudes agree well with the dominant mode amplitudes $\bar{A}_s(\bar{k})$ as shown in figure 6.10, indicating a general reduction of stationary CFI modes due to plasma forcing.

It should be noted that, the observed reduction of fluctuation-a and fluctuation-b structures is not contradictory to the observations of Chapter 5 where they were found to be significantly amplified in cases of strongly non-linear stationary CFIs (i.e. larger h_{DRE}). In fact, the increase of $\bar{A}_t$ and decrease of $\bar{A}_s$ imply that the reduction of fluctuation-a and fluctuation-b structures can be attributed to the significantly weakened stationary CFI modes. Ultimately, fluctuation-a and fluctuation-b structures tend to depend on the amplitude of their carrying stationary CFI modes remaining downstream of the PA forcing region. This assumption is further supported, considering that stationary CFI modes are significantly weakened by PA in the present study while remaining almost unaffected in the non-linear cases of Chapter 5

Considering the above observations, two primary outcomes governing the response of stationary and travelling CFI modes to the PA forcing can be extracted. The first scenario occurs when the net BFM effect takes dominance, leading to the suppression of both types of CFI modes, as usually found in numerical studies [29, 40]. Comparatively, the stationary CFI modes tend to be more suppressed in this case, as implied by the LST results. Alternatively, the second scenario arises when the intrinsic non-deterministic unsteadiness of PA outweighs the net BFM effect, resulting in a significant amplification of travelling CFI modes along with the suppression of stationary CFI modes, as demonstrated in the present study. Notwithstanding, in either scenario, the influences of travelling CFI modes in the boundary layer are expected to be enhanced due to the PA forcing. To estimate such influence, the ratio $\bar{A}_t/\bar{A}_s$ is calculated and illustrated in figure 6.12(e). The ratio $\bar{A}_t/\bar{A}_s$ significantly increases at PA-*on* conditions. Nonetheless, it should be noted that this ratio $\bar{A}_t/\bar{A}_s$ is a more appropriate metric for linear cases (i.e. cases at relatively low *Re*) where non-linear CFI modes (e.g. type *III* and secondary CFI modes) are not significantly amplified. Furthermore, the $\bar{A}_t/\bar{A}_s$ differs significantly from the N_t^{env}/N_s^{env} discussed

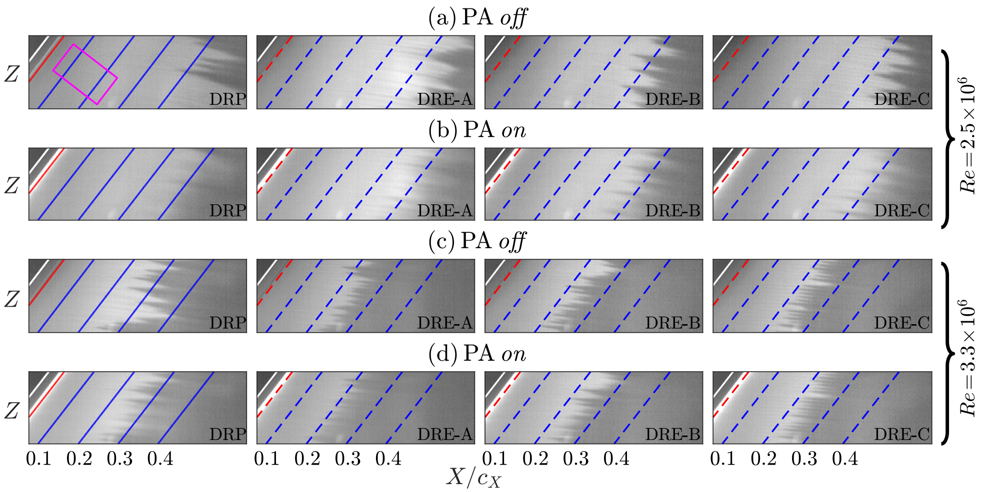

FIGURE 6.13: Transition front visualization at $\alpha = 2.5°$ for (a) $Re = 2.5 \times 10^6$, PA-*off*; (b) $Re = 2.5 \times 10^6$, PA-*on*; (c) $Re = 3.3 \times 10^6$, PA-*off*; (d) $Re = 3.3 \times 10^6$, PA-*on*. Flow comes from left and measurements are taken for DRP, DRE-A, DRE-B and DRE-C.

in section 6.3 and no direct comparison can be drawn at this point.

6.5. EFFECTS OF PLASMA-BASED BFM ON TRANSITION

This section examines the global effect of plasma-based BFM on the transition topology and location, through the use of IR thermography and corresponding quantification methods described in section 2.4.1. Several parameters are investigated, including the near-leading-edge surface roughness configurations (i.e. DRP and DRE-A/B/C), wing angle of attack α and Reynolds number Re.

6.5.1. TRANSITION TOPOLOGY

Figure 6.13 illustrates time-average IR images for DRP, DRE-A, DRE-B and DRE-C at $Re = 2.5 \times 10^6$ and $Re = 3.3 \times 10^6$. The leading edge of the $M3J$ model is indicated by the white solid line, while the red dashed line indicates the PA location. Additionally, blue dashed lines correspond to constant chord locations $x/c_x = 0.1$, 0.2, 0.3 and 0.4 respectively. For PA-*off*, contiguous turbulent wedges appear along the wing span for all tested cases, visualised by the thermal footprint caused by the local breakdown of stationary CF vortices [80]. These wedged transition fronts are also widely observed in swept wing transition studies [77, 81] and offer a first indication of the dominance of stationary CFIs at PA-*off* conditions. In fact, stationary CFI-dominated boundary layers are expected at PA-*off* conditions, considering the low level of freestream turbulence T_u ($< 0.03\%$) in the LTT facility and the sensitivity of stationary CFIs to surface roughness (i.e. DRP or DREs). Nonetheless, these wedged transition topology featured distinct differences between DRP- and DRE-conditioned cases. Evidently, DREs create more spanwise uniform transition fronts than DRP, due to the former's

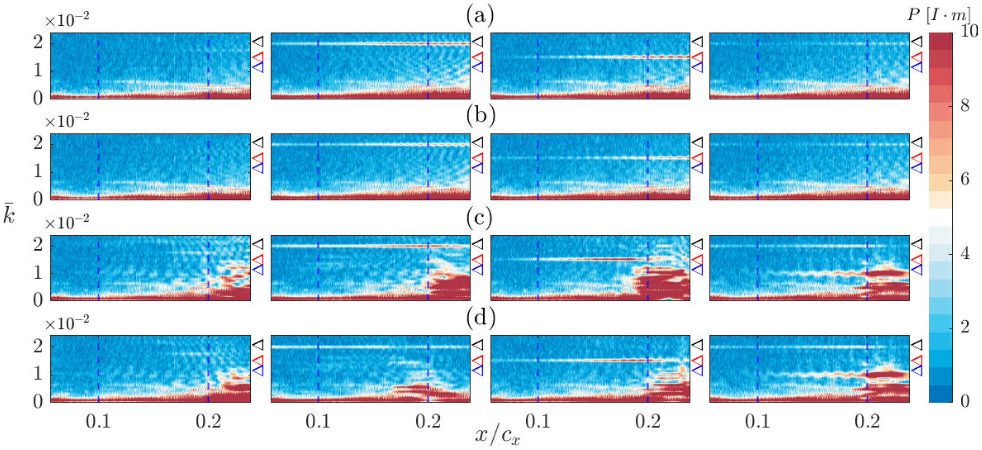

FIGURE 6.14: Same caption as figure 6.13 but for wavenumber spectra. Blue dashed lines correspond to $x/c_x = 0.1$ and 0.2 respectively. The black, red and blue triangles indicate the wavenumber $\bar{k}_6$, $\bar{k}_8$ and $\bar{k}_{10}$, respectively.

ability to concentrate perturbation energy in one single instability mode [80, 103]. In contrast, the distributed and broadband nature of DRP results in a more irregular transition pattern.

The characteristics of stationary CFI modes at PA-*off* are further revealed by the spanwise wavenumber spectra of IR imaging fields, as illustrated in figure 6.14(a) and (c). These spectra are extracted from images of camera IR-Zoom, imaging a FOV corresponding to the magenta box region in figure 6.13. The absence of evident spectral modes in the upstream portion of the FOV indicates no single monochromatic stationary CFI mode triggered by DRP, agreeing well with the previous PIV observations. In contrast, evident energy peaks are found at $\bar{k}_6$ and $\bar{k}_8$ respectively for DRE-A and DRE-B, confirming the upstream DRE excitation. Despite the same roughness element height h_{DRE} of DRE-A and DRE-B (i.e. similar initial amplitudes of $\bar{k}_6$ and $\bar{k}_8$ modes), the stationary CF mode of $\bar{k}_6$ shows an earlier growth than $\bar{k}_8$ at both low and high *Re*. This is also in agreement with the LST prediction, namely stationary modes of smaller wavelength are more amplified in the upstream region of the flow. Consistent with the PIV observations, instead of the $\bar{k}_{10}$ mode, the $\bar{k}_6$ mode is evidently amplified upstream, indicating the dominance of the $\bar{k}_6$ mode in DRE-C, though weaker than those induced by DRE-A. In fact, besides the LST-predicted early amplification of stationary modes of shorter $\bar{\lambda}$, the triggering of the $\bar{k}_6$ mode could be potentially attributed to the distinct neutral point locations of $\bar{k}_6$ and $\bar{k}_{10}$. As shown in figure 6.15, the neutral point of $\bar{k}_{10}$ is significantly downstream from the DRE location (i.e. x/c_x=0.02) compared to $\bar{k}_6$, which may consequently hinder the effective excitation of the $\bar{k}_{10}$ mode in the DRE-C case.

Figure 6.14(b) and (d) present the wavenumber spectra for PA-*on*. The spectra demonstrate that the PA forcing weakens the DRE-induced spectral peaks, confirming the general effect of plasma-based BFM in attenuating stationary CFI modes and

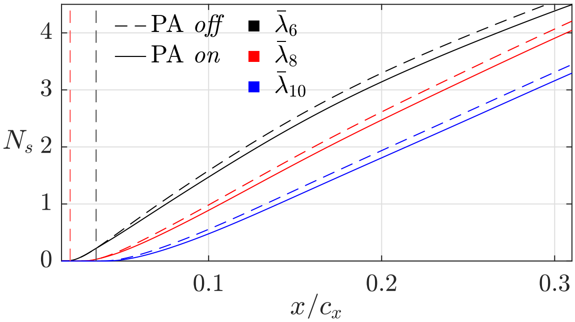

FIGURE 6.15: N factor of stationary CFI modes from the simplified model at $V_{p-p} = 7\,\mathrm{kV}$ and $Re = 2.5 \times 10^6$. The red and black vertical dashed lines indicate the location of x/c_x=0.02 and 0.035 respectively.

agreeing well with previous PIV results. Despite the presence of weaker stationary CFI modes in PA-*on* scenarios, the ensuing transition front is expected to be topologically similar to the PA-*off* case (i.e., sharp transition front), as long as stationary CFI modes are still dominant. However, a noticeable change in transition front topology is shown in figure 6.13(b) and indicates that plasma-based BFM does more than just weakening stationary CFI modes. Compared to PA-*off* cases, the PA operation imposes a 'blurring' effect on the transition front, where distinct turbulent wedges are spatially spread or even eradicated. This distinct blurred transition front is commonly attributed to the rise of travelling CFI modes and their subsequent unsteady laminar breakdown [34]. Unlike stationary CFI modes that predominantly propagate along local streamlines, travelling CFI modes exhibit significant deviations in propagation direction w.r.t local streamlines. This observation indicates the enhanced involvement of travelling CFI modes in the boundary layer development and transition process, due to the PA operation.

Following the method introduced in section 2.4.1, the IR intensity gradient density $|\nabla I|_d$ is used to quantify the blurriness of transition front, as illustrated in figure 6.16. Regarding all PA-*off* cases, the density $|\nabla I|_d$ reaches the minimum for DRE-A at $Re = 2.5 \times 10^6$. This result actually coincides with the slightly contaminated transition topology of DRE-A observed in figure 6.13(a), implying a relatively weak stationary CFI-dominated transition. When PA is on, the transition front is significantly affected. As shown in figure 6.16, $|\nabla I|_d$ generally presents very low values at PA-*on* (especially at lower Re), indicating contaminated transition fronts following the PA forcing. Furthermore, the tendency of $|\nabla I|_d$ also agrees well with the ratio N_t^{env}/N_s^{env} found in section 6.3 and the ratio $\bar{A}_t/\bar{A}_s$ in section 6.4.2, which obtain larger values at PA-*on* conditions. The observations ultimately lead to the conclusion that the PA operation significantly expands the involvement of travelling CFI modes in the boundary layer and diminishes the dominance of stationary CFI modes. On the other hand, it is noticed that the $|\nabla I|_d$ generally obtains larger values at higher Re at both PA-*off* and *on*. Such result also coincides with the observation of N_t^{env}/N_s^{env} (figure 6.5(c)), where the N_t^{env}/N_s^{env} generally exhibits smaller values at higher Re. This reveals a

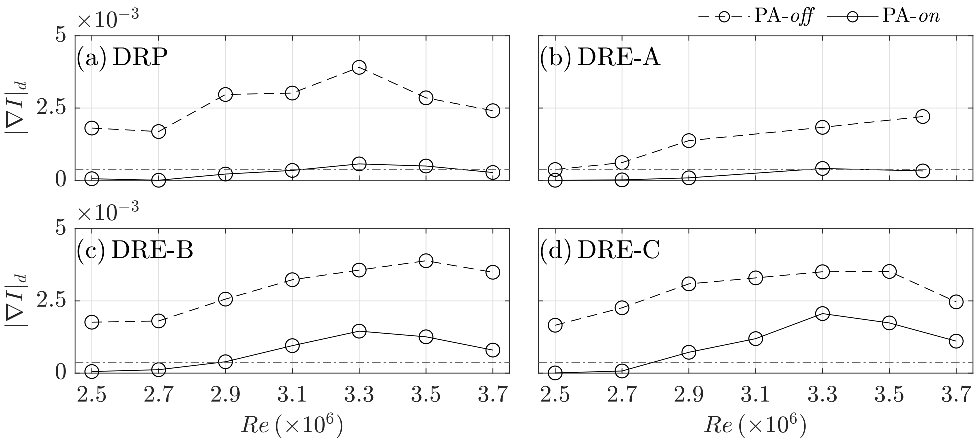

FIGURE 6.16: Average IR intensity gradient density $|\nabla I|_d$ under the condition of $\alpha = 2.5°$. The dot-dashed line indicates the $|\nabla I|_d$ of DRE-A at $Re = 2.5 \times 10^6$ and PA-*off*.

dependence of blurriness of transition on *Re* number. Specifically, the transition front will be less blurred (i.e. less contaminated by travelling CFI modes/more dominated by stationary CFI modes) at higher *Re*.

6.5.2. TRANSITION LOCATION

Following the approach described in section 2.4.1, the net laminar gain is quantified and transformed to an equivalent transition shift $\Delta(x_t/c_x)$, where $\Delta(x_t/c_x) > 0$ refers to transition delay and vice versa. The results are illustrated in figure 6.17 for various *Re* and α. In the case of DRP, the PA evidently advances the transition, particularly at lower α and lower *Re*. This result agrees well with the previous observation of $|\nabla I|_d$ suggesting a transition scenario dominated by travelling CFIs (as evident by the blurred transition front) at lower *Re* number. It is reasonable to assume that the higher efficacy of PA in advancing transition at lower *Re* number is closely linked to the higher susceptibility of boundary layer to travelling CFI modes. This is supported by the more pronounced increase of the envelope ratio N_t^{env}/N_s^{env} at lower *Re* numbers under conditions of PA-*on* (figure 6.5(c)). It is important to emphasize here that the observations regarding the DRP case do not contradict the fundamental concept of plasma-based BFM. The latter is meant to yield transition delay, especially at lower *Re* numbers where a given PA attains greater control authority within the boundary layer. Based on previous observations, the significant transition-advance effect is instead attributed to the competition between net BFM effect and intrinsic PA unsteadiness, as briefly described below. In the case of an idealised PA able to provide a time invariant net BFM effect (as commonly utilized in numerical simulations [29]), the transition is expected to be notably delayed. As *Re* increases, the transition delay becomes less significant until the PA loses its authority over the bulk boundary layer flow. However, in the case of a realistic plasma actuator, due to the intrinsic unsteadiness of the forcing, travelling CFI modes can be triggered and amplified

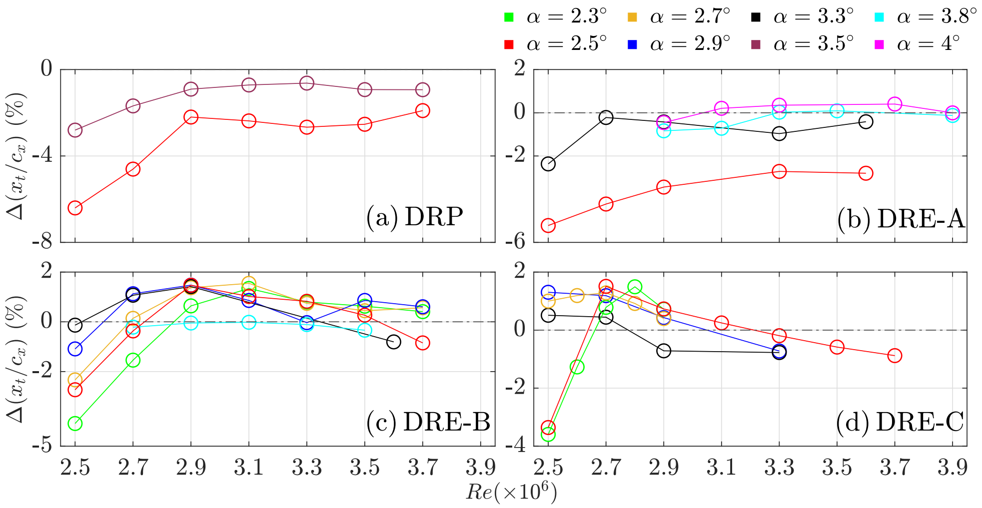

FIGURE 6.17: Transition front shift $\Delta(x_t/c_x)$ at various Re and α for (a) DRP; (b) DRE-A; (c) DRE-B; (d) DRE-C.

in the boundary layer. On the one hand, these initiated travelling CFI modes are favoured by the boundary layer at low Re number conditions and ultimately cancel out the beneficial net BFM effect, leading to significant transition advance. On the other hand, as Re increases, the effectiveness of net BFM effect diminishes due to the decreasing authority of PA, even though the boundary layer becomes less susceptible to travelling modes. It is yet to be determined whether there is an intermediate regime, where these two competing effects result in net transition delay.

In comparison to DRP, DRE-A exhibits similar trends of transition shift $\Delta(x_t/c_x)$ though with weaker values, indicating weaker PA effects in advancing transition. Nonetheless, it is noticed that the $\Delta(x_t/c_x)$ of DRE-A generally attains larger values at higher Re. This trend is further enhanced at higher angles of attack, where the $\Delta(x_t/c_x)$ even becomes slightly positive, indicating a subtle yet discernible transition delay. Similar trends can be observed in DRE-B and DRE-C, as shown in figure 6.17(c) and (d). However, the impact of PA on advancing transition is considerably weaker in DRE-B and DRE-C. In contrast, noticeable transition delays occur within a moderate range of Re numbers at various α. It appears that the weak transition delay observed in DRE-A is enhanced in DRE-B and DRE-C, underscoring the crucial roles of the forced wavelengths λ_{DRE}.

The occurrence of the maximum $\Delta(x_t/c_x)$ in DRE-B and DRE-C exhibits similarities to early studies of Deyhle & Bippes [25] and Bippes [7]. In their studies, transition was delayed when increasing the freestream turbulence T_u to moderate levels, compared to the extremely low T_u. Whereas further increasing T_u to higher levels, transition was again advanced. The growth and saturation of stationary CFI modes were observed to be suppressed in cases of high T_u. As hypothesized by the authors, when the T_u is low, stationary vortices dominate the boundary layer and

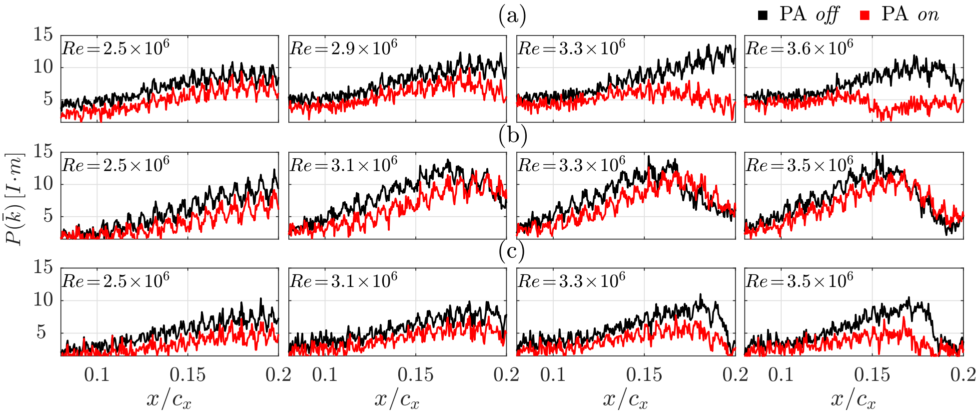

FIGURE 6.18: Spectral amplitudes $P(\bar{k})$ extracted from the wavenumber spectra (as shown in figure 6.14) at (a) $\bar{k}_6$ in DRE-A; (b) $\bar{k}_8$ in DRE-B; (c) $\bar{k}_6$ in DRE-C.

their higher saturation leads to strongly amplified secondary CFIs thus lowering the transitional Re number. Conversely, higher T_u stimulates primary travelling CFI modes thus advancing the transition as well. However, in an intermediate range of T_u, travelling CFI modes would suppress the growth and saturation of stationary CFI modes while themselves not growing sufficiently to incur breakdown, thereby resulting in a net transition delay. The interaction between primary stationary and travelling CFI modes was further investigated by the numerical work of Malik *et al.* [60]. The results indicate that the intensity of non-linear interactions between the primary stationary and travelling CFI modes depends on their initial amplitudes. In scenarios where the two primary modes have comparable amplitudes, the growth and saturation of stationary modes are indeed significantly suppressed. Similarly, the numerical work of Guo & Kloker [40] achieved transition delay by enhancing travelling CFI modes to suppress the dominant stationary CFI modes.

In a similar manner, the current work also observes the suppression of the development and saturation of stationary CFI modes. For each considered DRE case, the amplitudes of $P(\bar{k})$ are extracted from the spectra in figure 6.14 and illustrated in figure 6.18. To be noted that $P(\bar{k})$ is the IR intensity, which presents the thermal footprint of stationary vortices rather than their actual amplitudes. Nonetheless, considering that the IR intensity (i.e. surface temperature difference) arise from the shear stress generated by these vortices, the $P(\bar{k})$ can indirectly (albeit not linearly proportional) reflect the strength of stationary CFI modes. Evidently, in all tested cases, the growth and saturation of dominant stationary modes are generally suppressed due to the PA forcing. While this suppression effect may initially appear to be related to plasma-induced travelling CFI modes, it is important to take the net BFM effect into consideration as well. As demonstrated by previous results, the net BFM effect essentially renders the boundary layer more susceptible to travelling CFI modes, which could indirectly contribute to the suppression of stationary CFI modes' saturation. In the context of current work, it remains challenging to conclusively identify whether the suppression of stationary CFI modes is primarily attributed to the plasma-induced travelling CFI modes, the net BFM effect, or a combination of both factors.

In summary, the dependence of the transition behaviour on plasma-based BFM is found to follow analogous trends as to freestream turbulence [7, 25]. At the *Re* and α conditions where transition delay is maximised, the plasma-induced travelling CFI modes are likely to suppress the stationary CFI modes while themselves not growing excessively. This assumption is further supported by the moderate values of $|\nabla I|_{d,on}$ (figure 6.16) and $\bar{A}_{t,on}/\bar{A}_{s,on}$ (figure 6.12) in the range of transition delay *Re* numbers. This outcome further highlights a major limitation of plasma-based BFM, namely the requirement of sufficiently amplified stationary CFI modes in the boundary layer. This also aligns with the findings of Deyhle & Bippes [25], where transition was found to be most delayed in cases of moderate stationary vortices co-existing with travelling CFI modes initiated by a moderate T_u.

6.6. CONCLUSION

This Chapter employs a DBD plasma actuator to control CFIs and transition on a swept wing model, through the BFM strategy. A typical 2D spanwise-invariant PA is installed near the leading edge (x/c_x=0.035), forcing against the CF component. The net BFM effect is numerically investigated by the simplified body force model and LST. The results confirm a general stabilisation of both stationary and travelling CFIs due to the CF reduction. However, the ratio N_t^{env}/N_s^{env} implies that stationary CFI modes are more suppressed by the net BFM effect, rendering the boundary layer more susceptible to travelling CFI modes. This effect is particularly strong in scenarios for lower *Re* and stronger PA forcing.

The effects of plasma-based BFM on stationary and travelling CFIs are experimentally investigated by planar PIV at x/c_x=0.175. Distinct stationary CFI modes are initiated by surface roughness arrays. The dominant stationary CFI modes are weakened by the PA forcing, along with the reduction of spanwise gradient $\partial\bar{w}/\partial z$ and lobe structures, in agreement with the results of Chapter 5. On the other hand, travelling CFIs are generally amplified by PA, in spite of reduction at specific regions. The amplitude ratio $\bar{A}_t/\bar{A}_s$ further indicates the increase of travelling CFI modes in the boundary layer due to the plasma-based BFM strategy, which is more pronounced at lower *Re*.

Through the IR thermography, the transition topology and location are inspected. Generally, the average IR intensity gradient density $|\nabla I|_d$ obtains lower values at PA-*on*, demonstrating a blurred transition front due to the contamination of travelling CFIs. Specifically, this contamination is more severe when PA works at lower *Re*. The transition shift $\Delta(x_t/c_x)$ is further investigated w.r.t *Re* and surface-roughness arrays. In cases of weak stationary CFIs (i.e. DRP), PA exhibits a strong ability in advancing transition, especially at lower *Re*. Whereas, the advancing effect is weaker in cases of strong stationary CFI modes (i.e. DREs). Furthermore, the BFM-based PA achieved transition delay in DRE-B and DRE-C where a maximum transition delay is achieved at specific *Re*. This result essentially resembles the observation of Deyhle & Bippes [25] and [7] where transition was delayed in a specific range of freestream turbulence T_u, outside of which the transition was advanced. Additionally, the saturation of stationary CFI modes are found reduced.

In conclusion, in realistic applications, plasma-based BFM introduces the net BFM effect and the non-deterministic perturbations into the boundary layer. Both effects essentially enhance the influences of travelling CFIs in the boundary layer. Due to their substantial growth, these travelling CFIs can potentially hinder the effectiveness of net BFM effect. The alignment of the current results with previous work shows a hint that travelling CFIs may possibly have diminished detrimental impacts or even contribute positively to the net BFM effect by suppressing stationary CFIs, under certain circumstances. However, this cannot be confirmed by the current work and needs further investigations.

7

CONCLUSION AND RECOMMENDATIONS

A compilation of the most critical findings is hereby presented, together with a set of recommendations for future work

7.1. CONCLUSIONS

The research of this booklet detailed the effects of DBD PAs on the swept wing boundary layers, within the context of BFM technique. Corresponding investigations are achieved by advanced flow diagnostics along with complementary numerical solutions. Main conclusions corresponding to the objectives proposed in section 1.4 are summarized as below.

Objective A / Unsteady Perturbations of PA

It should be stressed that, the motivation of studying such disturbances starts from the work of Yadala *et al.* [99], where PA was demonstrated to indeed delay transition utilising the BFM strategy. Nonetheless, Serpieri *et al.* [87] found that unsteady disturbances (especially those of low-frequencies) were amplified due to the operation of BFM-based PA. Moralev *et al.* [64] later attributed these unsteady disturbances to the quasi-stochastic nature of PA micro-discharges. Due to the non-deterministic nature of the micro-discharges, these unsteady disturbances appear to be unavoidable during the PA operation, necessitating the elucidation of these unsteady disturbances within the context of BFM.

In Chapter 4, a BFM-based PA is operated at very low power to minimize the net BFM effect, focusing on the sole effects of plasma-induced unsteady disturbances. The amplification of plasma-induced unsteady disturbances are demonstrated by the spectral analysis, though their characteristics and frequencies significantly depend on frequency and location of the PA forcing. Further analysis shows that the upstream PA forcing enhances low-frequency type *III* modes, while the downstream forcing amplifies high-frequency type *I* modes. Moreover, low-frequency type *III* modes predominate in the presence of low-frequency forcing, whereas high-frequency type *I* modes become pronounced at the high-frequency PA forcing. Regarding the global PA effects on the transition process, the low-frequency PA forcing significantly accelerates the transition, particularly at the most upstream location (PA1). In contrast, the high-frequency PA forcing exhibits a relatively weaker influence on the transition location.

Objective B / PA Effects on Base Flow

The net BFM effect on the base flow is numerically investigated by the simplified body force model and LST analysis. A general BFM-caused stabilisation of the base flow is numerically confirmed. Chapter 5 presents the first experimental evidence demonstrating that the plasma-based BFM indeed reduces the CF component within a swept wing boundary layer. This experimental validation supports the fundamental hypothesis behind the plasma-based BFM as proposed by Serpieri *et al.* [87] and Yadala *et al.* [99]. The outcomes highlight that a more pronounced reduction of CF component can be achieved by the higher momentum coefficient c_μ. In addition, the BFM strategy displays a remarkable ability in manipulating the CF component w_s, even though the added momentum is delivered within the bulk velocity u_s direction. This highlights the important role of the PA forcing orientation with respect to the local CF component. The disparity in the reduction between u_s and w_s further prompts a directional alteration within the base flow. Notably, this alteration significantly influences the flow direction near the wall, illustrating the profound impact of the PA forcing in this proximal region. Whereas the flow direction remains unchanged in the freestream, highlighting the localized influence of the BFM approach.

Objective C/ PA Effects on Crossflow Instabilities

- **Stationary Crossflow Instabilities.** Both Chapter 5 and Chapter 6 demonstrate the efficacy of plasma-based BFM in weakening stationary CFIs within swept wing boundary layers. Specifically, in scenarios of both low-amplitude DRE-L and high-amplitude DRE-H in Chapter 5, the presence of PA forcing significantly diminishes the super-harmonic stationary modes. Whereas, the reduction of fundamental modes (DRE-induced modes) is solely observed in the DRE-L case. The disparate impacts of plasma-based BFM on reducing the fundamental modes are associated with h_{DRE} or more precisely, the amplitudes of the stationary CF vortices in the region interacting with the PA forcing. In the linear growth region as shown by DRE-L, the common amplitude reduction of stationary CFIs aligns with the LST results, confirming the BFM effect caused by the PA forcing. An intriguing observation in Chapter 5 is the notable spanwise shift of stationary CF vortex trajectories due to the PA forcing. Moreover, this effect is not only experimentally observed but also predicted by the LST analysis. Further analyses indicate that the trajectory alteration is supposed to stem from changes of local boundary layer stability within the PA forcing region.
- **Travelling Crossflow Instabilities.** The numerical investigations conducted in Chapter 5 and Chapter 6 confirm the overall stabilisation of both stationary and travelling CFIs, due to the CF reduction. Nonetheless, the LST analyses presented in Chapter 6 further suggest that the net BFM effect exerts a more pronounced suppression on stationary CFI modes (compared to travelling CFIs), as indicated by the ratio N_t^{env}/N_s^{env}. This in turn renders the boundary layer more susceptible to travelling CFI modes, particularly evident in scenarios of lower Re and stronger PA forcing. Chapter 5 and Chapter 6 investigate the fluctuations within the stationary CF vortex structures. The results confirm the universal amplification of travelling CFIs due to the PA forcing. However, the results further imply that, regarding velocity fluctuations within strong-shear regions of stationary structures (which are usually related to more developed CFIs, such as type I and type III modes), their amplitudes significantly depend on the strength of the carrying stationary CF vortices remaining downstream of the PA forcing region. In other words, despite the overall enhancement of travelling CFIs, these local fluctuations can be weakened by the PA forcing if the carrying stationary vortices are significantly diminished in the plasma region (Chapter 6). The blurriness quantification of transition front demonstrates that the PA forcing generally diminishes the typical jagged transition topology, confirming that the boundary layer becomes more dominated by travelling CFIs due to the PA modulation. However, it still remains challenging to attribute this result to either the net BFM effect (as predicted by LST) or the intrinsic PA unsteadiness (micro-discharges). Furthermore, the work of this thesis indicates that the plasma-induced unsteady disturbances cannot be conclusively determined as beneficial or detrimental to the BFM technique. On the one hand, they can possibly contribute to the reduction and early saturation of stationary CFIs (as shown by the spectral IR amplitudes in Chapter 6). On the other hand, their significant growth rates can destabilize the

boundary layer, thus weakening the net BFM effect.

Objective D/ PA Effects on Laminar-turbulent Transition
Chapter 6 investigates the effects of plasma-based BFM on the transition topology and transition location through the IR technique. The results confirm that the transition front is contaminated/blurred by plasma-caused travelling CFIs, even with a high f_{AC}. Specifically, this contamination becomes notably more pronounced when PA operates at lower Re. The transition location is further investigated w.r.t Re and surface roughness arrays. In cases of weak stationary CFIs (i.e. DRP), PA exhibits a strong ability in advancing transition, especially at lower Re. Whereas, the advancing effect is weaker in cases of strong stationary CFI modes (i.e. DREs). Furthermore, it appears that the plasma-based BFM can indeed achieve transition delay, however, will be limited within a specific range of Re, as shown by DRE-B and DRE-C. For a net BFM effect, it is expected that a more pronounced transition delay will be achieved at lower Re, since the PA forcing gradually loses the authority within the boundary layer at higher Re. Therefore, the currently observed maximum transition delay at specific Re shall be attributed to the plasma-caused travelling CFIs. This assumption is further supported by the observation of Deyhle & Bippes [25] and Bippes [7] where transition was delayed in a specific range of freestream turbulence T_u. When increasing T_u from extremely low to moderate levels, the transition is actually delayed. Whereas, the further increase of Re leads to transition advance. It appears that, in an intermediate T_u range, travelling CFI modes delayed transition by suppressing stationary CFI modes' growth without reaching breakdown. This is also likely contributing to the currently observed maximum transition delay at specific Re.

7.2. Outlook and Recommendations

By reducing the CF component, the BFM strategy straightforwardly diminishes the CFIs, stabilizing the swept wing boundary layer. Its robust operation and practical implementation make this technique one of the most promising approaches for controlling swept wing boundary layers. Despite its potential as demonstrated in this study, several uncertainties persist and are exemplified as below, requiring further investigation and experimental validation.

First of all, to enhance the applicability of the plasma-based BFM technique in future practical scenarios, it is imperative to tackle the intrinsic non-deterministic unsteadiness of PAs. Nonetheless, there is potential to not only address but also leverage this PA unsteadiness. The study conducted by Guo & Kloker [40] numerically demonstrated that sub-critical positive travelling CFI modes have the potential to suppress both critical stationary and travelling CFI modes, thereby achieving transition delay. This finding is reflected by the experimental work of Deyhle & Bippes [25] and the current study where travelling CFI modes are assumed to contribute to the transition delay. Therefore, to leverage the non-deterministic unsteadiness induced by PAs, the discrete PAs could be used for all PA-based strategies (section 1.3.3). The spanwise spacing of these discrete PAs should align with the wavelengths of sub-critical travelling CFI modes. Consequently, though the PA operation inevitably induces travelling CFIs (due to the non-deterministic unsteadiness), these PA-induced travelling CFI modes are at least most likely to be the (positive) sub-critical CFI modes. These modes can possibly enhance the effectiveness of PA-based LFC under specific flow conditions, taking into account local boundary layer stability characteristics.

In addition, the maximum transition shift $\Delta(x_t/c_x)$ observed in figure 6.17 at specific *Re* is thought to result from the suppression of stationary CFIs by travelling CFIs. However, this assumption needs validation through experiments. Such crucial experiment needs the involvement of plasma-induced unsteady disturbances without influence of net BFM effect. If the assumption is true, transition delays are assumed to be achieved at specific combinations of λ_{DRE} and f_{AC}. In fact, such experiment essentially resembles conditions explored in Chapter 4, where no transition delay was observed. In Chapter 4, despite attempts to reduce the net BFM effect by operating PA at lower power, the plasma-induced unsteady disturbances feature concentrated energies at the critical frequency (i.e. 200 Hz). This can produce more critical travelling CFI modes of significant initial amplitudes compared to scenarios of plasma-based BFM, where the non-deterministic unsteady disturbances are expected to distribute in random frequencies.

Moreover, the efficacy of plasma-based BFM exhibits a complicated dependence on the wavelength λ_{DRE} and angle of attack α. In cases of DRE-B in Chapter 6, (figure 6.17), the maximum transition shift $\Delta(x_t/c_x)$ tends to shift towards lower *Re* when increasing α. Whereas in cases of DRE-C, the maximum $\Delta(x_t/c_x)$ appears to shift even further to lower *Re*. On the other hand, as α increases, the $\Delta(x_t/c_x)$ tends to approach 0 in DRP and DRE-A. This implies that the maximum $\Delta(x_t/c_x)$ may be identified for DRP and DRE-A when further increasing α. This observation further emphasizes that the suppression of stationary CFIs by travelling CFIs to delay transition is contingent upon specific combinations of *Re*, α, and λ_{DRE}. This complexity in the design and effective range of the plasma-based BFM warrants further investigation.

Additionally, it is important to note that this study does not consider other types of instabilities. As demonstrated in Chapter 6, the BFM strategy essentially renders the boundary layer more 'two-dimensional' by reducing the CF component. Consequently, 2D instabilities such as TS waves might exert more substantial influences within the swept wing boundary layer (particularly those featuring weaker favourable pressure distributions), as discussed in section 6.3 in Chapter 6. Considering the 2D structure and inherent unsteadiness of the PA forcing, typical TS waves may be initially amplified along with CFIs in the PA forcing region. Further investigations are required on this aspect.

BIBLIOGRAPHY

[1] ARKESTEIJN, JOERIE 2021 Cross-flow instability control through base-flow modification using ac-dbd plasma actuators: An experimental investigation. Master's thesis, Delft University of Technology.

[2] ARNDT, ALEXANDER, CORKE, THOMAS, MATLIS, ERIC & SEMPER, MICHAEL 2020 Controlled stationary/travelling cross-flow mode interaction in a mach 6.0 boundary layer. *Journal of Fluid Mechanics* **887**, A30.

[3] ASTARITA, T. & CARLOMAGNO, G. M. 2012 *Infrared thermography for thermo-fluid-dynamics*. Springer Science & Business Media.

[4] BARANOV, SERGEY A, CHERNYSHEV, SERGEY L, KHOMICH, VLADISLAV YU, KISELEV, ANDREY PH, KURYACHII, ALEKSANDR P, MOSHKUNOV, SERGEY I, REBROV, IGOR E, SBOEV, DMITRY S, TOLKACHEV, STEPAN N & YAMSHCHIKOV, VLADIMIR A 2021 Experimental cross-flow control in a 3d boundary layer by multi-discharge plasma actuators. *Aerospace Science and Technology* **112**, 106643.

[5] BENARD, N, MIZUNO, A & MOREAU, E 2009 A large-scale multiple dielectric barrier discharge actuator based on an innovative three-electrode design. *Journal of Physics D: Applied Physics* **42** (23), 235204.

[6] BENARD, NICOLAS & MOREAU, ERIC 2014 Electrical and mechanical characteristics of surface ac dielectric barrier discharge plasma actuators applied to airflow control. *Experiments in Fluids* **55** (11), 1–43.

[7] BIPPES, HANS 1999 Basic experiments on transition in three-dimensional boundary layers dominated by crossflow instability. *Progress in aerospace sciences* **35** (4), 363–412.

[8] BONFIGLI, GIUSEPPE & KLOKER, M 2005 Numerical investigation of transition caused by superposed steady and travelling crossflow vortices. *Univ. of Stuttgart, Inst. of Aerodynamics and Gas Dynamics, Tech. Rept. IAG-TR-2005-CFTRANS* .

[9] BONFIGLI, GIUSEPPE & KLOKER, MARKUS 2007 Secondary instability of crossflow vortices: validation of the stability theory by direct numerical simulation. *Journal of fluid mechanics* **583**, 229.

[10] BORODULIN, VI, IVANOV, AV & KACHANOV, YS 2015 Scenarios of swept-wing boundary-layer transition in presence of various kinds of freestream turbulence and surface roughnesses. *Procedia IUTAM* **14**, 283–294.

[11] BORODULIN, VI, IVANOV, AV, KACHANOV, YS & MISCHENKO, DA 2014 Experimental investigation of characteristics of steady and unsteady crossflow-instability modes developing in a 35-degree swept-airfoil boundary layer. In *Proc. 17th Int. Conf. Methods of Aerophysical Research*.

[12] BORODULIN, VI, IVANOV, AV, KACHANOV, YS & MISCHENKO, DA 2023 Excitation of crossflow modes in a swept-airfoil boundary layer. part 1. surface receptivity. *European Journal of Mechanics-B/Fluids* **100**, 256–269.

[13] BORODULIN, VI, IVANOV, AV, KACHANOV, YS & ROSCHEKTAEV, AP 2013 Receptivity coefficients at excitation of cross-flow waves by free-stream vortices in the presence of surface roughness. *Journal of Fluid Mechanics* **716**, 487–527.

[14] BORODULIN, VI, IVANOV, AV, KACHANOV, YS & ROSCHEKTAEV, AP 2016 Receptivity coef-

ficients at excitation of cross-flow waves due to scattering of free-stream vortices on surface vibrations. *Journal of Fluid Mechanics* **793**, 162–208.

[15] Borodulin, VI, Ivanov, AV, Kachanov, YS & Roschektayev, AP 2021 Distributed vortex receptivity of a swept-wing boundary layer. part 1. efficient excitation of cf modes. *Journal of Fluid Mechanics* **908**.

[16] Borodulin, VI, Ivanov, AV, Kachanov, YS & Roschektayev, AP 2021 Distributed vortex receptivity of a swept-wing boundary layer. part 2. receptivity characteristics. *Journal of Fluid Mechanics* **908**.

[17] Bruun, Hans H 1996 Hot-wire anemometry: principles and signal analysis. *Measurement Science and Technology* **7** (10), 024.

[18] Casacuberta, Jordi, Groot, Koen J, Hickel, Stefan & Kotsonis, Marios 2022 Secondary instabilities in swept-wing boundary layers: Direct numerical simulations and biglobal stability analysis. In *AIAA SCITECH 2022 Forum*, p. 2330.

[19] Corke, Thomas, Arndt, Alexander, Matlis, Eric & Semper, Michael 2018 Control of stationary cross-flow modes in a mach 6 boundary layer using patterned roughness. *Journal of Fluid Mechanics* **856**, 822–849.

[20] Corke, Thomas C, Enloe, C Lon & Wilkinson, Stephen P 2010 Dielectric barrier discharge plasma actuators for flow control. *Annual review of fluid mechanics* **42**, 505–529.

[21] Corke, Thomas C, Post, Martiqua L & Orlov, Dmitry M 2007 Sdbd plasma enhanced aerodynamics: concepts, optimization and applications. *Progress in Aerospace Sciences* **43** (7-8), 193–217.

[22] Dagenhart, Jray, Stack, Jpeter, Saric, William & Mousseux, Marc 1989 Crossflow-vortex instability and transition on a 45 deg swept wing. In *20th Fluid Dynamics, Plasma Dynamics and Lasers Conference*, p. 1892.

[23] Dallmann, U & Bieler, H 1987 Analysis and simplified prediction of primary instability of three-dimensional boundary-layer flows. In *19th AIAA, Fluid Dynamics, Plasma Dynamics, and Lasers Conference*, p. 1337.

[24] Debien, A, Benard, N, David, L & Moreau, E 2012 Unsteady aspect of the electrohydrodynamic force produced by surface dielectric barrier discharge actuators. *Applied Physics Letters* **100** (1).

[25] Deyhle, H & Bippes, H 1996 Disturbance growth in an unstable three-dimensional boundary layer and its dependence on environmental conditions. *Journal of Fluid Mechanics* **316**, 73–113.

[26] Discetti, Stefano & Ianiro, Andrea 2017 *Experimental aerodynamics*. CRC Press.

[27] Dobbinga, E 1955 De lage snelheids windtunnel van de sub-afdeling vliegtuigbouwkunde der technische hogeschool. *Publicatie in: De Ingenieur, Algemeen gedeelte, No. 38, September 1955* .

[28] Dörr, Philipp 2018 Numerical investigation of crossflow transition control using plasma actuators. PhD thesis, University of Stuttgart.

[29] Dörr, PC & Kloker, MJ 2015 Stabilisation of a three-dimensional boundary layer by base-flow manipulation using plasma actuators. *Journal of Physics D: Applied Physics* **48** (28), 285205.

[30] Dörr, PC & Kloker, MJ 2016 Transition control in a three-dimensional boundary layer by direct attenuation of nonlinear crossflow vortices using plasma actuators. *International Journal of Heat and Fluid Flow* **61**, 449–465.

[31] Dörr, Philipp, Kloker, Markus & Hanifi, Ardeshir 2017 Effect of upstream flow deforma-

tion using plasma actuators on crossflow transition induced by unsteady vortical free-stream disturbances. In *47th AIAA Fluid Dynamics Conference*, p. 3114.

[32] Dörr, Philipp C & Kloker, Markus J 2017 Crossflow transition control by upstream flow deformation using plasma actuators. *Journal of Applied Physics* **121** (6), 063303.

[33] Downs, Robert, Lovig, Erica & White, Edward 2012 Experimental investigation of the crossflow instability in moderate freestream turbulence. In *42nd AIAA Fluid Dynamics Conference and Exhibit*, p. 2824.

[34] Downs, Robert S & White, Edward B 2013 Free-stream turbulence and the development of cross-flow disturbances. *Journal of Fluid Mechanics* **735**, 347–380.

[35] Enloe, CL, Font, GI, McLaughlin, TE & Orlov, DM 2008 Surface potential and longitudinal electric field measurements in the aerodynamic plasma actuator. *AIAA journal* **46** (11), 2730–2740.

[36] Enloe, C, McHarg, M, Font, Gabriel & McLaughlin, Thomas 2009 Plasma-induced force and self-induced drag in the dielectric barrier discharge aerodynamic plasma actuator. In *47th AIAA Aerospace Sciences Meeting including The New Horizons Forum and Aerospace Exposition*, p. 1622.

[37] Friederich, Tillmann & Kloker, Markus J 2012 Control of the secondary cross-flow instability using localized suction. *Journal of fluid mechanics* **706**, 470–495.

[38] Gaponenko, VR, Ivanov, AV, Kachanov, Yu S & Crouch, JD 2002 Swept-wing boundary-layer receptivity to surface non-uniformities. *Journal of Fluid Mechanics* **461**, 93–126.

[39] Grundmann, Sven & Tropea, Cameron 2008 Active cancellation of artificially introduced tollmien–schlichting waves using plasma actuators. *Experiments in Fluids* **44** (5), 795–806.

[40] Guo, Zhengfei & Kloker, Markus J 2019 Control of crossflow-vortex-induced transition by unsteady control vortices. *Journal of Fluid Mechanics* **871**, 427–449.

[41] Guo, Zhengfei & Kloker, Markus J 2020 Effects of low-frequency noise in crossflow transition control. *AIAA Journal* **58** (3), 1068–1078.

[42] Haynes, Tim S & Reed, Helen L 2000 Simulation of swept-wing vortices using nonlinear parabolized stability equations. *Journal of Fluid Mechanics* **405**, 325–349.

[43] He, Chuan, Corke, Thomas C & Patel, Mehul P 2009 Plasma flaps and slats: an application of weakly ionized plasma actuators. *Journal of aircraft* **46** (3), 864–873.

[44] Hinsch, Klaus D 1995 Three-dimensional particle velocimetry. *Measurement Science and Technology* **6** (6), 742.

[45] Högberg, Markus & Henningson, Dan 1998 Secondary instability of cross-flow vortices in falkner-skan-cooke boundary layers. *Journal of Fluid Mechanics* **368** (1), 339–357.

[46] Hosseini, Seyed M, Tempelmann, David, Hanifi, Ardeshir & Henningson, Dan S 2013 Stabilization of a swept-wing boundary layer by distributed roughness elements. *Journal of Fluid Mechanics* **718**, R1.

[47] Joslin, Ronald D 1998 Aircraft laminar flow control. *Annual review of fluid mechanics* **30** (1), 1–29.

[48] Kogelschatz, Ulrich 2003 Dielectric-barrier discharges: their history, discharge physics, and industrial applications. *Plasma chemistry and plasma processing* **23** (1), 1–46.

[49] Kotsonis, Marios 2015 Diagnostics for characterisation of plasma actuators. *Measurement Science and Technology* **26** (9), 092001.

[50] Kotsonis, M, Ghaemi, S, Veldhuis, L & Scarano, F 2011 Measurement of the body force

field of plasma actuators. *Journal of Physics D: Applied Physics* **44** (4), 045204.

[51] Kotsonis, Marios, Giepman, Rogier, Hulshoff, Steven & Veldhuis, Leo 2013 Numerical study of the control of tollmien–schlichting waves using plasma actuators. *AIAA journal* **51** (10), 2353–2364.

[52] Kriegseis, Jochen 2011 Performance characterization and quantification of dielectric barrier discharge plasma actuators. PhD thesis, Technische Universität Darmstadt.

[53] Krishnan, KSG, Bertram, O & Seibel, O 2017 Review of hybrid laminar flow control systems. *Progress in Aerospace Sciences* **93**, 24–52.

[54] Kurz, Holger BE & Kloker, Markus J 2014 Receptivity of a swept-wing boundary layer to micron-sized discrete roughness elements. *Journal of fluid mechanics* **755**, 62–82.

[55] Kurz, Holger BE & Kloker, Markus J 2016 Mechanisms of flow tripping by discrete roughness elements in a swept-wing boundary layer. *Journal of Fluid Mechanics* **796**, 158–194.

[56] Lohse, Jakob, Barth, Hans Peter & Nitsche, Wolfgang 2016 Active control of crossflow-induced transition by means of in-line pneumatic actuator orifices. *Experiments in Fluids* **57** (8), 1–10.

[57] Lomas, Charles G 2011 *Fundamentals of hot wire anemometry*. Cambridge University Press.

[58] Mack, Leslie M 1984 Boundary-layer linear stability theory. *Tech. Rep.*. California Inst of Tech Pasadena Jet Propulsion Lab.

[59] Maden, I, Maduta, R, Kriegseis, J, Jakirlić, S, Schwarz, C, Grundmann, S & Tropea, C 2013 Experimental and computational study of the flow induced by a plasma actuator. *International Journal of Heat and Fluid Flow* **41**, 80–89.

[60] Malik, MR, Li, F & Chang, C-L 1994 Crossflow disturbances in three-dimensional boundary layers: nonlinear development, wave interaction and secondary instability. *Journal of Fluid Mechanics* **268**, 1–36.

[61] Malik, Mujeeb R, Li, Fei, Choudhari, Meelan M & Chang, Chau-Lyan 1999 Secondary instability of crossflow vortices and swept-wing boundary-layer transition. *Journal of Fluid Mechanics* **399**, 85–115.

[62] Merino-Martínez, Roberto, Carpio, Alejandro Rubio, Pereira, Lourenço Tércio Lima, van Herk, Steve, Avallone, Francesco, Ragni, Daniele & Kotsonis, Marios 2020 Aeroacoustic design and characterization of the 3d-printed, open-jet, anechoic wind tunnel of delft university of technology. *Applied Acoustics* **170**, 107504.

[63] Messing, Ralf & Kloker, Markus J 2010 Investigation of suction for laminar flow control of three-dimensional boundary layers. *Journal of Fluid Mechanics* **658**, 117.

[64] Moralev, Ivan, Selivonin, Igor & Ustinov, Maxim 2019 On the stochastic forcing of the boundary layer by plasma actuators. *Experiments in Fluids* **60** (12), 1–9.

[65] Morkovin, Mark V 1969 On the many faces of transition. In *Viscous Drag Reduction: Proceedings of the Symposium on Viscous Drag Reduction held at the LTV Research Center, Dallas, Texas, September 24 and 25, 1968*, pp. 1–31. Springer.

[66] Neumann, Mathias, Friedrich, Christian, Czarske, Jürgen, Kriegseis, Jochen & Grundmann, Sven 2012 Determination of the phase-resolved body force produced by a dielectric barrier discharge plasma actuator. *Journal of Physics D: Applied Physics* **46** (4), 042001.

[67] Peng, Kaisheng, Arkesteijn, JPW, Avallone, Francesco & Kotsonis, Marios 2022 Experimental base flow modification on a swept wing using plasma forcing. *Physics of Fluids* **34** (10), 103614.

[68] Peng, K, Avallone, F & Kotsonis, M 2022 Unsteady disturbances in a swept wing boundary

layer due to plasma forcing. *Physics of Fluids* **34** (11), 114115.

[69] Peng, Kaisheng & Kotsonis, Marios 2021 Cross-flow instabilities under plasma actuation: Design, commissioning and preliminary results of a new experimental facility. In *AIAA Scitech 2021 Forum*, p. 1194.

[70] Pereira, Ricardo, Ragni, Daniele & Kotsonis, Marios 2014 Effect of external flow velocity on momentum transfer of dielectric barrier discharge plasma actuators. *Journal of applied physics* **116** (10).

[71] Prandtl, Ludwig 1905 Uber flussigkeitsbewegung bei sehr kleiner reibung. *Verhandl. 3rd Int. Math. Kongr. Heidelberg (1904), Leipzig* .

[72] Radeztsky Jr, Ronald H, Reibert, Mark S & Saric, William S 1999 Effect of isolated micron-sized roughness on transition in swept-wing flows. *AIAA journal* **37** (11), 1370–1377.

[73] Raffel, Markus, Merz, Christoph B, Schwermer, Till & Richter, Kai 2015 Differential infrared thermography for boundary layer transition detection on pitching rotor blade models. *Experiments in Fluids* **56** (2), 1–13.

[74] Raffel, Markus, Willert, Christian E, Scarano, Fulvio, Kähler, Christian J, Wereley, Steve T, Kompenhans, Jürgen, Raffel, Markus, Willert, Christian E, Scarano, Fulvio, Kähler, Christian J & others 2018 Piv uncertainty and measurement accuracy. *Particle Image Velocimetry: A Practical Guide* pp. 203–241.

[75] Reynolds, Osborne 1883 Xxix. an experimental investigation of the circumstances which determine whether the motion of water shall be direct or sinuous, and of the law of resistance in parallel channels. *Philosophical Transactions of the Royal society of London* (174), 935–982.

[76] Rius Vidales, AF 2022 Influence of a forward-facing step on crossflow instability and transition: An experimental study in a swept wing boundary-layer. PhD thesis, Delft University of Technology.

[77] Rius-Vidales, Alberto F & Kotsonis, Marios 2020 Influence of a forward-facing step surface irregularity on swept wing transition. *AIAA Journal* **58** (12), 5243–5253.

[78] Rius-Vidales, Alberto F, Kotsonis, Marios, Antunes, Alexandre P & Cosin, Renato 2018 Effect of two-dimensional surface irregularities on swept wing transition: forward facing steps. In *2018 Fluid Dynamics Conference*, p. 3075.

[79] Saric, William, Carrillo, Jr, Ruben & Reibert, Mark 1998 Leading-edge roughness as a transition control mechanism. In *36th AIAA Aerospace Sciences Meeting and Exhibit*, p. 781.

[80] Saric, William S, Reed, Helen L & White, Edward B 2003 Stability and transition of three-dimensional boundary layers. *Annual review of fluid mechanics* **35** (1), 413–440.

[81] Saric, William S, West, David E, Tufts, Matthew W & Reed, Helen L 2019 Experiments on discrete roughness element technology for swept-wing laminar flow control. *AIAA Journal* **57** (2), 641–654.

[82] Schuele, Chan Yong, Corke, Thomas C & Matlis, Eric 2013 Control of stationary cross-flow modes in a mach 3.5 boundary layer using patterned passive and active roughness. *Journal of Fluid Mechanics* **718**, 5–38.

[83] Sciacchitano, Andrea & Wieneke, Bernhard 2016 Piv uncertainty propagation. *Measurement Science and Technology* **27** (8), 084006.

[84] Serpieri, J 2018 Cross-flow instability: Flow diagnostics and control of swept wing boundary layers. PhD thesis, Delft University of Technology.

[85] Serpieri, Jacopo & Kotsonis, Marios 2015 Design of a swept wing wind tunnel model for study of cross-flow instability. In *33rd AIAA Applied Aerodynamics Conference*, p. 2576.

[86] Serpieri, Jacopo & Kotsonis, Marios 2016 Three-dimensional organisation of primary and secondary crossflow instability. *J. Fluid Mech* **799**, 200–245.

[87] Serpieri, Jacopo, Yadala, Srikar & Kotsonis, Marios 2017 Conditioning of cross-flow instability modes using dielectric barrier discharge plasma actuators. *J. Fluid Mech* **833**, 164–205.

[88] Shahriari, Nima, Kollert, Matthias R & Hanifi, Ardeshir 2018 Control of a swept-wing boundary layer using ring-type plasma actuators. *Journal of Fluid Mechanics* **844**, 36–60.

[89] Shneider, M, Likhanskii, A, Macheret, S, Opaits, D & Miles, D 2010 State-of-the-art high-fidelity dbd plasma simulations. In *AFOSR DBD Plasma Actuator Workshop, 24-25 February 2010, Gainesville, FL.*

[90] Smith, Barton L, Neal, Douglas R, Feero, Mark A & Richards, Geordie 2018 Assessing the limitations of effective number of samples for finding the uncertainty of the mean of correlated data. *Measurement Science and Technology* **29** (12), 125304.

[91] Tropea, Cameron, Yarin, Alexander L, Foss, John F & others 2007 *Springer handbook of experimental fluid mechanics*, , vol. 1. Springer.

[92] Wang, Jin-Jun, Choi, Kwing-So, Feng, Li-Hao, Jukes, Timothy N & Whalley, Richard D 2013 Recent developments in dbd plasma flow control. *Progress in Aerospace Sciences* **62**, 52–78.

[93] Wang, Zhefu, Wang, Liang & Fu, Song 2017 Control of stationary crossflow modes in swept hiemenz flows with dielectric barrier discharge plasma actuators. *Physics of Fluids* **29** (9), 094105.

[94] Wassermann, Peter & Kloker, Markus 2002 Mechanisms and passive control of crossflow-vortex-induced transition in a three-dimensional boundary layer. *Journal of Fluid Mechanics* **456**, 49.

[95] Wassermann, Peter & Kloker, Markus 2003 Transition mechanisms induced by travelling crossflow vortices in a three-dimensional boundary layer. *Journal of Fluid Mechanics* **483**, 67–89.

[96] White, Edward B & Saric, William S 2005 Secondary instability of crossflow vortices. *Journal of Fluid Mechanics* **525**, 275.

[97] Yadala, Srikar 2020 Plasma-flow interfaces for instability control. PhD thesis, Université de Poitiers.

[98] Yadala, Srikar, Hehner, Marc, Serpieri, Jacopo, Benard, Nicolas & Kotsonis, Marios 2018 Swept-wing transition control using ac-dbd plasma actuators. In *2018 Flow Control Conference*, p. 3215.

[99] Yadala, Srikar, Hehner, Marc T, Serpieri, Jacopo, Benard, Nicolas, Dörr, Philipp C, Kloker, Markus J & Kotsonis, Marios 2018 Experimental control of swept-wing transition through base-flow modification by plasma actuators. *Journal of Fluid Mechanics* **844**.

[100] Yadala, Srikar, Hehner, Marc T, Serpieri, Jacopo, Benard, Nicolas & Kotsonis, Marios 2021 Plasma-based forcing strategies for control of crossflow instabilities. *AIAA Journal* pp. 1–11.

[101] Zoppini, G 2023 Receptivity of swept wing boundary layers to surface roughness: Diagnostics and extension to flow control. PhD thesis, Delft University of Technology.

[102] Zoppini, Giulia, Michelis, Theodoros, Ragni, Daniele & Kotsonis, Marios 2022 Cancellation of crossflow instabilities through multiple discrete roughness elements forcing. *Physical Review Fluids* **7** (12), 123902.

[103] Zoppini, G, Michelis, Theodorus, Ragni, D & Kotsonis, M 2023 The near wake of discrete roughness elements on swept wings. *Journal of Fluid Mechanics* **960**, A11.

[104] Zoppini, Giulia, Ragni, Daniele & Kotsonis, Marios 2021 Experimental investigation on receptivity of crossflow instability to discrete roughness amplitude and location. In *AIAA Scitech 2021 Forum*, p. 0152.

[105] Zoppini, G, Westerbeek, S, Ragni, D & Kotsonis, M 2022 Receptivity of crossflow instability to discrete roughness amplitude and location. *Journal of Fluid Mechanics* **939**, A33.

List of Publications

Journal Publications

3. K Peng, F Avallone, M Kotsonis. Plasma-based base flow modification on swept wing boundary layers: dependence on flow parameters. *Journal of Fluid Mechanics* (under review).

2. K Peng, F Avallone, M Kotsonis. 2022. Unsteady disturbances in a swept wing boundary layer due to plasma forcing. *Physics of Fluids* 34 (11). [68]

1. K Peng, JPW Arkesteijn, F Avallone, M Kotsonis. 2022. Experimental base flow modification on a swept wing using plasma forcing. *Physics of Fluids* 34(10). [67]

Conference Proceedings and presentations

3. K. Peng, F. Avallone and M. Kotsonis. 2023. Swept wing transition controlled by plasma-based base flow modification. *16th International Conference on Fluid Control, Measurements, and Visualization.*

2. K. Peng, J.P.W. Arkesteijn, F. Avallone and M. Kotsonis. 2022. EXPERIMENTAL BASE FLOW MODIFICATION THROUGH PLASMA ACTUATION ON A SWEPT WING. *European Drag Reduction and Flow Control Meeting, EDRFCM 2022.*

1. K Peng, M Kotsonis. 2021. Crossflow instabilities under plasma actuation: Design, commissioning and preliminary results of a new experimental facility. *AIAA SCITECH 2021 Forum.* [69]

CURRICULUM VITÆ

Kaisheng Peng

09-May-1992	Born in Sichuan, China.

EDUCATION

2018–2024	PhD in Aerospace Engineering Delft University of Technology, The Netherlands *Base Flow Modification by Plasma Actuation for Swept Wing Transition Control*
2015–2018	Master in Electrical Engineering Southwest Jiaotong University, China *Plasma Flow Control on High-speed Railway*
2011–2015	Bachelor in Electrical Engineering Southwest Jiaotong University, China

OTHER EXPERIENCES

2022	Culham Plasma Physics Summer School
2021	Prague-Sum Workshop
2019	VKI Lecture Series on Introduction to Measurement Techniques